Universitá di Pavia

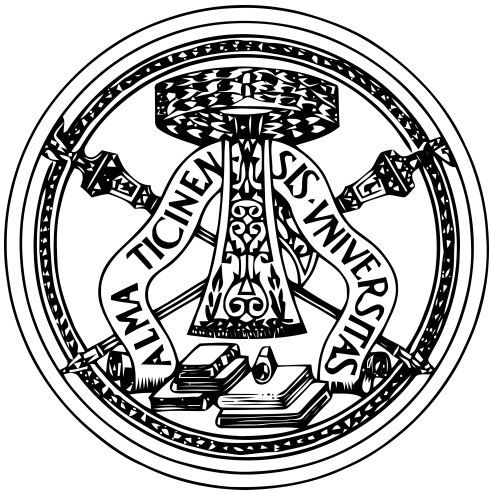

PhD in Electrical, Computer and Biomedical engineering

Faculty of Engineering

High energy nanosecond laser systems for nonlinear optics and remote sensing applications

PhD Thesis of

Luigi Fregnani

XXXI PhD cycle

Contents

Summary of the PhD Thesis

During my PhD research activity carried out at the Laser Source Laboratory of the University of Pavia, I had the opportunity to study and develop complex high-energy (from several mJ to several tens of mJ) and high spectral purity, even single longitudinal mode (SLM), nanosecond laser systems operating at 1 μm and 2 μm. High spectral purity, high energy nanosecond pulses are requested in many applications ranging from nonlinear optics frequency up- and down-conversion, high resolution spectroscopy, LIDAR and remote sensing.

The first laser system I had the opportunity to developed is a table-top pulsed Master Oscillator Power Amplifier (MOPA) laser originally intended as a part of a more complex laser system aimed to work as a transmitter for High Spectral Resolution LIDAR (HSRL) applications. The main specifications required for the laser system I developed were:

- Operating wavelength 1064 nm.
- Optical bandwidth $<$ 100 MHz (SLM).
- Pulse duration $>$ 10 ns.
- Pulse energy $>$ 1 mJ.
- Low energy pulse monitor at 1 kHz.
- High energy pulse repetition rate up to 100 Hz.
- Very good spatial beam quality ($M^2 < 1.5$).
- Compact foot-print (table-top).

Given the very demanding specifications in terms of both spectral and spatial quality, and high pulse energy, we opted for a MOPA architecture based on a high quality, compact, low-energy seeder and a suitable number of amplifiers. As a seeder we designed and built a Nd:YVO_4 microchip laser operating in the gain switching regime. This choice resulted in a very compact and simple seeder architecture (a monolithic cavity of few mm of length) which produced SLM nanosecond pulses (13 ns duration) at the requested 1 kHz repetition rate. The

gain switching technique has the main drawback of producing low-energy pulses: in our case the pulse energy available from the seeder was as low as 80 nJ. This required a careful design of a multi-stage, high-gain amplification chain. The first amplification stage consisted of a longitudinally CW diode-pumped, double-pass Nd:YVO_4 amplifier which increased the pulse energy to 12 μJ (gain of about 21 dB). After this amplifier, we opted for a two stages, Quasi-CW diode-side-pumped Nd:YVO_4 amplifier operating at 100 Hz which boosted the energy to the mJ level. The final output pulses had energy of 3,2 mJ with 13 ns duration and an optical bandwidth of 63 MHz, corresponding to a time-bandwidth product of about 0,8, close to the Fourier limit for a Gaussian pulse temporal profile.

This MOPA laser was employed as a pump source for a nonlinear optics experiment consisting in the demonstration of Raman conversion in the visible with a $4\times4\times30$ mm^3 $SrWO_4$ crystal. This material provides a Raman gain of about 5 cm/GW at 1064 nm pump wavelength. The gain is as high as 16 cm/GW, if pumped at 532 nm. For this reason, we decided to pump with the second harmonic (SH) of the MOPA laser. The maximum available pump energy at 532 nm was 1,5 mJ. Pump pulse duration was 11 ns after SH generation in a 5-mm-long type-II KTP crystal. The pump pulses at 532 nm were SLM and with almost diffraction limited spatial beam quality (M^2 = 1.1). The high parallelism of the Raman crystal facets permitted to exploit a low-finesse (facets Fresnel reflectivity was about 9%) cavity effect to further reduce the Stimulated Raman Scattering (SRS) threshold. A SRS threshold as low as 0.4 mJ (100 MW/cm^2 corresponding pump intensity) was obtained. The Raman shifted pulses at 559 nm showed a duration of 3,3 ns and a maximum energy of about 0,17 mJ, corresponding to a high peak power of about 50 kW. The beam quality was well preserved (M^2 = 1.3). We also carefully characterized the longitudinal mode content of the Raman shifted pulses. About 15% of the generated pulses resulted SLM, the remaining 85% contained only two or seldom three longitudinal modes, confirming the very high spectral purity of the Raman generated pulses.

During the second year of my PhD, I took part in a 6-month research activity at KTH Royal Institute of Technology in Stockholm, Sweden, from February 2017 to July 2017, when I was hosted by the Laser Physics group of the Department of Applied Physics at the School of Engineering Sciences. During this research activity I had the opportunity to take part in a project aimed to build a tunable double-wavelength nanosecond excitation source, with pulse

energies in the range of tens of mJ. This rather complex MOPA laser system was intended to be a universal laboratory source for testing different THz platforms which were developed in parallel by other colleagues at KTH.

In order to achieve higher power conversion efficiency in THz generation the tunable source was designed to operate in the spectral range around 2 μm providing two wavelengths close enough to permit THz generation through difference frequency generation in proper nonlinear materials. Moreover, this wavelength range (2 μm) opens the possibility to exploit large range of THz generating media, including semiconductor platforms, which were the target of the project.

The architecture chosen for the 2-μm laser source was an Optical Parametric Oscillator (OPO) followed by an Optical Parametric Amplifier (OPA) both pumped at 1 μm, since this was the most practical solution for achieving the required pulse energies in the spectral range of interest. The tunable source employed as nonlinear crystals specially designed quasi-phase-matched (QPM) structures in Rb:$KTiOPO_4$ directly produced at KTH. The pump laser at 1 μm for the optical parametric source was a commercial injection-seeded, single-longitudinal mode laser at 1064 nm with a maximum output energy of about 150 mJ (InnoLas Laser GmbH) and was available for the experiments at the laser lab at KTH.

The OPO was realized with a plane-concave Fabry-Perot cavity. The plane cavity output coupler was a chirped Volume Bragg Grating (VBG) with a peak reflectivity at 2130 nm. The peculiarity of this VBG was its central reflective wavelength that could be tuned by moving it orthogonally to the incoming beam, specifically in a range of $\pm$ 10nm from the central wavelength.

The maximum output energy of the OPO was 1,5 mJ with a pump of 7 mJ, corresponding to about 5% of the available pump energy, the remaining 95% being used to pump the OPA. The maximum pump energy level for the oscillator was dictated by the damage threshold of the VBG which was the most delicate component of the OPO. The measurements confirmed the theoretical expectations as the source generated narrowband pulses (7 ns with 0,4 nm FWHM optical bandwidth) that could be tuned in a range of 1,5 THz around the degeneracy wavelength of 2128,4 nm.

In the OPA we used the same nonlinear material used for the OPO (PP-RKTP). At the end

of the amplification chain we obtained 52 mJ total energy (signal+idler) at 2 μm with a tuning range of about 21 nm (1,5 THz). The 7,5 ns pulses showed an optical bandwidth of 36 GHz and a fairly good beam quality. THz generation experiments using this excitation source are ongoing at KTH.

During the final year of my PhD I focused my research activity on high-energy (multi-mJ), Q-switched nanosecond laser oscillators architecture suitable to be employed in remote sensing and military applications. This kind of applications are usually very demanding for what concerns the robustness of the laser, since it is supposed to be working in harsh conditions. In all these applications, the laser can be subject to strong accelerations, vibrations and high temperature variations that can heavily affect resonator alignment and laser components functioning. Therefore, it is very important to adopt simple laser architectures, employing few, well tested and technologically mature components, and proper design strategies to make the resonator functioning less sensitive to the environmental conditions.

To this purpose, Porro prisms have been widely employed in substitution of usual flat or concave mirrors in Fabry-Perot resonators. Porro prisms are retro-reflecting prisms with 90°-cut reflecting surfaces that allow the laser beam to be reflected into the same direction where it comes from, up to a small angle of misalignment from the normal of the input plane face of the prism. Since Porro prisms induce polarization phase change in the incoming beam, this effect must be modeled and taken into proper account when the resonator is designed, in particular when polarization-sensitive components are used in the laser. This analysis is usually done by means of a Jones matrixes analysis of the resonator.

The laser source I designed and characterized was a multi-mJ, side-pumped Nd:YAG Q-Switched nanosecond laser originally intended as a possible seeder for a more complex MOPA laser at 1064 nm for a space-borne atmospheric LIDAR. For this reason, a special attention was devoted to the identification of a simple pump configuration and resonator geometry still offering a reasonably good beam quality and effective mitigation of misalignment sensitivity. To this purpose, I investigated both a Passively Q-switched (PQS) and an Electro-Optical Modulator (EOM) Actively Q-Switched (AQS) resonator configurations. The interest in these two different Q-switching techniques is motivated by the trade-off required from the specific application, i.e., generally AQS can provide higher energies as well as a higher pulse-to-pulse

jitter stabilization, whereas PQS architectures generally are far simpler and therefore more cost-effective and reliable.

The characterization of the laser I realized is comprehensive of a spatial and spectral beam quality analysis, a detailed characterization of the misalignment tolerance guranteeed by the Porro prism resonator, as well as measurements of the output pulse energy, jitter and beam pointing stability. For the PQS experiments, two different Cr:YAG saturable absorbers with different initial transmission $T_0 = 90\%$ and 70% were employed. Best results in terms of output pulse energy were obtained with the $T_0 = 70\%$ saturable absorber, yielding 7-mJ, 46-ns pulses (150 kW peak power). The active Q-Switching is achieved with a double $7\times7\times5$ mm^3 thermal matched RTP Pockels cell with a half-wavelength voltage of 2,4 kV. A maximum pulse energy of 10,5 mJ, with a corresponding pulse duration of 39 ns was obtained (250 kW peak power).

Part of the results I obtained in the research I carried out during my PhD have been published on peer-reviewed international journals and presented at international conferences. A detail of the publications and international conferences communications is reported here.

Articles on peer-reviewed international journals

1. **L. Fregnani**, P. Farinello, F. Pirzio, X. Zahng, V. Petrov and A. Agnesi, *"Threshold reduction and mode selection with uncoated Raman crystal acting as a low-finesse cavity"*, Appl. Opt. 56, 662-665 (2017).

2. R.S. Coetzee, X. Zheng, **L. Fregnani**, F. Laurell and V. Pasiskevicius *"Narrowband, tunable, 2 μm optical paremetric master-oscillator power amplifier with large-aperture periodically poled Rb:KTP"*, Applied Physics B (2018) 124:124 https://doi.org/10.1007/s00340-018-6992-z

International conferences communications

1. P. Farinello, **L. Fregnani**, F. Pirzio, S. Dell'Acqua, G. Piccinno, and A. Agnesi, *"High-energy single longitudinal mode MOPA laser system at 1064 nm"*, 7^{th} EPS Europhoton Conference 2016, Vienna.

2. **L. Fregnani**, F. Pirzio, G. Piccinno and A. Agnesi, *"Multi-mJ, side-pumped, polarization coupled Nd:YAG Porro-prism laser in active and passive Q-switching regime"*, 8^{th} EPS Europhoton conference 2018, Barcellona.

3. R. Coetzee, X. Zheng, **L. Fregnani**, F. Laurell, and V. Pasiskevicius, *"Narrowband, tunable, 2 μm optical parametric master oscillator power amplifier with large-aperture periodically poled Rb:KTP"*, 8^{th} EPS Europhoton conference 2018, Barcellona.

List of the Seminars, Courses and Summer Schools attended during my PhD

- Linguaggi problemi e metodi della comunicazione scientifica. 8 CFU
- Frontiers of solid state light sources, Europhoton conference 2016, Vienna. 2,1 CFU
- Current and future short-range channel access. 0,8 CFU
- Cognitive radio and dynamic spectrum access. 0,8 CFU
- 3D mapping by drones. 6 CFU
- Tensor flow, a short course for PhD students. 4 CFU
- Frontiers of solid state light sources, Europhoton conference 2018, Barcelona. 1,6 CFU
- EWT and other survival tactics. 1 CFU
- seminars 8 CFU

1. Introduction

A large variety of applications ranging from material processing [1][2][3][4][5], to medicine [6][7][8][9], from optical communications [10][11][12], to environmental monitoring [13][14][15], from spectroscopy [16][17][18][19][20], to nonlinear optics [21][22][23][24][25] just to name a few, are made possible by solid-state pulsed laser sources.

In many cases, the most important single parameter that has the largest impact on the potential application of the laser is the pulse peak power $P_{peak} \propto \frac{E_p}{\tau_p}$ (being E_p the pulse energy and τ_p the pulse duration) that can be realized in the spectral window requested by the specific application. Higher peak power traduces in the possibility of reaching higher local optical field intensity when the light beam is focused on the target, thus enabling special radiation-matter interactions exploited in all those exciting applications made possible only by laser technologies.

Pulse peak power can be increased either augmenting the pulse energy, usually adopting the master oscillator power amplifier (MOPA) architecture, thanks to its flexibility, intrinsic modularity and efficiency, or by developing laser sources able to deliver shorter and shorter pulses. The possibility to obtain extremely high peak powers without the need for very high pulse energy is one (surely not the only one!) reason for the huge success of ultrafast (picosecond and femtosecond) lasers. As an example, a 1-W diode-pumped solid-state femtosecond laser working at tens of MHz repetition rate and delivering 100-fs-long pulses with only few nJ of energy (typical numbers for a low power Yb-doped femtosecond laser, for example), already delivers tens of kW peak power pulses. The same peak power from a 10-ns laser, would require a pulse energy of $\sim 100\ \mu$J, which would result in kW (!) average power at tens of MHz repetition rate! This example should clarify the great benefit that may come from ultrashort pulses.

However, in many practical situations, the requisite of high peak power comes in combination with strict requirements for what concerns the spectral purity, i.e. the optical bandwidth, of the laser pulses. Since a Fourier-transform relation exists between the optical pulse duration τ_p and the optical bandwidth $\Delta\nu_p$, so that in practice $\Delta\nu_p\tau_p \sim 1$, the condition on the spectral purity traduces in a minimum acceptable pulse duration.

Therefore, tens of nanosecond pulses (which are considered relatively long in the optical domain), are required in all those applications where the optical bandwidth must be very narrow, in the range of tens of MHz. This is the case in many nonlinear optics and remote sensing applications.

This is the framework in which is inserted the research activity described in this thesis, since during my PhD I had the opportunity to work on the development of two rather complex and challenging high-energy, high-spectral-purity, nanosecond MOPA systems operating at 1 and 2 μm respectively.

The detailed description of the MOPA laser operating at 1 μm is reported in Chapter 2. This table-top laser system was developed as a part of a more complex laser system intended for High Spectral Resolution LIDAR (HSRL) applications. In this case, the strict requirement about spectral purity of the laser (optical bandwidth $<$ 100 MHz) is a consequence of the application targeted, which was the remote measurement of wind velocity through the discrimination of a Doppler-shift in the spectrum of the radiation back-scattered by aerosol particles. The energy required for the HSRL application was as high as 200 mJ, thus requiring a multi-stage MOPA design. I personally took part on the development of the master oscillator and the high-gain amplification stages up to the mJ level, whereas the design and development of the final booster amplifier was part of another PhD student research and it is not described in this thesis. Nevertheless, the peculiar characteristics of the laser system were successfully exploited in nonlinear optics experiments, namely Stimulated Raman Scattering (SRS) in the visible employing a $SrWO_4$ crystal, as described in Section 2.11.

In Chapter 3 it is described the research activity I carried out at the Laser Physics Lab of KTH in Stockholm during a six months visiting period. The project I was involved in was aimed to the realization of a tunable double-wavelength nanosecond excitation source with pulse energies in the range of tens of mJ which would be a universal laboratory source for

testing different THz platforms. In order to achieve higher conversion efficiency in THz generation, the tunable source was designed to operate in the spectral range around 2 μm generating two wavelengths close enough to permit THz generation through difference frequency generation in proper nonlinear materials. Moreover, this wavelength range opens the possibility to exploit a large variety of THz generating media, including semiconductor platforms, which was the target of the project. The architecture chosen for the 2-μm laser source was an Optical Parametric Oscillator (OPO) followed by an Optical Parametric Amplifier (OPA) both pumped at 1 μm, since this was the most practical solution for achieving the required pulse energies in the spectral range of interest.

After an intense activity in developing complex MOPA laser systems operating in different regimes and wavelength regions, I had the opportunity to focus more on the direct generation of mJ-level nanosecond pulses in diode-pumped oscillators. In particular, my research was focused on the identification of practical solutions for nanosecond Q-switched sources suitable to be employed in remote sensing and military applications. This kind of applications are usually very demanding for what concerns the robustness of the laser, since it is supposed to be working in harsh conditions. Therefore, it is very important to adopt simple laser architectures, employing few, well tested and technologically mature components, and proper design strategies to make the resonator functioning less sensitive to the environmental conditions. To this purpose, in stead of the traditional standing-wave Fabry-Perot resonators employing plane or curved end-mirrors, I investigated resonators employing Porro prisms as end-mirrors. This solution permits an effective mitigation of the misalignment sensitivity of the laser at an expense of a relatively more complex resonator design and a slight reduction in laser efficiency and spatial beam quality. The results of this research activity are reported in Chapter 4.

2. High energy 1-μm MOPA laser system for HSRL and nonlinear optics

2.1 Laser system specifications

High energy, single longitudinal mode (SLM) lasers are irreplaceable tools for many different applications requiring good beam quality, narrow linewidth, and long coherence length, such as remote sensing, LIDAR and high resolution spectroscopy [26]. Master Oscillator Power Amplifier (MOPA) is the most exploited architecture for this kind of laser systems, thanks to its flexibility, intrinsic modularity and efficiency. Owing to the well-developed Nd-doped high gain amplification modules technology [27][28], 1064 nm is the natural wavelength for the MOPA system. The good spatial beam quality, high spectral purity, and high pulse peak power provided by the laser permit an efficient nonlinear frequency up or down-conversion to match the specific wavelength required by the application.

In this chapter I will describe the design and realization of a table-top pulsed MOPA laser, developed as a part of a more complex laser system intended for High Spectral Resolution LIDAR (HSRL) applications. A brief overview on LIDAR technology and HSRL systems is given in Section 2.3. The main specification required for the laser system were:

- Operating wavelength 1064 nm.
- Optical bandwidth $<$ 100 MHz (SLM).
- Pulse duration $>$ 10 ns.
- Pulse energy $>$ 1 mJ.

- Low energy pulse monitor at 1 kHz.
- High energy pulse repetition rate up to 100 Hz.
- Very good spatial beam quality ($M^2 < 1.5$).
- Compact foot-print (table-top).

The architecture of the laser system, with the motivation of the main design choices for the building blocks will be described in Section 2.2, the characterization of the building blocks and the whole MOPA laser system I built is presented in Section 2.7, 2.8, 2.9.

In Section 2.11 I describe the setup and the experimental results obtained employing this MOPA laser as the pump source for a nonlinear optics experiment consisting in the demonstration of Raman conversion in the visible with a $SrWO_4$ crystal.

2.2 Design overview

The specifications for this laser system operating at 1 μm were very demanding both in terms of the required pulse energy and the spectral purity, corresponding to a SLM pulsed regime. SLM operation can be relatively easily obtained by employing short resonators (microchip lasers), where the frequency separation of the cavity axial modes, the so-called Free Spectral Range FSR=c/2L (being c the speed of light and L the optical length of the cavity) becomes larger or comparable to the gain bandwidth of the active medium, thus preventing the possibility of simultaneous oscillation of more than one resonator longitudinal mode. Microchip lasers can be pulsed by means of two main techniques, namely, Q-Switching and gain switching. In laser materials offering high upper level energy storage capability, i.e. long fluorescence lifetime, such as rare earth doped crystals Nd:YAG and Nd:YVO_4, Q-Switching is usually the more convenient regime to generate energetic pulses. Unfortunately, in Q-Switching regime, pulse duration is proportional to the cavity length and the extreme compactness of microchip lasers (cavity $<$ 1 cm) results in very short, usually sub-ns pulse duration. This limitation can be overcome with gain switching technique, since with this technique, even very short microchip resonators can produce laser pulses with duration longer then 10 ns in SLM regime.

The major drawback in the gain switching pulse generation is its intrinsic low output energy, usually in the range of few tens of nJ, which transfers part of the complexity of the design from the oscillator to the proper amplification chain.

The architecture we decided to implement for this laser system was, therefore, a multi-stage, MOPA laser system with a Nd:YVO_4 micro-chip laser in gain switching regime as a master oscillator and a two-stages Nd:YVO_4 power amplifier chain. Even if the repetition rate requested for the mJ-level amplified pulses was 100 Hz, the low energy seeder was supposed to work at 1 kHz repetition rate to provide a signal monitor for the electronics at this higher rate. Given the very low pulse energy available out of the gain-switched seeder, this signal was not ideal for the monitoring purposes, therefore we opted for a first amplification stage operated in cw to initially increase the pulse energy at 1 kHz repetition rate. For the booster amplification stage, given the low repetition rate of 100 Hz, the natural choice was a QCW diode pumped amplifier. In this way, we could take advantage of the high gain available pumping with 150-W peak power QCW diode array at 808 nm. Proper synchronization of the different amplification stages was realized by means of an external commercial pulse generator (Berkley Nucleonics BNC 565) providing the properly delayed enabling signals for the seeder fast modulated pump diode and the QCW diode pumped final amplification heads. The schematic representation of the architecture of the system is shown in Fig. 2.1.

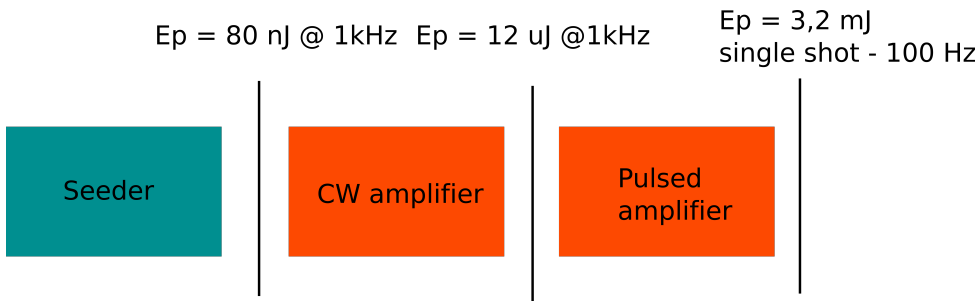

Figure 2.1: Schematics of the output power and energy at every step

2.3 High Spectral Resolution Lidar

LIDAR (LIght Detection And Ranging) is a measurement technique based on the illumination of a specific target by a laser pulse and the measurement of the backscattered signal. LIDARs

can work with different configurations and therefore can measure different parameters of the target. Time of flight LIDAR are the most common. In this case laser pulses are sent to a target and a receiver measures the amount of time it takes for the pulses to be reflected or scattered back to the source. From this information, the system retrieves the information about the distance of the target from the source. By analyzing the back-scattered signal as a function of time, 3d maps can be realized with this technique. But a signal analysis in the time domain is not the only possible source of information from a LIDAR system. If also the optical spectrum of the back-scattered signal can be measured, many more information can be made available. This is what happens in one of the most common area of application of LIDAR systems which is the atmospheric monitoring. In this case, for example, Raman scattering is used to identify the presence and concentration of specific molecules in the atmosphere (usually pollutants). Given the relatively large spectral shift provided by Raman scattering, the spectral purity of the laser source is not so crucial in this atmospheric LIDAR. A very challenging, but very important measurement that can be done with a LIDAR system, is the measurement of velocity of wind, or in general the velocity of aerosol in the atmosphere. To target this application, the so-called High Spectral Resolution Lidar (HSRL) must be developed. Indeed, the physical effect used in this kind of measurements is Doppler effect, responsible for a velocity dependent, frequency shift in the back-scattered radiation collected by the LIDAR receiver.

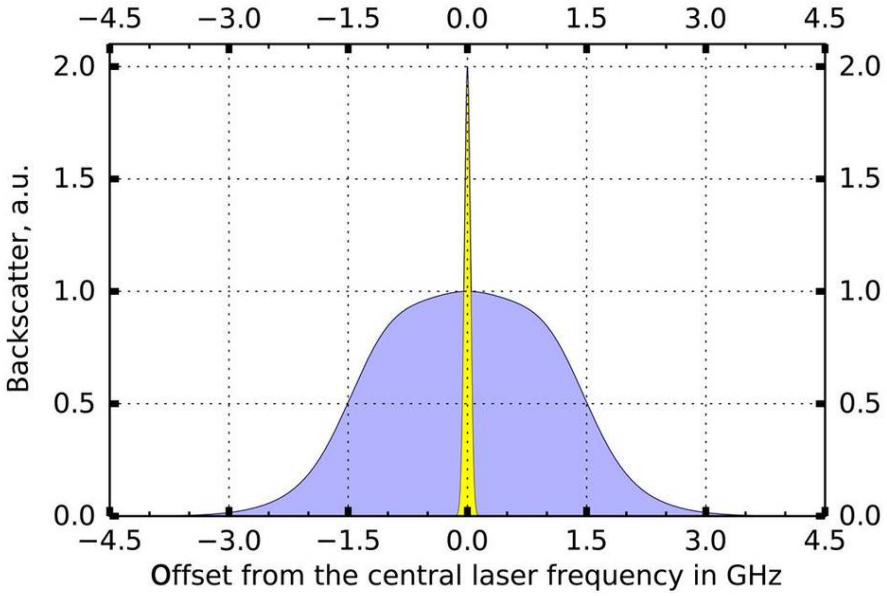

Figure 2.2: Spectrum of the scattered pulse as it can be resolved by a HSRL

In particular it becomes critical to be able to distinguish between the signal produced by the random thermal motion of the molecules and the signal generated by the particles that are moving with the speed of the wind. The typical shape of the scattered radiation is represented in Fig. 2.2, where the two contributions can be easily distinguished because of the very different associated bandwidths (particles $\rightarrow$ tens of MHz, molecular scattering $\rightarrow$ few GHz). This is possible only if the receiver has a very narrow bandwidth tunable filter (much narrower than the molecular response shown in Fig. 2.2), and the laser excitation source has a very narrow bandwidth, comparable with the bandwidth of the signal produced by particle scattering. More details about LIDAR in general and HSRL technique can be found in [29].

2.4 Gain Switching

A detailed description of the Gain Switching dynamics can be found in [30]. To introduce the gain switching pulse generation it is worth describing the behavior of a four level laser system under the assumption that the transition between the upper energy levels and the lower laser levels takes place with duration relatively longer than the laser transition between the levels

2 and 1.

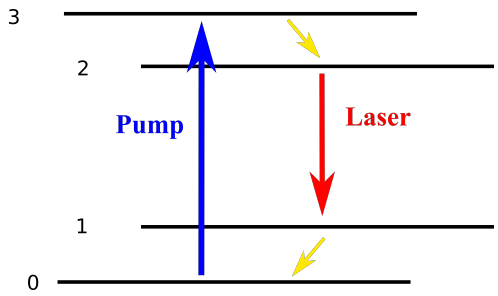

Figure 2.3: Scheme of a generic 4 level laser

If we define $n(t)$ as the population inversion density and $\phi(t)$ as the photon density inside the resonator, the dynamic behavior of a four-level system can be described by the equations

$$\begin{cases} \frac{\partial n}{\partial t} = R_p - \sigma_e c \phi n - \frac{n}{\tau_f} \\ \frac{\partial \phi}{\partial t} = \sigma_e c \phi n - \frac{\phi}{\tau_c} \end{cases} \tag{2.1}$$

Where R_p is the pump rate, σ_e is the emission cross section at the laser wavelength, τ_f is the fluorescence time, i.e. the decay time of the upper laser level to the lower laser level due to radiative transition and τ_c is the photon lifetime which depends on the length of the cavity as well as its intrinsic losses and its output coupling.

The second term of the first equation (and the first term of the second) quantifies the stimulated emission due to the laser photons. Equation 2.1 holds as long as the transient time between the ground level and the first laser level and the transition between the upper level and the upper laser level are both relatively faster then the fluorescence time, as it is the case in practical situations.

2.4.1 Relaxation oscillations

If we consider a continuous pump which instantaneously reaches its threshold value, i.e. a *step function* pump, the term R_P in the first equation of the system 2.1 becomes equal to 0. Moreover, if the analysis is applied to short time span it is also possible to neglect the term depending on the spontaneous emission that usually takes place in longer time span, therefore

equation 2.1 becomes

$$\begin{cases} \frac{\partial n}{\partial t} = -\sigma_e c \phi n \\ \frac{\partial \phi}{\partial t} = \sigma_e c \phi n \end{cases} \tag{2.2}$$

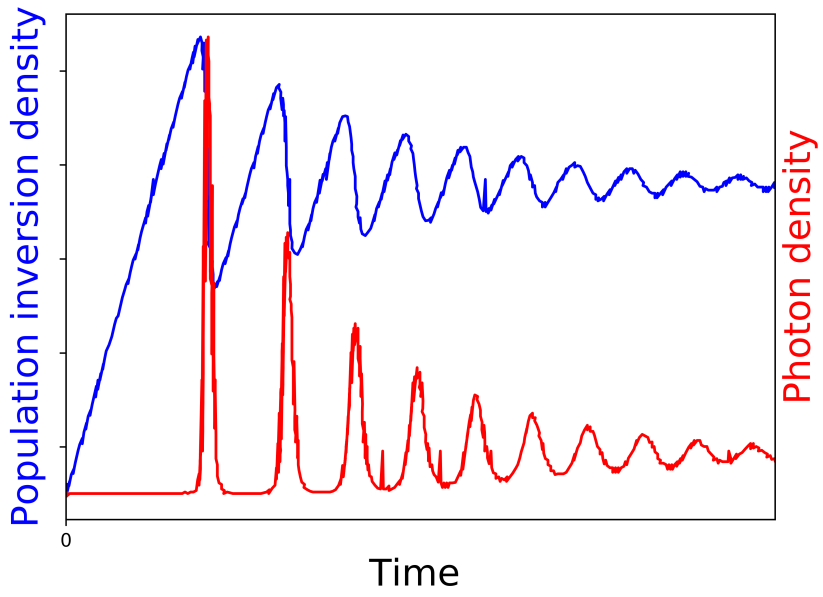

Figure 2.4: Evolution of the population inversion density and the photon density in response to a step function pump

As it can be seen in Fig. 2.4, which represents the evolution of *n* and $\phi(t)$ in a four level system we can see a series of oscillations of the two variable of our interest.

To describe the process: at the time t=0 the inversion of population starts and the upper level of the laser transition starts to get filled, then, when the inversion exceeds the threshold value $n_{th} = 1/(c\sigma_e c)$, the number of photons intracavity starts to grow while simultaneously the inversion mechanism still takes place ($\partial n/\partial t > 0$ and $\partial \phi/\partial t > 0$); then, when the number of photons reaches a certain value (ϕ_0), the stimulated emission due to the laser photons becomes dominant over the pump and the inversion density starts to decrease ($\partial n/\partial t < 0$ and $\partial \phi/\partial t > 0$), until it falls below the threshold value n_{th}, then the photon density diminishes and reaching again ϕ_0, and the process repeats itself with a lower modulation depth, until the inversion population is stabilized to the threshold value.

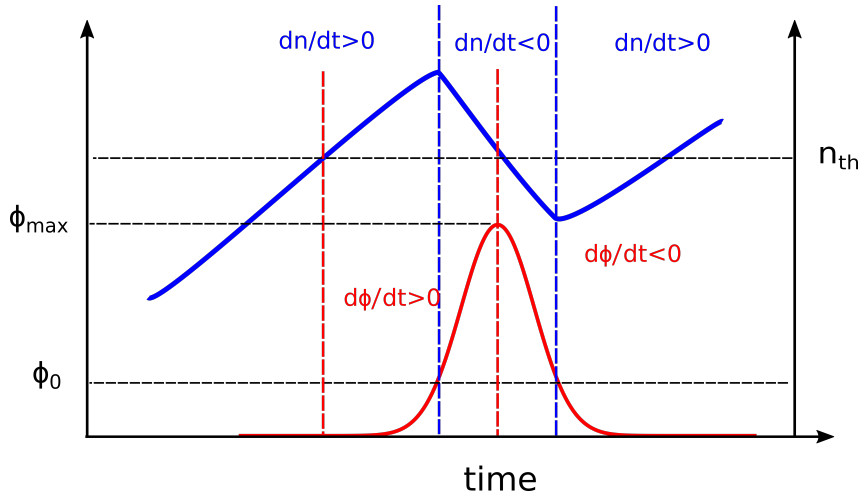

Figure 2.5: Evolution of the population inversion and of the photon density inside a laser cavity

If the pump pulse is *stopped* as soon as the first peak is generated it is possible for the laser to emit a short pulse whose duration depends on the characteristic of the material and on the pump pulse instead of the length of the optical resonator [30].

2.5 Microchip laser

Microchip laser are monolithic solid state laser where the whole cavity is made by the gain medium and the mirrors are substituted by the coatings of the crystal.

Microchip laser have been invented by J. J. Zayhowski and A. Mooradian [31] with the purpose of creating a simple and compact single longitudinal mode solid-state laser. Today they find use in various sectors such as automotive, biomedical, laser marking, telecommunications and environmental applications [32].

One of the obvious advantage of this architecture is the easiness of alignment. Because of their short length microchip lasers represent an excellent choice for sub-nanosecond Q-switched sources with a SESAM or Cr:YAG as a saturable absorber [33]. The most common material used as gain media are Nd:YAG and Nd:YVO_4 for generation in the 1 μm region. The seeder for the MOPA was a $2 \times 2 \times 1,5$ mm^3 Nd:YVO_4 1%-doped laser crystal with a coating that was HR for the laser wavelength and AR for the 808 nm pump. The coating on the output face was still AR for the pump and had a 97% reflectivity for the laser wavelength.

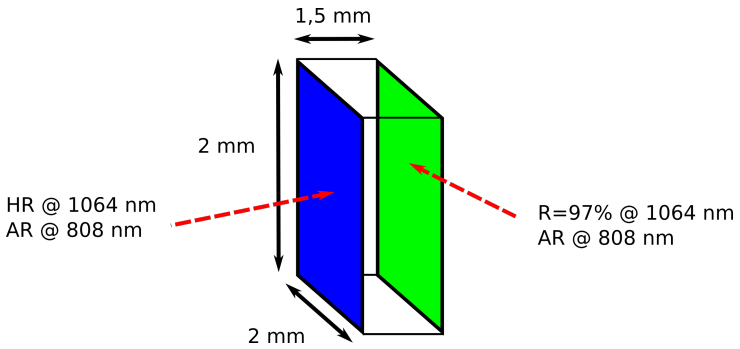

Figure 2.6: Nd:YVO_4 microchip laser employed in the MOPA

2.6 Seeder pump diode characterization

The pump diode is a BFP1 laser diode from Bright Solutions srl operating near 808 nm. The maximum output power at 1 kHz was $\sim$ 7 mW for a pulse duration of 500 ns corrispending to a max peak power of 14 W and a pulse energy of 7 μJ (see Fig. 2.7). The spectrum emitted by the laser diode was measured with a ANDO AQ6317B optical spectrum analyzer. The result of the measurement, repeated at different laser diode pulse repetition rate ranging from 100 Hz to 50 kHz is shown in Fig. 2.8. Given the extremely low duty cycle of operation no significant thermal drift of emitting pump wavelength was observed. The pump beam is coupled to a 100 μm core diameter optical fiber and then focused inside the crystal by means of a telescope.

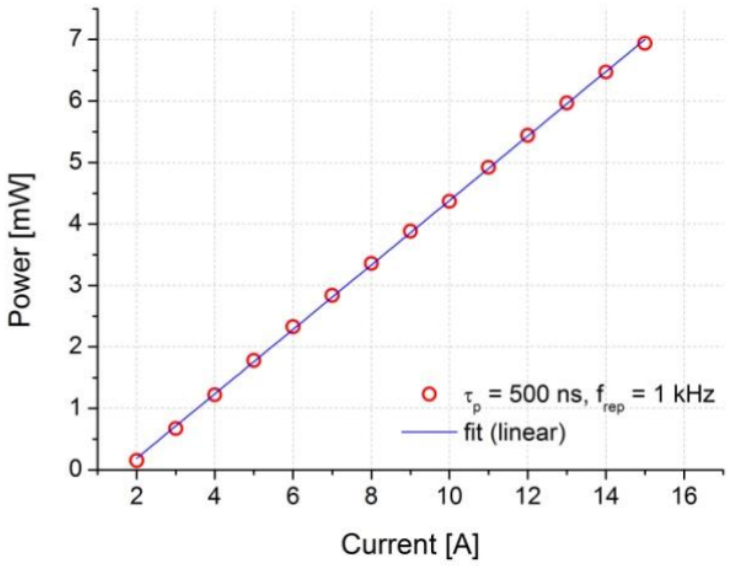

Figure 2.7: Output power of the BFP pump diode in function of its driving current

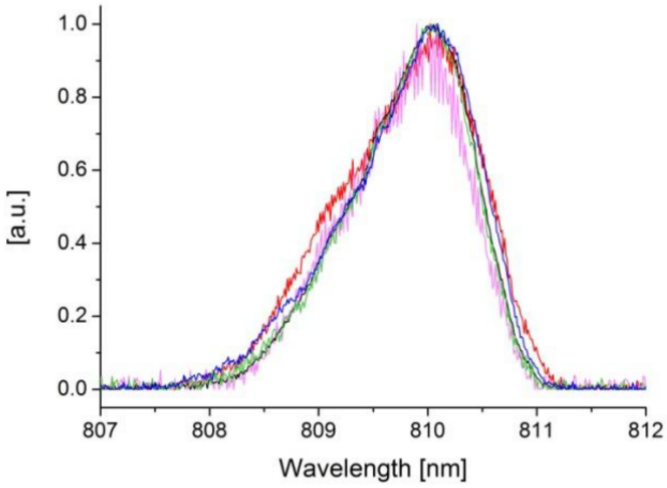

Figure 2.8: Optical spectrum of the BFP diode at different repetition rates

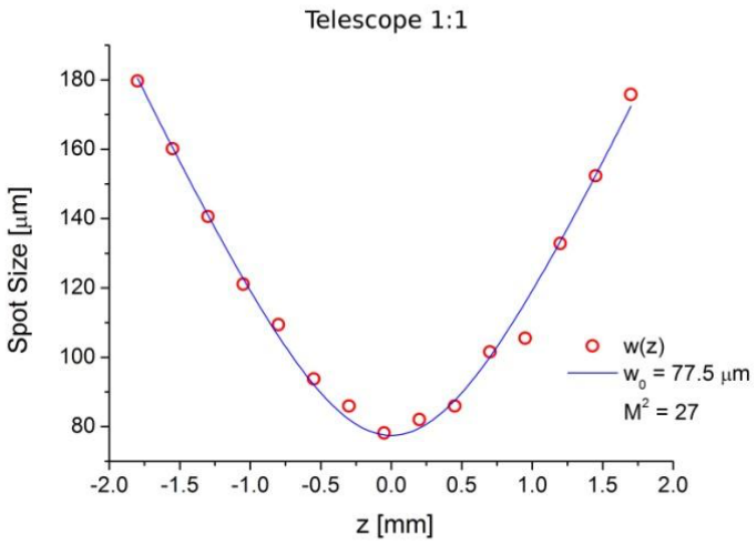

Figure 2.9: Spatial beam quality of the BFP1 pump diode

The spatial beam quality of the pump source was measured with the knife-edge technique. The result is shown in Fig. 2.9. The $M^2 \simeq 27$ is quite typical for the 100-μm multi-mode fiber. The pump radiation was imaged in the active medium with a 1:1 telescope.

2.7 Microchip seeder characterization

The design of the seeder stage with the reshaping optics and optical components, such as Faraday isolators, used to protect the gain-switched microchip laser from back-injection coming from subsequent amplification stages is shown in Fig. 2.10

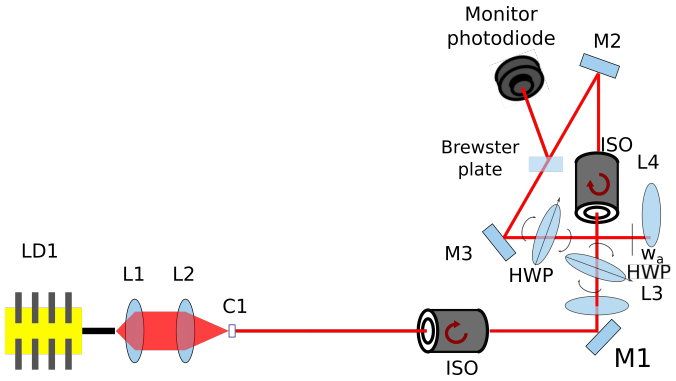

Figure 2.10: Design of the seeder stage. Two opto-isolators were inserted in the architecture in order to avoid any possible effect of self-lasing or back-injection

LD1	BFP1 Bright Solutions srl pulsed diode laser, 14 W max peak power at 808 nm coupled in a 100 μm optical fiber
L1	f=6,25 mm aspheric lens AR at 808 nm
L2	f=6,25 mm aspheric lens AR at 808 nm
C1	Nd:YVO_4 $2 \times 2 \times 1,5$ mm 1% doping R_{OC}=97%
M1,M4,M6,M7,M8	Dielectric mirror HR 45° at 1064 nm
L3	f=300 mm spherical lens
M2	Metallic mirror
M3	Metallic mirror
$\boldsymbol{w_a}$	0,82 mm beam waist on lens L4
L4	f=250 mm spherical lens
L3-M2	17 cm
M2-M3	25 cm
M3-L4	30 cm
HWP	Half wave-plate at 1064 nm

Table 2.1: List of the acronyms and distances in Fig. 2.10

The first step of the analysis was the characterization of the diode-pumped 1,5-mm-long Nd:YVO_4 laser seeder. Just outside the microchip an output power of 137 μW and a pulse

width of about 13 ns were measured. These values were obtained with a pump repetition rate of 1 kHz and with pump pulses of 500 ns of duration and 6 W of output peak power.

The spatial beam quality was measured by means of a CCD camera scanned along the focal plane of a spherical lens. The result is shown in Fig. 2.11. The $M_x^2 \times M_y^2 = 1,07 \times 1,05$ prove the almost diffraction limited beam quality of the gain-switched seeder. The central wavelength emitted by the seeder is 1063,9 nm as shown in Fig. 2.13. This unusually "short" wavelength can be justified by the extremely low pump duty cycle (0,05%) and correspondingly low thermal load of the active medium (incident average power of few mW).

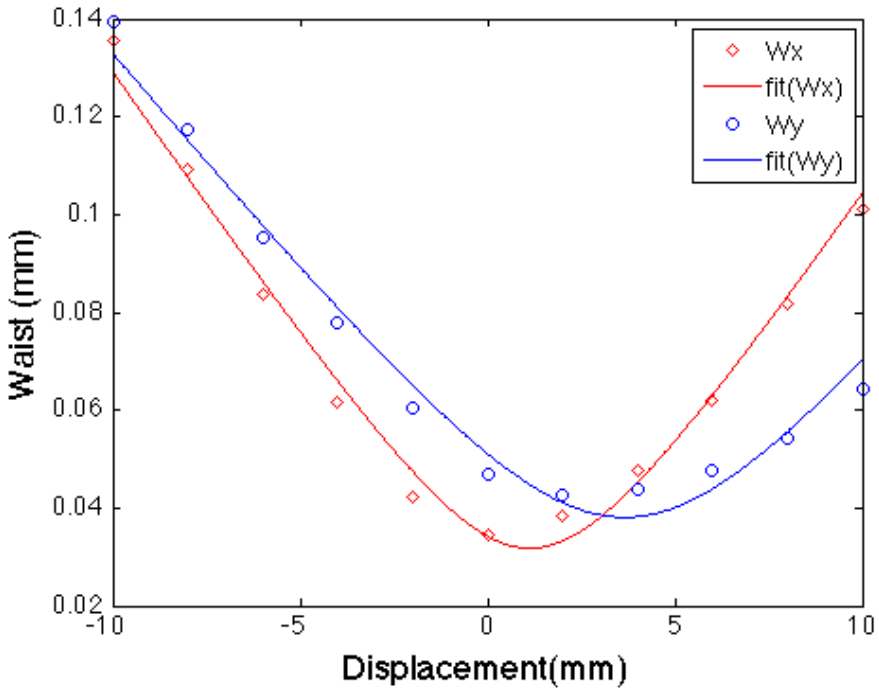

Figure 2.11: Seeder M^2 measurements (M_y^2 =1,05 M_x^2=1,07)

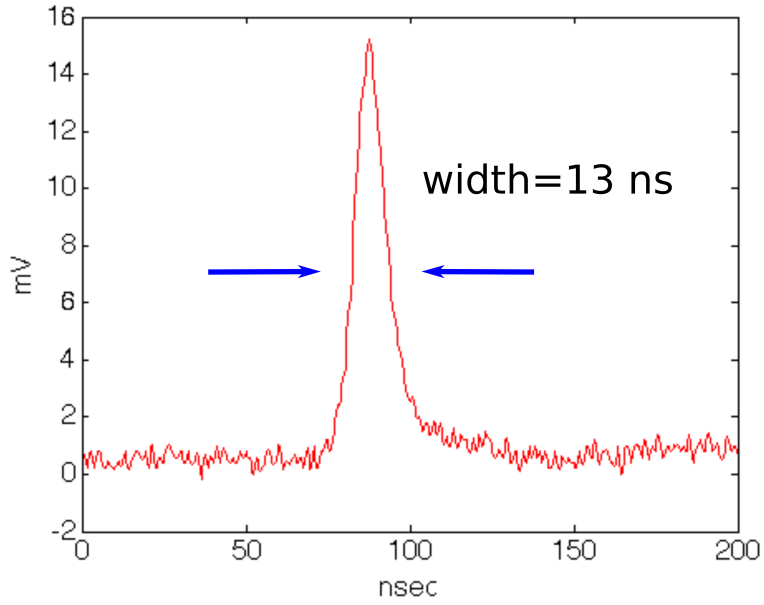

Figure 2.12: Seeder pulse measured with Tektronix digital phosphorus oscilloscope TDS5104B (1 GHz bandwidth)

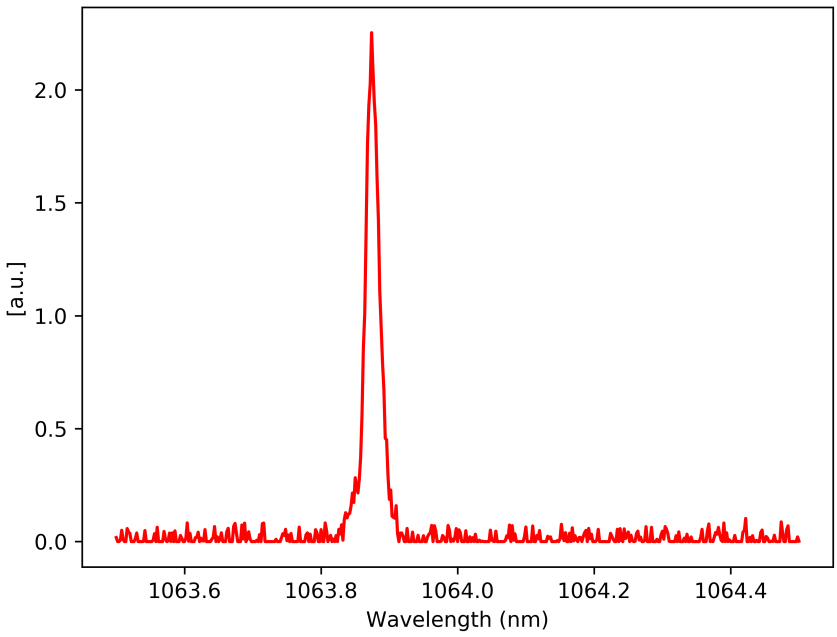

Figure 2.13: Spectrum of the seeder pulses taken with an ANDO AQ6317B spectrometer

2.8 CW-pumped amplification stage

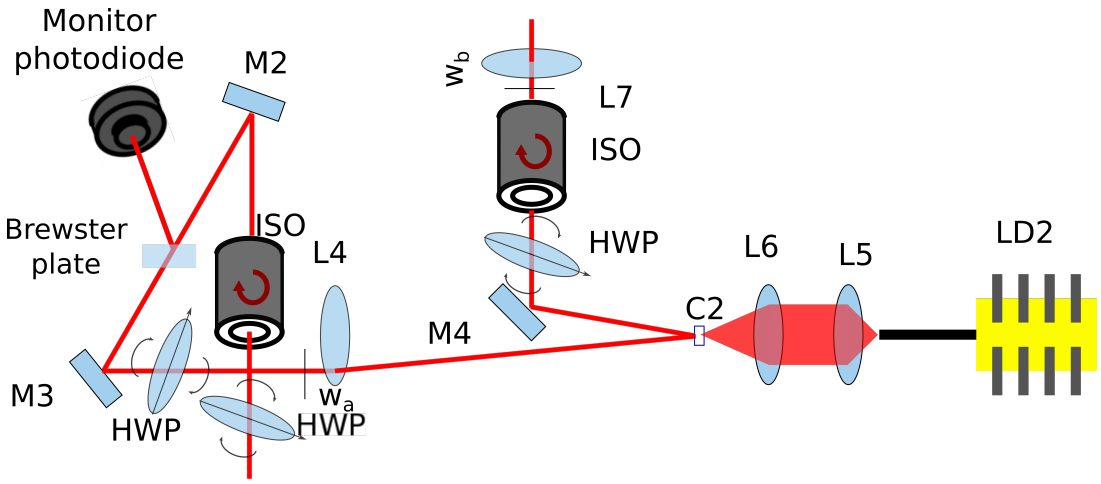

Figure 2.14: CW amplification setup

L4	f=250 mm achromatic lens
LD2	high power diode laser CW 20 W maximum power coupled in a 200 μm core diameter fiber
L5	f=30 mm achromatic lens
L6	f=40 mm achromatic lens
C2	Nd:YVO_4 0.3% doping $3 \times 3 \times 10$ mm^3 AR/AR
w_b	1,3 mm
L4-C2	25 cm
C2-M4	18,5 cm
M4- w_b	11 cm
L7	f=300 mm spherical lens

Table 2.2: List of the acronyms and distances in Fig. 2.14

The first stage of amplification was intended to increase the energy of the seeder thus easing the work of the last stage of amplification. The pump waist in the Nd:YVO_4 double pass amplifier was ≈ 133 μm due to a magnification of 4/3 made by an achromatic lens telescope. In

order to optimize the mode matching the seeder waist was decreased to $\approx 100\ \mu$m. The thermal management of the Nd:YVO_4 amplification crystal was performed with a water cooled copper mount whose temperature was kept around 18°C. The pump diode of the first stage was a CW diode with a maximum output power of 20 W.

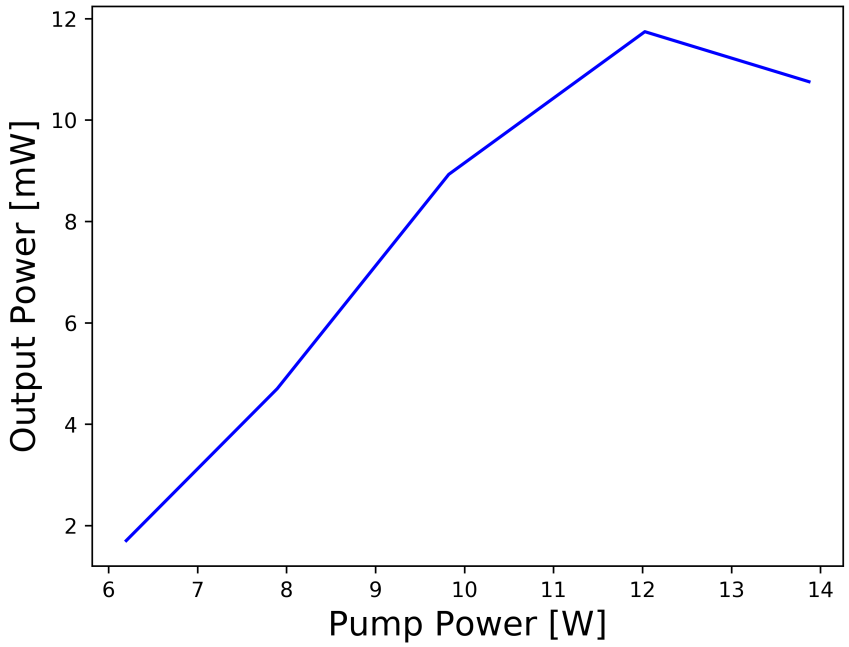

Figure 2.15: Output energy in function of the CW diode pump power

The maximum output power obtained was for 60% of the maximum current corresponding to 12,5 W incident pump power. Further increasing the pump power the pump energy dropped. We attribute this limitation to a thermal shift of the emission cross-section peak of the CW pumped Nd:YVO_4 amplifier. Indeed, as it can be seen in Fig. 2.16, if we compare the seeder spectrum with the fluorescence spectrum of the Nd:YVO_4 CW-pumped amplifier, we notice that increasing the pump power results in a progressive red shift of the gain peak wavelength, as expected by literature [34]. This mismatched between the seeder wavelength and the gain peak wavelength in the amplifier is unavoidable given the very small thermal load in the low duty cycle microchip laser.

It was also noted that a careful mounting of the amplifier crystal in its copper case was critical for the optimization of the output energy up to 18 μJ, as measured before the final

Faraday isolator in Fig. 2.14.

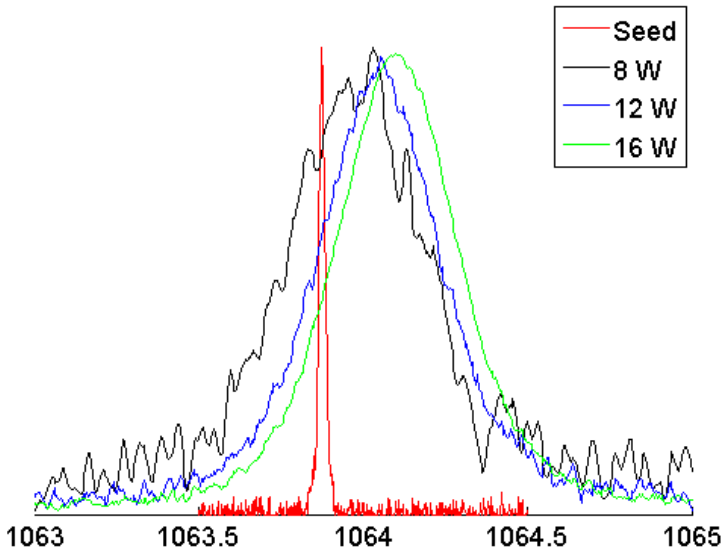

Figure 2.16: Spectrum of the seeder (red) and fluorescence spectrum of Nd:YVO_4 as measured at different pump power levels

An optical isolator was inserted between mirror M4 and lens L7 in order to avoid any retro-injection of the amplified beam inside the microchip. During the measurements of the output power the seeder pulse was monitored and it could be noticed that, in the absence of the optical isolator, as the pump power grew, an instability appeared in the seeder. The instability caused a certain number of pulses (about 5% out of 100 samples) to be reduced in amplitude and to have a longer duration (18 ns).

The seeder beam was then collimated with the lens L7 (see Fig. 2.14). The amplified beam was then collected with mirror M4. After the optical isolator a maximum energy of 12,3 μJ was measured. The unavoidable decrease in output energy caused by the optical isolator represented a necessary trade off to avoid any possible damage to the microchip and to increase the stability of the output pulses.

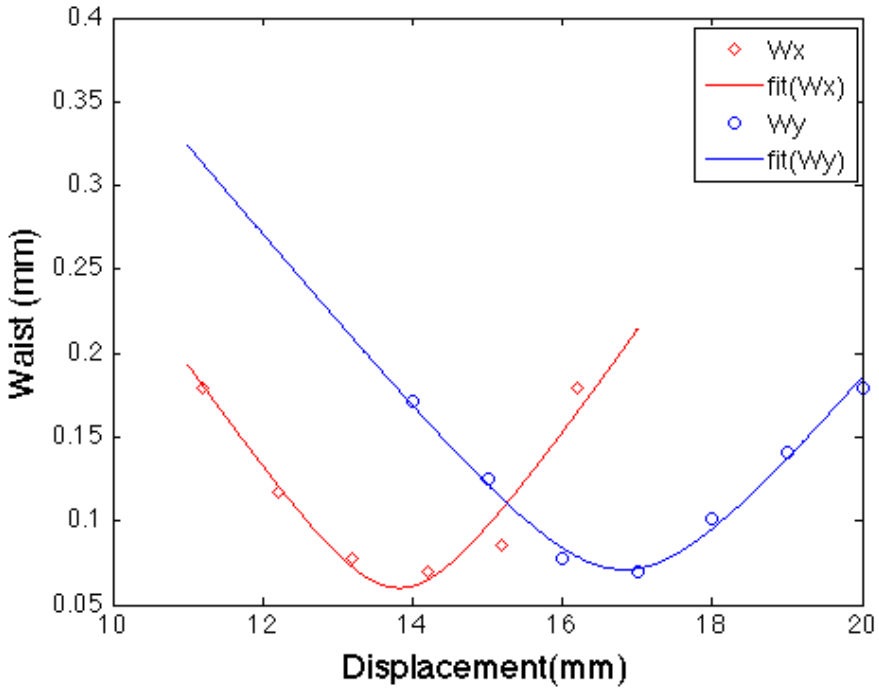

Figure 2.17: M^2 after the CW amplification M_y^2=1,15 M_x^2=1,14

We measured a beam quality of the CW amplified beam of $M_x^2 \times M_y^2 = 1,14 \times 1,15$. The result is shown in Fig. 2.17. The astigmatism was already present in the seed beam as it can be seen in Fig. 2.11.

The very good beam quality preservation in the double-pass CW-pumped amplifier was possible thanks to the careful adjustment of seed beam waist in the amplifier trading off energy extraction efficiency for beam quality preservation.

2.9 Quasi-CW pumped amplification stage

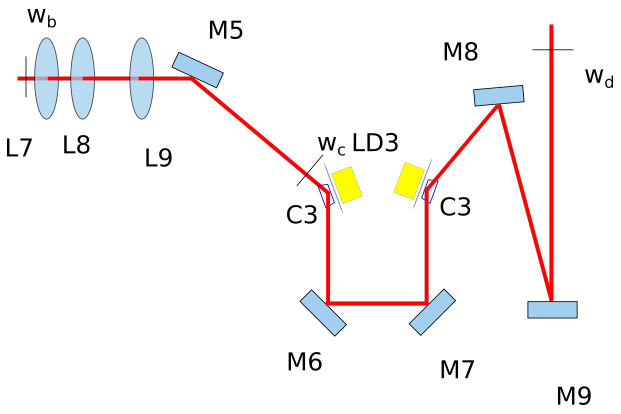

Figure 2.18: Quasi-CW amplification setup

w_b	1,3 mm
L7	f=300 mm spherical lens
L8	f=150 mm spherical lens
L9	f=-50 mm spherical lens
w_c	0,5 mm
M5	Metallic mirror
LD3	Quasi-CW high power (150 W) laser diodes
C3	$4 \times 2 \times 15$ mm^3 Nd:YVO_4 1% doped 6° wedged slab
M9	Dielectric mirror HR 0° at 1064 nm
w_d	0,5 mm
L8-L9	10 cm
L9-C3	17 cm
C3-C3	24 cm
C3-w_d	50 cm

Table 2.3: List of the acronyms and distances in fig 2.18

Before entering the second amplification stage the laser was collimated then resized with a spherical telescope to a beam radius of 0.5 mm. Just like in the CW amplification stage when the amplification started to increase (as the pulses reached 0,2 mJ of energy at 50 Hz) the same instability as before was seen in the seeder pulse. The same procedure as the one in the previous stage of amplification was applied and another optical isolator (the one between the Nd:YVO_4 and the mirror M1) was inserted.

The pump repetition rate of the second amplifier could be modified from single shot to 100 Hz, the width of the pump pulses was 100 μs and the peak power was 150 W at 160 A for a pump pulse energy of 15 mJ for each amplifier. The synchronization of the 1 kHz pulse train with the pump pulse train was controlled by a BNC 565 pulse delay generator. The input of the generator was given by a current monitor signal taken by the driver of diode LD1, then the output frequency was obtained by dividing the seeder frequency by a chosen value.

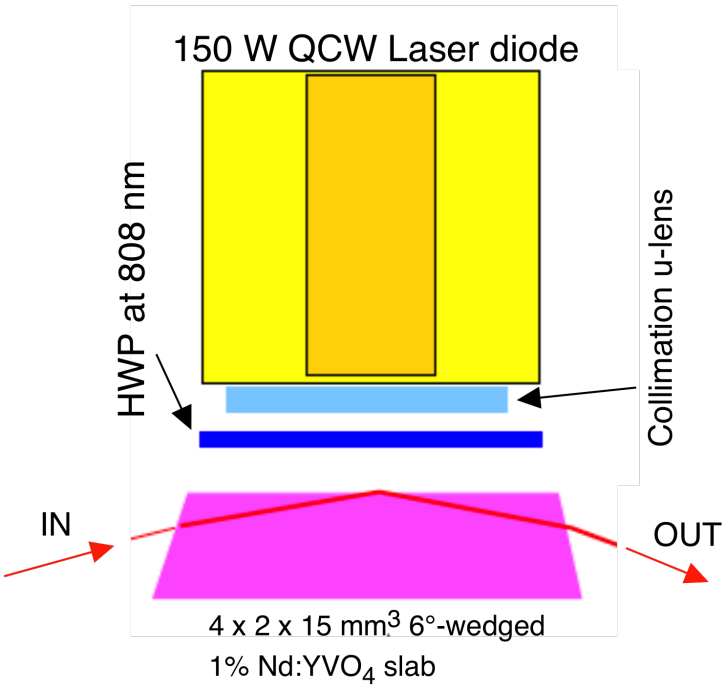

Figure 2.19: Grazing-incidence Nd:YVO_4 QCW laser diode pumped amplification head

The amplification stage is based on a couple of $4 \times 2 \times 15$ mm^3, Nd:YVO_4 slabs, 1%-doped, 6° wedge, in a grazing-incidence configuration. Each slab was pumped by a 150 W peak power quasi-cw laser diode array with emitting size 10 mm x ~ 1 μm, tuned at 808 nm and collimated

by a microlens to a vertical dimension $2w_y$ of 0.8 mm. The input and output faces of the slabs were antireflection-coated at 1064 nm, while the pump side was AR coated at 808 nm. Half-wave plates were used to align the polarization of the pump diode arrays with the Nd:YVO_4 c-axis (perpendicular to the plane of Fig. 2.19). The pump pulse duration was selected to 100 μs, matched to the active medium fluorescence lifetime, in order to maximize the amplifier gain. The grazing incidence, total internal reflection configuration permits to obtain very high gain (small signal gain $>$ 30 dB have been demonstrated with configurations similar to the one adopted here [35]), fully exploiting the high-peak power pump diode, still maintaining an excellent beam quality [35]. The strong gain shaping established by such extremely high gains makes the beam divergence basically dominated by diffraction from the gain aperture and nearly independent of the seed diameter. This effect may be responsible for the slight beam quality improvement we noticed after amplification, as it can be seen in the M^2 measurement result presented in Fig. 2.20.

Up to 50 Hz the maximum pulse energy was 3,2 mJ. At 100 Hz a power of 330 mW was obtained, but we noticed a drop in the output pulse energy from 3,2 to 2,5 mJ after around 30 minutes of operating time. This loss of energy was likely due to a thermal detuning of the QCW amplifier.

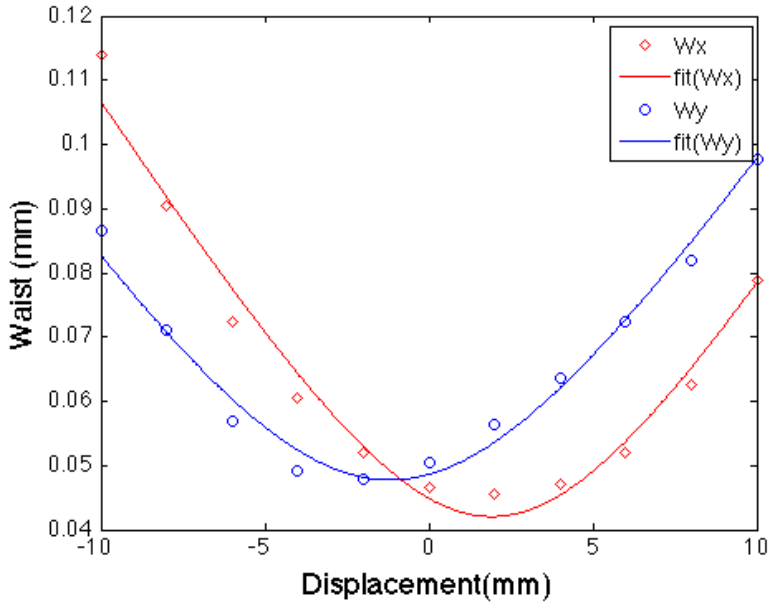

Figure 2.20: M^2 after the QCW amplification M_x^2 =1,07 M_y^2=1,05

2.10 Frequency stability measurements

In this section I report the spectral characterization of the seeder and the measurement of the stability of the bandwidth and the central output frequency. Because of the narrow bandwidth of the laser, the resolution of a general purpose optical spectrum analyzer such as the one available in our lab (ANDO AQ6317B) was not sufficient to obtain any usable information about the bandwidth of the pulses generated. It was then necessary to employ a scanning Fabry-perot interferometer, the model at our disposal was a Thorlabs SA210-8B.

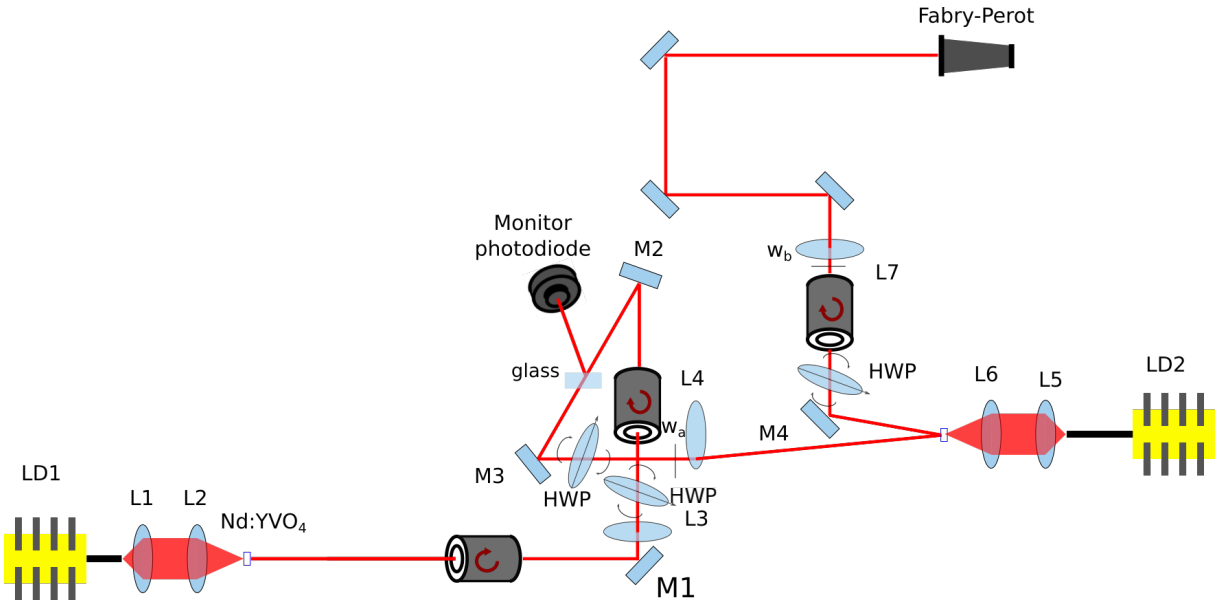

Figure 2.21: Schematics of the measurements taken with the Fabry-Perot scanning interferometer

A Fabry Perot interferometer is a frequency filter composed by two partially reflective mirrors with respective reflective coefficients R_1 and R_2. If we consider a monochromatic plane wave with amplitude E_i and wavelength λ it can be shown that the ratio between the amplitude of the transmitted electromagnetic wave and the incoming one is

$$T = \frac{|E_t|^2}{|E_i|^2} = \frac{1 + R_1R_2 - R_1 - R_2}{1 + R_1R_2 - 2\sqrt{R_1R_2}cos\delta} \tag{2.3}$$

where $\delta = 4\pi nL/\lambda + \phi_1 + \phi_2$ is the phase shift produced in a round-trip (including the phase shift ϕ_1 and ϕ_2 given by the two mirrors), L is the cavity length, n is the refractive index of the

medium between the two mirrors. If, as it is in most cases, R_1=R_2, eq. 2.3 becomes

$$T = \frac{(1-R)^2}{1+R^2-2Rcos(\delta)} \tag{2.4}$$

The ratio between T_{max} ($\delta = 2q\pi$ for $q = 0, \pm1, \pm2, ...$) and T_{min} ($\delta = 2q\pi + \pi$ for $q = 0, \pm1, \pm2, ...$) is called *coefficient of finesse* and is given by

$$F = 1 + \frac{4R}{(1-R)^2} \tag{2.5}$$

Since δ is linearly dependent on the frequency it is possible to define the so called *resonant frequencies* ν_q as

$$\nu_q = \frac{c}{2nL}\left(q - \frac{\phi_1 + \phi_2}{2\pi}\right) \tag{2.6}$$

and the distance between two consecutive resonant frequencies is called *Free Spectral Range* **FSR**.

$$FSR = \nu_{q+1} - \nu_q. \tag{2.7}$$

Another key parameter in a Fabry-Perot interferometer is the FWHM of the transmission bandwidth W, which, if R $\approx$ 1 can be approximated to $\approx 4/\sqrt{F} \approx 2(1-R)$. Thanks to this last parameter it is possible to calculate the FWHM $\delta\nu$ with the proportion $\delta\nu/\Delta\nu = W/2\pi$ which is :

$$\delta\nu \approx \frac{1-R}{\pi}\Delta\nu \tag{2.8}$$

in particular the ratio $\Delta\nu/\delta\nu$ is called *finesse* of the Fabry-Perot. [36]
This particular scanning Fabry-Perot interferometer uses an optical cavity formed by two spherical mirrors with the same radius of curvature disposed in a confocal configuration which simplifies the alignment of the cavity.

Given the instrument FSR = 1,5 GHz, we measured an average bandwidth of 63 MHz FWHM with a standard deviation of 1.1 MHz over 60 measures taken in a span of 2 hours.

The bandwidth was calculated by measuring the time distance between two consecutive peaks transmitted by the Fabry-Perot interferometer and, by measuring the bandwidth of these peaks, then exploiting the proportion $\frac{\delta\nu}{FSR} = \frac{\delta t}{T}$. In Fig. 2.22 it is shown the typical oscilloscope trace showing the SLM operation of the laser (only one pulse present in a complete scanning Fabry-Perot FSR). The detail of the spectrum as measured by the instrument is shown in Fig.

2.23(a). Please notice that the spectrum appears as it is "sampled" at the period corresponding to the pulse period of the 1 kHz oscillator. In Fig. 2.23(b) it is shown the gaussian fit of the spectrum.

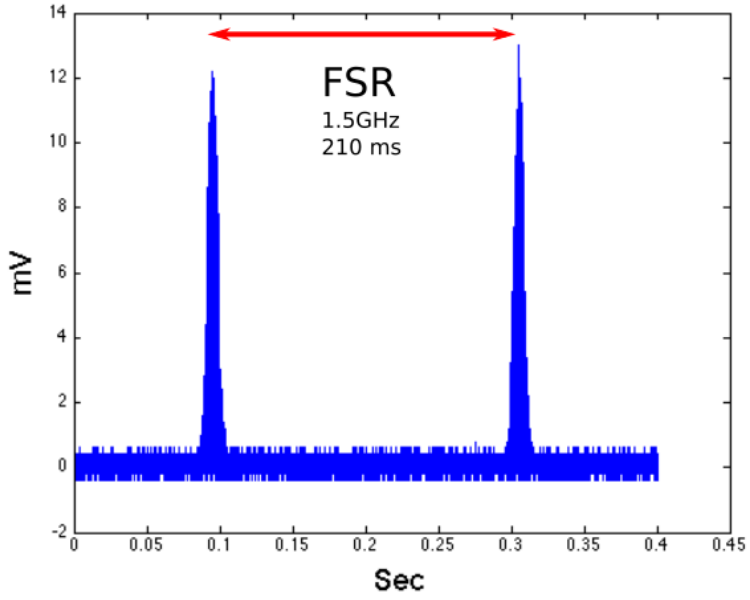

Figure 2.22: Oscilloscope trace of the scanning Fabry-Perot, the resolution of the measure was of 1 point every 200 ns for a total number of points of 2 million for every scan

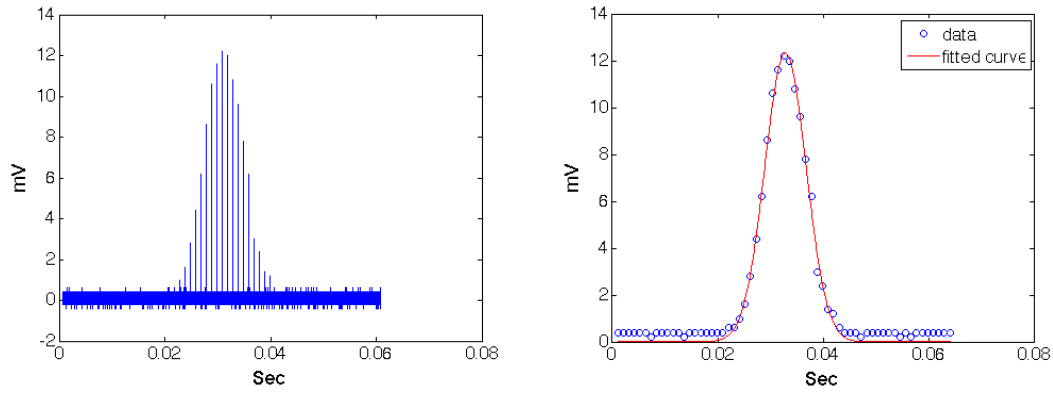

(a) (b)

Figure 2.23: Zoom over the first peak of the Fabry Perot scan (a) and gaussian fit of the envelope of the first peak (b). The gaussian fit was needed to accurately measure the FWHM and, therefore knowing the actual bandwidth of the pulses

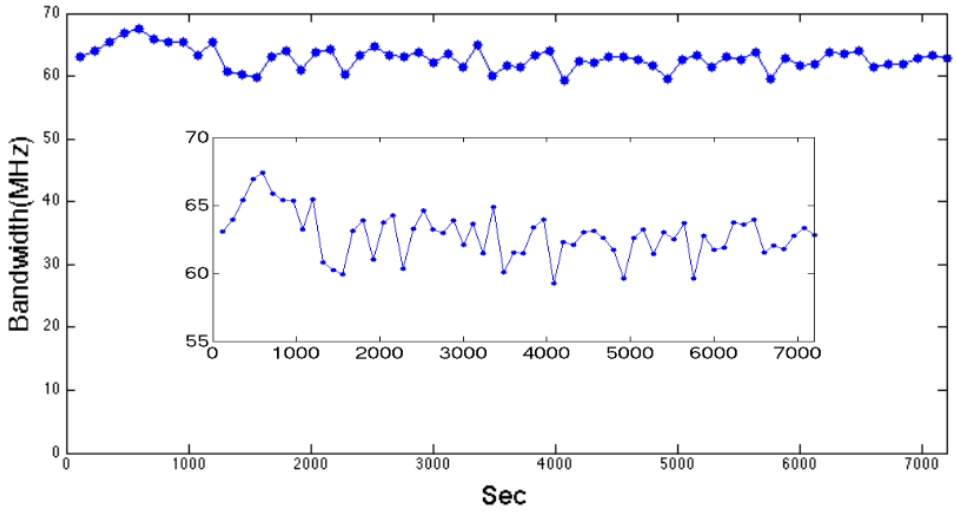

Figure 2.24: Series of measurements of the bandwidth taken in a span of 2 hours

Another information of the scanning of the Fabry-Perot was the absolute frequency stability of the laser which could be calculated as the displacement of the position of the first pulse. In order to calculate the stability of the frequency also the distance between the peaks was monitored and it was found to have a standard deviation of about 1% of its average value.

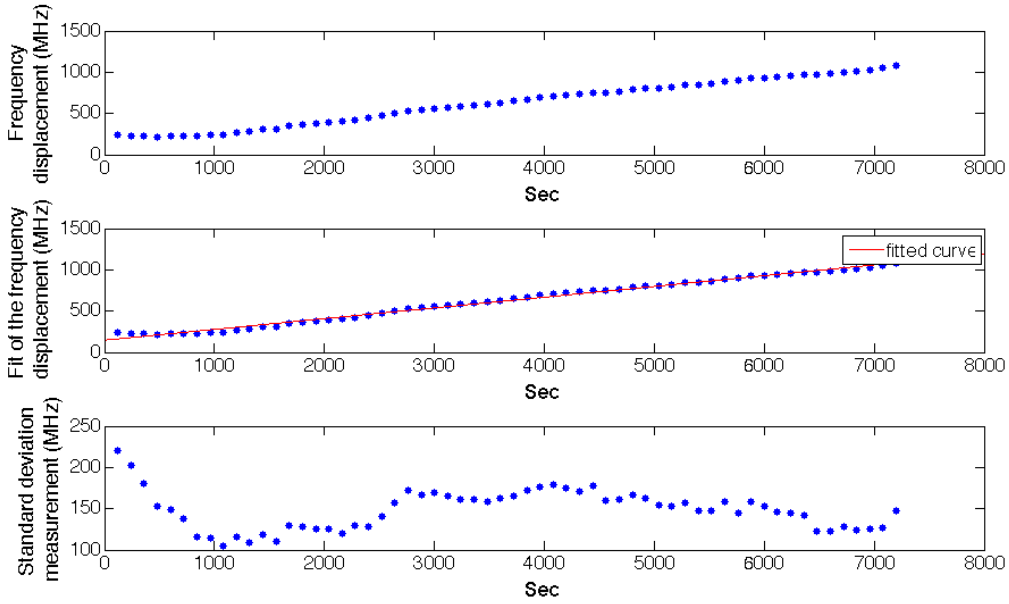

Figure 2.25: First peak pulse position (top), fit of the data (center), position deviation without the slope (bottom)

In Fig. 2.25 it is shown that the position of the first peak of the trace is changing almost linearly in time. The growth-rate is compatible with the room temperature growth. By ignoring the slope it is possible to calculate the standard deviation of the center of the peak and thus the absolute stability of the losing frequency. It was found a standard deviation of 23 MHz.

By assuming an average pulse duration of 13 ns and an average bandwidth of 63 MHz the time-bandwidth product was $\approx$ 0,8 fairly close to the Fourier limit for a gaussianly shaped pulse.

2.11 Nonlinear optics experiments

2.11.1 Stimulated Raman Scattering

The complex MOPA laser system I described in the previous sections had the following performance:

Pulse duration: 13 ns

Pulse energy: 3.2 mJ

Pulse peak power 250 kW

Pulse repetition rate: s.shot – 100 Hz

Output wavelength: 1064 nm

Optical bandwidth: 63 MHz (SLM)

Beam quality: $M_x^2 \times M_y^2 < 1.1$

Table-top footprint: ($\sim$1 m^2)

In order to match the requirements of the HSRL application (pulse energy 100 mJ), a further high energy amplification stage was required. I did not take part to the experiments related to this final amplification stage that was part of the PhD work of a colleague and are not described in this work. Nevertheless, the peculiar characteristics of this laser system, namely the high peak power available with excellent spatial and spectral beam quality are very interesting features for nonlinear frequency conversion experiments. Therefore, we took advantage of the availability in the Lab of a suitable sample of $SrWO_4$ to perform Stimulated Raman Scattering (SRS) experiments pumping with our nanosecond high spectral purity MOPA. The main

characteristics of $SrWO_4$ crystal relevant to SRS experiments are reported in Table 2.4.

Crystal family	Tungstates
Hardness	4 Mohs
Thermal conductivity	3 $Wm^{-1}K^{-1}$
Refractive index	1.87 at 1 μm
Sample dimensions	$4 \times 4 \times 30$ (length) mm^3
Dephasing time T_r	3.9 ps
g_r for pumping at 1064 nm	5 cm/GW (c-axis) 4 cm/GW (a-axis)
g_r for pumping at 532 nm	16 cm/GW
Raman shift	921 cm^{-1}

Table 2.4: Main physical and geometrical properties of the $SrWO_4$ sample used in the experiments

SRS is a third-order nonlinear effect corresponding to an inelastic scattering process involving the interaction of an incident photon (the pump photon at 1064 nm in our case) with a molecule, or the lattice of a crystalline medium. Depending on initial conditions (i.e. whether the molecule is in ground or excited state), the pump can transfer energy to the Raman medium, which in turn releases a red shifted beam (referred to as Stokes line), or extract energy from the already excited molecules, resulting in a blue shifted scattered light (called the anti-Stokes line).

It is worth noting that the anti-Stokes lines are typically much weaker than Stokes counterparts, since they rely on starting population in the excited state, whose value is predicted by the Boltzmann distribution at thermal equilibrium. Given the vibration nature of the Raman effect excitation, in solid-state materials, the energy absorbed or released by the materials is of the rough order of several hundred-few thousand of cm^{-1}, resulting in typical wavelength shift of 50 - 150 nm for a pump photon at 1 μm.

It is possible to identify a characteristic material response time T_r, after which it is reasonable to assume the interaction to be over. T_r is referred to as dephasing time which varies from material to material, but is typically of the order of few ps up to tens of ps in solid state

materials and it is found to be proportional to the inverse of the linewidth associated with the Raman transition, which is consequently typically in the rang 10-100 GHz. Given the material parameters reported in Table 2.4 and the characteristics of our pump laser, we fully exploited a steady state SRS regime, since our pulse duration was way longer than the dephasing time of $SrWO_4$.

Limiting the discussion of SRS to the situation in which a single Raman transition (i.e. first Stokes) experiences enough gain to be observed, at the same time applying a plane-wave approximation and neglecting pump depletion, the growth of the Stokes beam power P_{st} can be written as:

$$P_{st}(L) = P_{st}(0)e^{g_r I_p L} = P_{st}(0)e^{G} \tag{2.9}$$

Where g_r is the wavelength-dependent Raman gain of the material usually measured in cm/GW, L is the length of the Raman medium (if matched to the nonlinear interaction length, as usually occurs) and I_p is the incident pump intensity. In practical situations, when a travelling-wave SRS generation is targeted, in order to amplify the spontaneous quantum noise at the 1^{st} Stokes Raman-shifted wavelength, a net small-signal gain $G \sim 25$ must be provided. This permits to make an estimation of the required pump intensity to reach the Raman signal detection threshold, once is given the crystal length and the material Raman gain g_r. A significant reduction in SRS threshold intensity can be obtained if a cavity is employed in stead of a single-pass travelling-wave geometry. Considering a Raman oscillator pumped by pulses with duration τ, much longer than the round-trip time $2nl/c$, the oscillation threshold is reached when

$$\frac{P_N}{P_0} = \left[R_{OC}e^{-2\alpha L}e^{g_r I_{th}^{OSC} L}\right]^N \sim e^G \tag{2.10}$$

where P_N is the Raman pulse power after the maximum number of round trips $N = c\tau/2nl$, during which the pump provides the Raman amplification action, P_0 is the initial noise power at the Raman wavelength, R_{OC} is the output coupler reflectivity, and α is the passive loss per unit length due to scattering and other possible source of passive losses in the crystal. Therefore, one can relate the thresholds in a single pass, and for the oscillator,

$$I_{OSC} = \left(\frac{t_r}{\tau_p} + \frac{ln(R_{OC}) + 2\alpha L}{g_r L}\right) I_{SP} \tag{2.11}$$

The term in the brackets represents the reduction factor of the Raman oscillation threshold

with respect to a single-pass traveling-wave setup. It can readily exceed one order of magnitude, but even an uncoated monolithic crystal resonator can provide significant threshold reduction, allowing for safe SRS below the damage threshold for a given pulse duration.
Considering Eq. 2.9 and the material parameters of the $SrWO_4$ crystal at our disposal, we could estimate an incident pump threshold intensity for a single-pass travelling-wave Raman generation of $I_{th,1064nm} \approx 1.7$ GW/cm^2, $I_{th,532nm} \approx 0.5$ GW/cm^2. Considering the relatively long pump pulse duration (exceeding 10 ns), these incident intensity values could be already close to typical 1 GW/cm^2 material damage threshold. Even pumping at 532 nm, which clearly is very advantageous with respect to 1064 nm owing to the more than tripled value of the material Raman gain, the expected threshold is too high to permit efficient conversion, which requires typically above-threshold factor of about 2-3 before the onset of higher order Stokes limit the conversion efficiency of the 1^{st} Stokes. However, if one considers the threshold reduction factor in Eq. 2.11, even a low-finesse resonator constituted by the uncoated plane parallel facets of the crystal acting as two plane mirrors, can already yield a significant reduction in the expected threshold. Given $SrWO_4$ refractive index (see Table 2.4) the uncoated facets Fresnel reflectivity is R $\approx$ 9%. If one makes the reasonable assumption that distributed internal losses can be neglected, pumping the 30-mm-long $SrWO_4$ crystal with the 13-ns-long pulses (resulting in the factor N $\approx$ 30), the threshold reduction factor

$$I_{th}^{(OSC)} / I_{th}^{(SP)} \approx 0,2 \tag{2.12}$$

This may be not enough to guarantee safe operation in case of pumping at 1064 nm, but turns out in an expected threshold pump intensity of about 100 MW/cm^2 pumping with the second harmonic of the 1064 nm MOPA pulses. For this reason, once we verified that the parallelism of the $SrWO_4$ crystal facets was good enough to permit the low-finesse resonator behavior, we decided to setup a Raman generation experiment pumping at 532 nm.

2.11.2 Experimental setup and Raman conversion results

The experimental setup is shown in Fig. 2.27. In order to protect the MOPA laser from dangerous back-reflections we inserted a Faraday isolator between the final amplification stage and the SHG module. An HWP was used to properly adjust pump beam polarization for the SHG

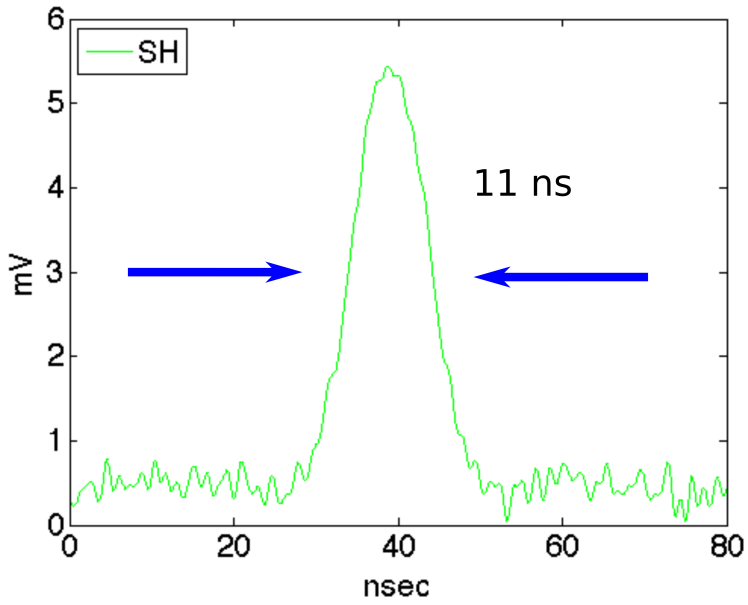

Figure 2.26: Oscilloscope trace of the Second Harmonic pulses at 532 nm

in a $3 \times 3 \times 5$ mm^3 type-II KTP crystal. After the Faraday rotator the maximum available pulse energy was about 2,7 mJ. The telescope formed by spherical lenses L12-L13 yelded a minimum beam waist in the KTP crystal of $w_e \sim 200$ μm resulting in a maximum on-axis peak intensity of about 300 MW/cm^2. In this conditions, we measured a SH conversion efficiency of about 56% with a pulse energy of 1,4 mJ at 532 nm. The oscilloscope trace of the SH pulses is shown in Fig. 2.26. The pulse duration was bout 11 ns.

Lens L14 (see Fig. 2.27) was used to re-image the 532 nm beam in the $SrWO_4$ crystal with a beam radius of 150 μm yielding a maximum on-axis pump peak intensity of about 360 MW/cm^2 in the Raman crystal.

Carefully aligning the Raman crystal with respect to the pump beam readily produced SRS at 559 nm with a pump energy threshold as low as 0,4 mJ. The corresponding on-axis pump intensity threshold is about 100 MW/cm^2, as shown in 2.29, which is in fair agreement with the prediction of Eq. 2.11.

M8, M12	Dielectric mirror HR 45° at 1064
M9	Dielectric mirror HR 0° at 1064
w_d	0,5 mm
L12	f=150 mm broadband AR coated in the near infrared
L13	f=75 mm broadband AR coated in the near infrared
w_e	200 μm
KTP	$3 \times 3 \times 5$ mm^3 AR coated at 532 nm and 1064 nm
M10	Dichroic mirror, HR/HT at 1064/808 nm at 45°
L14	f=75 mm AR coated at 532 nm
w_f	150 μm
M13, M14, M15	metallic mirror
L13	f=-50 mm broadband AR coated in the visible

Table 2.5: List of the acronyms and distances in Fig. 2.27

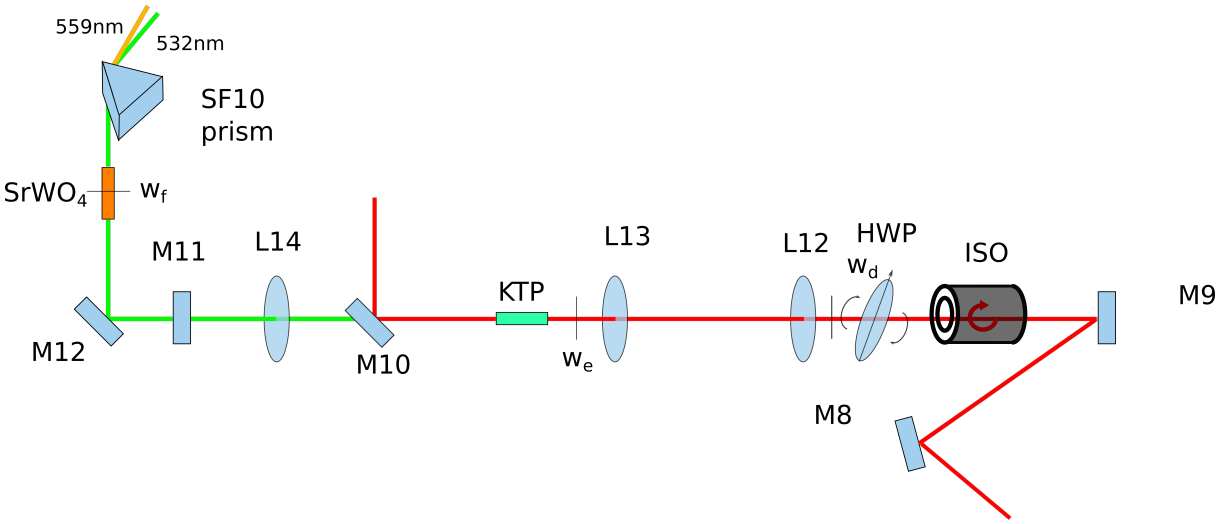

Figure 2.27: Setup for the SRS experiments

The SH and the Raman radiation were separated by a SF10 prism. It is worth noticing that even at the highest pump power no 2^{nd} Stokes was measured. Nevertheless, by observing the conversion curve of Fig. 2.29 it can be expected the onset of the 2^{nd} Stokes to have a role in

the slight drop of conversion slope efficiency close to the maximum incident pump energy. The output energy measured behind the exit face is shown in Fig. 2.29. The external slope efficiency amounts to 21%. Also taking into account the measured Raman output from the input face, the internal slope efficiency is 31%.

2.11.3 Spectral and spatial beam quality characterization

The oscilloscope trace of the Raman shifted pulses is shown in 2.28. The 3,3 ns pulse duration corresponds to a compression factor of about 3 with respect to the pump that can mainly be attributed to the small "above threshold" factor we operated the Raman converter. The pulse reduction contributed to maintain a significant pulse peak power at 559 nm: the maximum pulse energy obtained was 0,18 mJ, yielding a peak power of about 60 kW for the Raman shifted pulses.

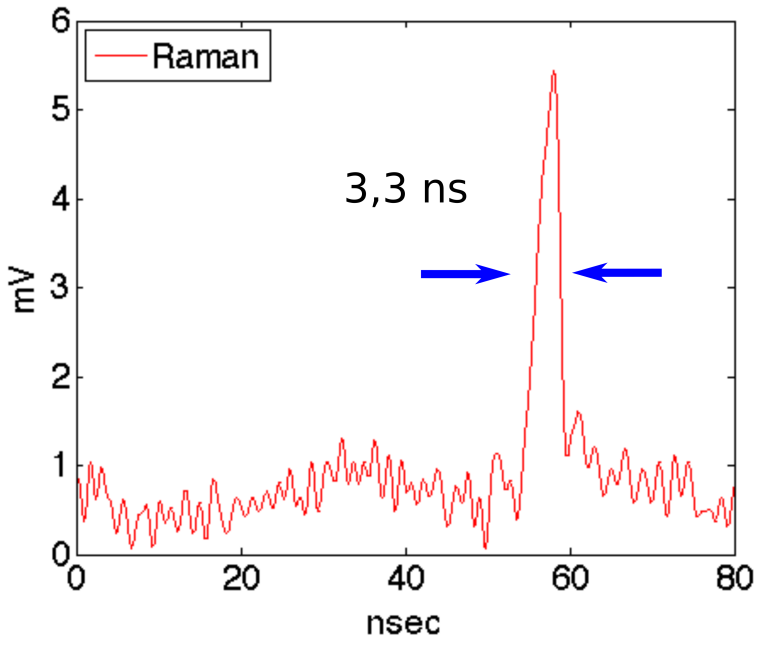

Figure 2.28: Oscilloscope trace of the generated Raman pulses

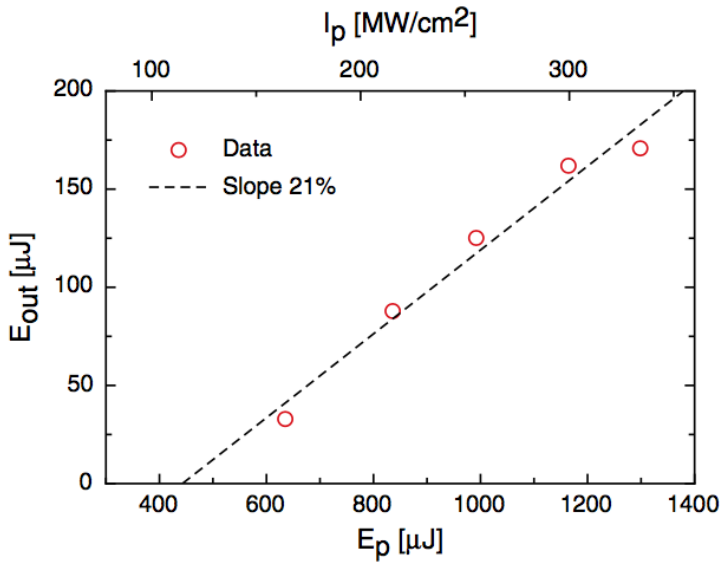

Figure 2.29: Raman output energy as a funcition of pump energy and pump on axis peak intensity

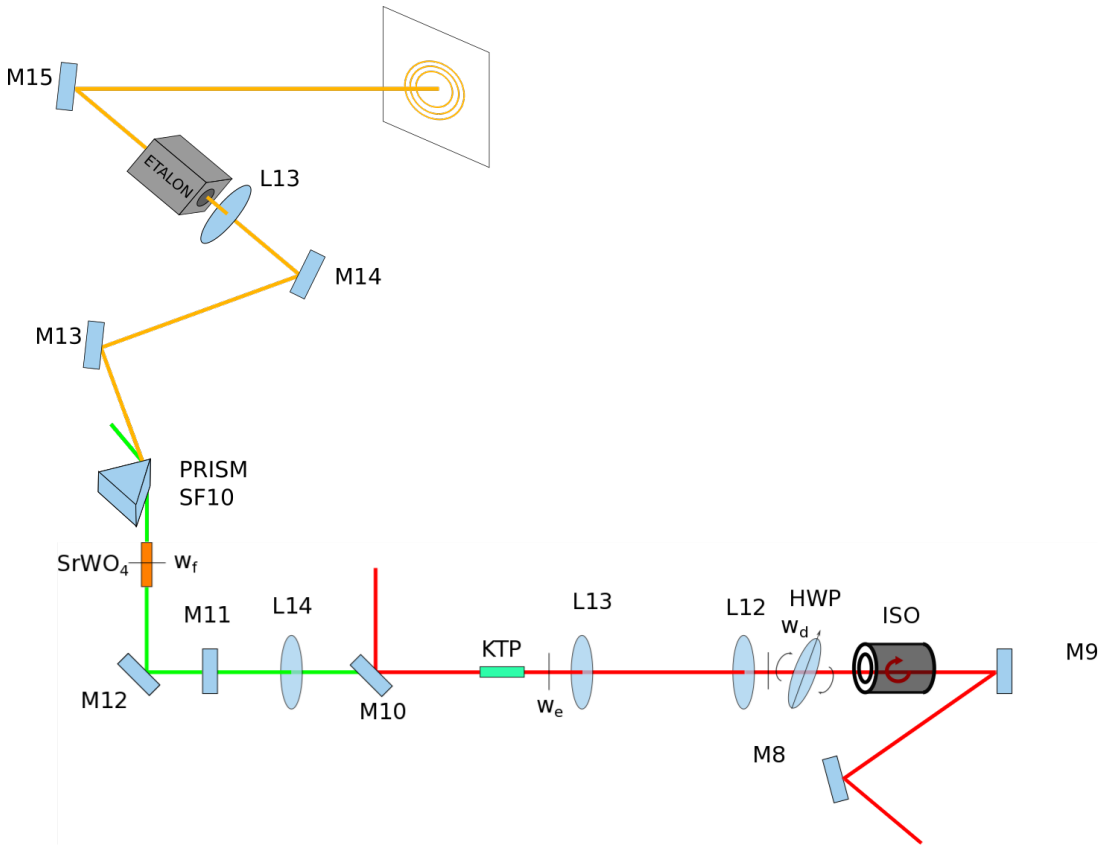

Figure 2.30: Setup for the analysis of the spectrum of the Raman pulses

Since the Fabry-Perot scan interferometer used for the characterization of the MOPA laser at 1064 nm was not suitable for investigation of spectral properties of the pulses in the visible, in order to investigate the longitudinal mode content of the pump at 532 nm and the Raman generated pulses, we employed a Quanta-Ray FPA-1 etalon specified with a finesse of about 10 and a FSR = 7.5 GHz. The SLM operation of the pump laser beam at 532 nm can be appreciated by the ring pattern produced by the Etalon as it is shown in Fig. 2.31.

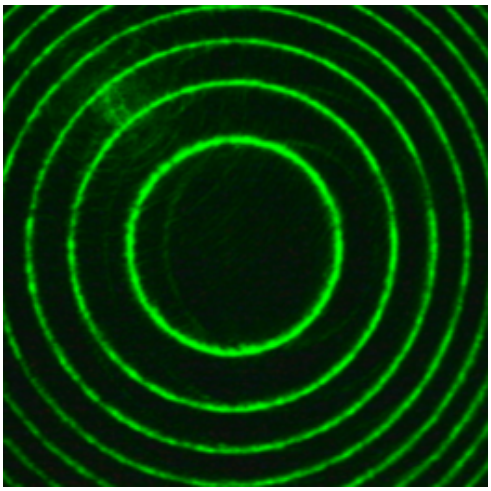

Figure 2.31: SH interference pattern

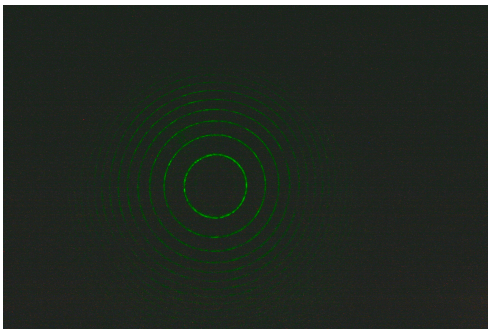

Figure 2.32: Single Mode

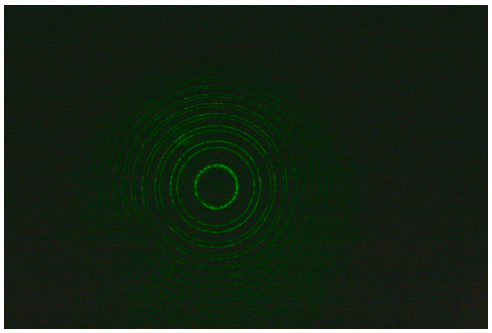

Figure 2.33: Multimodal

Figure 2.34: About 15% of the generated Raman shifted pulses resulted SLM

The same Etalon was used to characterize the longitudinal mode content of the Raman shifted pulses, with the setup shown in Fig. 2.30.

In Fig. 2.32 we report the ring pattern recorded in case of SLM Raman shifted laser pulses at 559 nm, whereas in Fig. 2.33 it is shown the ring pattern recorded in the presence of two

longitudinal modes. Notwithstanding the small feedback from the end facets, corresponding to a low finesse resonator, the cavity is clearly shaping the spectrum. At full pump energy, about 3 times above the threshold, oscillation occurs most often with 2 – 3 longitudinal modes whose spacing (inferred by the period of the ring pattern and etalon thickness) does correspond to the crystal length.

Previous results [37] showed that SRS pumped by a SLM laser exhibits a spectrum whose bandwidth is defined only by the finite dephasing time of the phonons. It is however possible, just like in [38] to obtain a SLM Raman generation if the pump energy is decreased close to SRS threshold. In our case when we get closer to the treshold (about 2 times above threshold) we noticed an increase in the occurrence of SLM pulses, but only for 20% of the times, while 60% were composed by only 2 longitudinal modes. Closer to threshold it was impossible to analyze the rate of SLM pulses because the low Raman power produced rings with too low intensity for our camera. It is believed however that the tendency is, like in [38], to obtain more frequent SLM emission.

In order to measure the spatial beam quality of the Raman radiation the beam was collimated with a 300 mm lens and then focused with a shorter 50 mm lens. The CCD camera was centered in the focus and translated in a span of 40 mm. As shown in Fig. 2.35, the Raman exhibited a fairly good beam quality ($M_x^2 \times M_y^2$=1,3×1,15) which is similar to the pump.

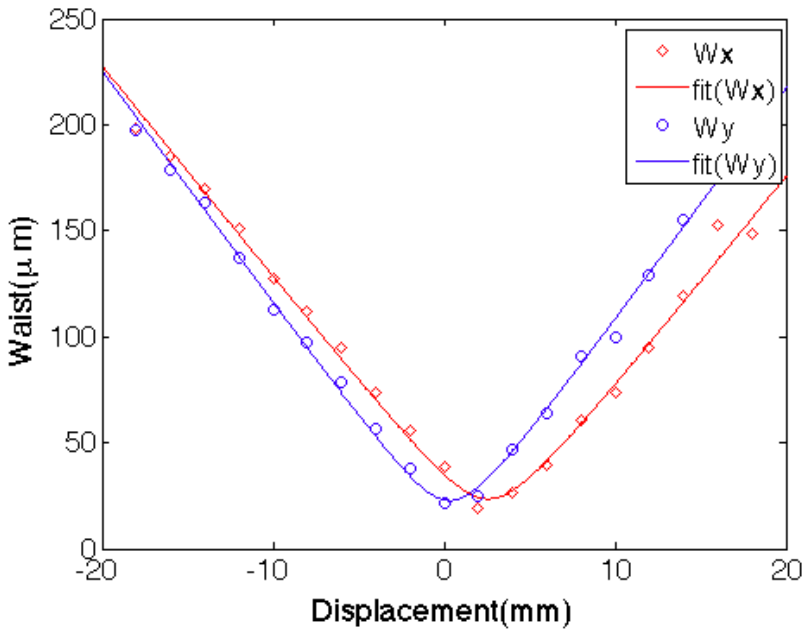

Figure 2.35: $M_x^2 = 1,3$ and $M_y^2 = 1,15$

A reverse calculation from the magnification telescope and the waist diameter in the focus showed resulted in a Raman beam waist $\approx$ 120 μm in the $SrWO_4$ crystal, which is $\sim$ 20% smaller than the pump beam waist, due to the nonlinear interaction. But it is significantly larger with respect to the expected $w_R \sim w_P/3$ for the traveling-wave generation with a slight pump depletion. This result suggests that, again, a cavity effect is taking place and shaping the beam.

The absence of mirrors and the geometry of the crystal only allowed a plane-plane configuration, which reduced the optical and slope efficiency with respect to [37] [39]. In this configuration it was therefore harder to optimize the mode-matching between the pump and the cavity mode. If a better beam quality or an higher efficiency are required, it would be possible, at an expense of more complex setup with respect to the monolithic plane-plane resonator, to design a stable cavity with curved mirrors and optimized mode matching.

3. Nonlinear 2-μm MOPA laser system for THz generation

3.1 Introduction

In this Chapter I describe the research activity and the experimental results obtained during a 6-month visiting period I spent at KTH Royal Institute of Technology in Stockholm, Sweden, from February 2017 to July 2017, when I was hosted by the Laser Physics group of the Department of Applied Physics at the School of Engineering Sciences. During this visit I had the opportunity to take part in a research project aimed to build a tunable double-wavelength nanosecond excitation source, with pulse energies in the range of tens of mJ [40]. This rather complex laser system was intended to be a universal laboratory source for testing different THz platforms which were developed in parallel by other colleagues at KTH. In order to achieve higher power conversion efficiency in THz generation the tunable source was designed to operate in the spectral range around 2 μm. Moreover, this wavelength range opens the possibility to exploit a large variety of THz generating media, including semiconductor platforms, which was the target of the project. The architecture chosen for the 2-μm laser source was an Optical Parametric Oscillator (OPO) followed by an Optical Parametric Amplifier (OPA) both pumped at 1 μm, since this was the most practical solution for achieving the required pulse energies in the spectral range of interest. The tunable source employed as nonlinear crystals specially designed quasi-phase-matched (QPM) structures in Rb:$KTiOPO_4$ (**RKTP**) directly produced at KTH. The pump laser at 1 μm for the optical parametric source was a commercial InnoLas injection-seeded, SLM laser at 1064 nm with a maximum output energy of about 200 mJ and

was available for the experiments at the laser lab at KTH. In Section 3.4, preliminary to the description of the research activity I personally took part in, I will report for the shake of completeness and clarity the characterization of the pump laser system at 1 μm as it was carried out when the laser was delivered to the lab. In Section 3.5 I report some design consideration for the singly resonant OPO and I describe the architecture and the performance of the OPO we built. In Section 3.6 it is described the OPA and the related experimental measurements. In Appendix B I give a brief overview on THz generation and applications of THz sources.

3.2 Basics of nonlinear optics and DFG

Nonlinear optics is the branch of optics that studies the interaction between optical radiation and matter when the incoming electric field E_{in} associated to the light beam is strong enough to excite a nonlinear response in the material polarization P. If the electric field has a sufficiently high intensity, indeed, the material susceptibility exhibits a non linear behavior:

$$\chi = \chi^{(1)} + \chi^{(2)}E(t) + \chi^{(3)}E^{(2)}(t)... \tag{3.1}$$

Where $\chi^{(2)}$ and $\chi^{(3)}$ are respectively the second and third order terms of the expansion. High enough field can be easily obtained with laser radiation and, in particular, if two laser beams at different angular frequencies ω_1, ω_2

$$E_{in} = E_1 cos(k_1 z - \omega_1 t + \phi_1) + E_2 cos(k_2 z - \omega_2 t + \phi_2) \tag{3.2}$$

enter a crystal whose second order nonlinear coefficient is sufficiently high, the generated radiation will be described by the following expression :

$$\begin{aligned} P^2 = \; & \frac{1}{2}E_1^2 cos(2(k_1 z - \omega_1 t + \phi_1)) + \\ & \frac{1}{2}E_2^2 cos(2(k_2 z - \omega_2 t + \phi_2)) + \\ & \frac{1}{2}(E_1^2 + E_2^2) + \\ & E_1 E_2 cos((k_1 + k_2)z - (\omega_1 + \omega_2)t + (\phi_1 + \phi_2)) + \\ & E_1 E_2 cos((k_1 - k_2)z - (\omega_1 - \omega_2)t + (\phi_1 - \phi_2)) \end{aligned} \tag{3.3}$$

The last term of equation 3.3 oscillating at angular frequency $(\omega_1 - \omega_2)$, specifically, represents the nonlinear effect called Difference Frequency Generation (**DFG**) since the frequency of the generated wave is the difference of the frequencies of the two incoming ones.
Second order nonlinear process are energy conservative, meaning that in DFG holds the relations

$$\hbar\omega_3 = \hbar\omega_1 - \hbar\omega_2 \tag{3.4}$$

where ω_3 is the frequency of the generated radiation and ω_1 and ω_2 are the two incoming ones, with $\omega_1 > \omega_2 > \omega_3$.
Since, usually, the refractive index of materials follow normal dispersion, the refractive index at different frequencies will have three different values i.e. $n_1 > n_2 > n_3$ creating a k-vector mismatch between the three waves given by

$$\Delta k = k_1 - k_2 - k_3. \tag{3.5}$$

In order to maximize the plane wave interaction the value of Δk needs to be as close as possible to zero. This condition is called **phase matching**.
In the DFG process in particular the relation between the three amplitude of the waves is

$$\frac{dA_3}{dz} = i\frac{\omega_3}{n_3 c} A_1 A_2^* d(z) e^{\Delta k z} \tag{3.6}$$

meaning that without phase matching the energy keeps flowing back and forth between the newly generated radiation and the incoming ones. A possible solution is to vary periodically the sign of the nonlinear coefficient: this technique is called **Quasi Phase Matching (QPM)**. QPM can be obtained by applying a periodic voltage over the length of a proper nonlinear crystal.

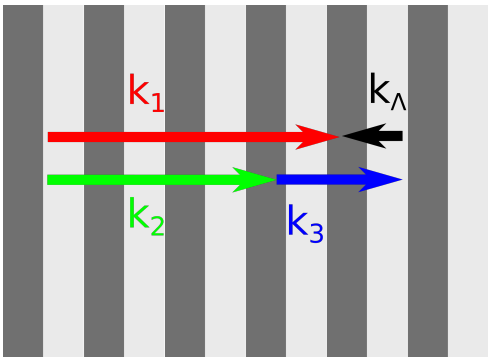

Figure 3.1: Quasi-Phase Matching scheme in a periodically poled crystal

The periodical poling will generate a new k-vector that will modify the interaction of the three waves and, if the period of the poling is properly chosen, the mismatch will be set to zero at a specific wavelength: $0 = k_1 - k_2 - k_3 - k_\Lambda$ where k_Λ is the k-vector of the periodicity of the nonlinear coefficient, i.e.

$$k_\Lambda = \frac{2\pi}{\Lambda} m \tag{3.7}$$

where

$$\Lambda = \frac{2\pi}{\Delta k} m \tag{3.8}$$

Meaning that the k-vector artificially created with the poling needs to compensate the phase mismatch [41].

3.3 Optical Parametric Oscillators

Radiation around 2 μm wavelength represents an interesting part of the optical spectrum because of its unique properties [42]. For example, 2 μm is a part of the so called "eye safe" spectrum ($\lambda >$ 1,4 μm) allowing a series of free space operations for this kind of sources such as LIDAR, gas sensing system and for space optical communications.
Another important characteristic of the 2 μm radiation is related to the absorption spectrum of water (see Fig. 3.2). There is indeed a peak in its absorption that allows systems operating at this particular wavelength to be excellent choices for biomedical treatment, since biological tissues well absorb this wavelength.

2 μm is also very interesting for applications in wind speed analysis which can be in turn very useful for weather forecasting.

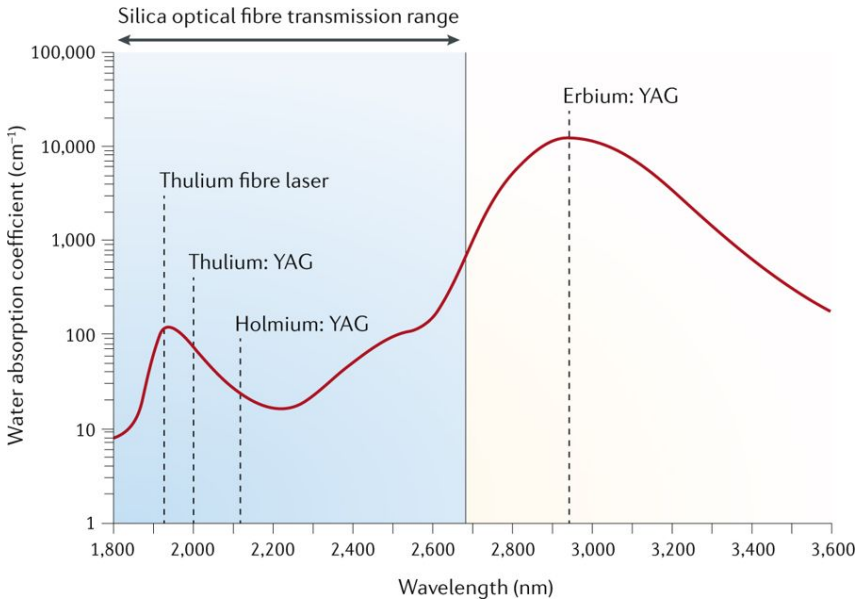

Figure 3.2: Optical spectrum of the absorption of water [43]

Because of its properties a series of possible sources for 2 μm generation have been investigated. In the field of solid state lasers particular interest has been put in Tm^{3+} and Ho^{3+} based systems. In particular Tm^{3+} lasers can be pumped by commercially available 800 nm diode lasers.

Another alternative, expecially for high energy applications, are the mid-infrared OPOs. OPO have been proposed first by Joseph Giordmaine and Bob Miller in 1965 [44]. Since their demonstration they have been used in many scientific research area thanks to their output wavelength flexibility, and, more recently, they have also been employed in industrial applications such as LIDAR or biomedical optics.

3.3.1 Nanosecond OPO

An OPO is a light source based on the DFG process [45][44]. As introduced in Section 3.2 a DFG process takes place when two beams properly phase matched enter a second order nonlinear medium, then a third beam, whose frequency is the difference of the two is generated. In an

OPO the DFG process takes place between a very intense pump beam and the quantum noise present in the nonlinear crystal and their relation is given by

$$\omega_{pump} = \omega_{signal} + \omega_{idler}. \tag{3.9}$$

The two waves generated inside an OPO are called **signal** and **idler**, with the former being the one at the higher frequency. Their frequencies need to sum up to the frequency of the pump, therefore if one of the two is changed, the other follows.

The generated traveling polarization wave needs to propagate at the same velocity of the two injected waves, meaning that the respective k-vectors of the three waves need to obey to the momentum matching condition

$$n_{pump}\omega_{pump} = n_{signal}\omega_{signal} + n_{idler}\omega_{idler}. \tag{3.10}$$

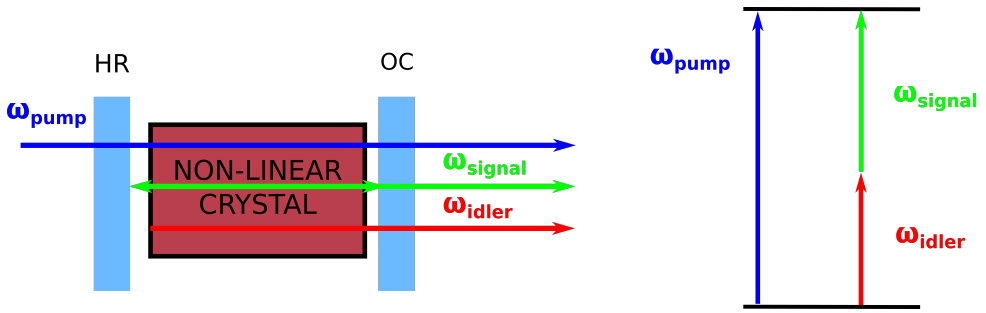

Figure 3.3: Singly resonant OPO general scheme. The incoming pump amplify the quantum noise at the frequency of the signal which is then amplified by the feedback effect of the cavity and the pump energy

Most OPO are *singly resonant*, meaning that the cavity mirrors are reflective (100% the pump mirror and usually 40-90% the output coupler) only for one of the two frequencies, being the signal or the idler. Another possible approach is to employ a *double resonant* design, i.e. an OPO where both the signal and the idler resonates inside the cavity.

The first CW pumped OPOs where built with a double resonant architecture, because they offer a lower threshold. Singly resonant OPOs however became more popular thanks to their higher output stability.

The main problems that limited the diffusion of OPOs in the past were the lack of high spatial beam quality pump sources and the low damage thresholds of nonlinear materials.

These two problems have been solved by the improvement of diode pumped solid-state lasers and by the development of new more resistant nonlinear materials such as BBO, LBO and KTP that allows high level of pump power as well as the possibility to adopt quasi-phase matching (for KTP).

If we consider an end-pumped linear OPO, it is possible to define the gain g per unit of length as [46]

$$g = \sqrt{\kappa I_p} \tag{3.11}$$

with I_p being the pump intensity and κ the coupling constant measured in W^{-1}

$$\kappa = \frac{8\pi^2 d_{eff}^2}{\lambda_s \lambda_i n_s n_i n_p \epsilon_0 c} \tag{3.12}$$

where d_{eff} is the nonlinear coefficient which depends on the type of conversion between pump, signal and idler and, of course, on the choice of the nonlinear material (for PPKTP at 1064 nm it is in the range of $\approx$ 5 - 10 pm/V).

The ideal single-pass power gain can be approximated by

$$G = \frac{1}{4} exp(2gl) \tag{3.13}$$

where l is the length of the crystal. However, the gain in the equation 3.13 does not take into account any possible mismatch Δk in the wavenumbers of the three waves interaction. When such a mismatch occurs the actual gain coefficient can be expressed by the equation

$$g_{eff} = \sqrt{g^2 - \left(\frac{1}{2}\Delta k\right)^2} \tag{3.14}$$

If we consider the case of a RKTP crystal pumped at 1 μm and generating around 2 μm, from [47], the typical value of damage fluence is in the order of 10 J/cm^2, which corresponds to the remarkably high damage intensity of 1 GW/cm^2 for 10-ns pulses. The typical values of d_{eff} for PPKTP are $d_{eff} \sim 8$ pm/V, which results in a coupling parameter of eq. 3.12, $k \sim 8 \cdot 10^{-8}$ W^{-1} for a pump at 1064 nm and a signal/idler around degeneracy at 2.1 μm. If one considers to work far from the damage threshold, for example at 30% of the maximum theoretical allowed incident intensity, the available gain per unit length of eq. 3.11 can be as high as $g \sim 5$ cm^{-1} in condition of perfect phase matching. Clearly, in order to maintain such high gain per unit

of length, the phase matching condition must be satisfied precisely enough to maintain the phase mismatch $\Delta k/2 \ll g$ (see eq. 3.14). At 1 μm, given a refractive index $n \simeq 1,7$, this means that the propagation constants have to be phase-matched to better than 10^{-5}/cm.

According to the model developed by Byer et al. [48], an estimation of the threshold intensity for the nanosecond pumped OPO can be obtained by

$$I_{th} = \frac{1.12}{\kappa g_s l_{eff}^2}\Big(\frac{L}{t_p c} ln\frac{P_s}{P_n} + 2\alpha l + ln\frac{1}{\sqrt{R_{OC}}} + ln2\Big)^2 \tag{3.15}$$

where,

- k can be calculated through eq. 3.12;
- g_s is the spatial mode coupling defining the overlap between the pump mode of radius w_p and the resonating signal mode (w_s) inside the nonlinear crystal and is given by

$$g_s = \frac{1}{1 + (w_s/w_p)^2}$$

- l_{eff} is the effective nonlinear gain length, that can be approximated with the nonlinear crystal length if walk-off can be neglected and the confocal parameter of the pump is larger than the nonlinear crystal length;
- $L/\tau_p c$ represents the number of OPO cavity roundtrips contained in a pump pulse duration (the shorter the cavity, the lower the threshold once the pump pulse duration is fixed!);
- $\ln(P_s/P_n)$ is usually assumed $\simeq 30$ and represent the logarithmic gain required to amplify spontaneous quantum noise to a detectable ("threshold") energy level;
- $2\alpha l$ are the length dependent nonlinear crystal losses;
- R_{OC} is the reflectivity of the output coupler.

3.4 Characterization of the InnoLas pump laser at KTH Laser Lab

The pump laser was an injection seeded, Q-Switched Nd:YAG commercial Innolas Spitlight diode pumped solid state nanosecond laser. The complete characterization of the laser can be found in [49].

In 2012, when the laser was delivered to KTH laser lab, the maximum average output power of the oscillator was $\approx$ 8,5 W at 100 Hz while the maximum available average power of the MOPA was $\approx$ 24 W corresponding to a maximum energy of 240 mJ as shown in Fig. 3.4. The stabilization of the laser in term of pulse duration and maximum output power needed one hour of stabilization time. In Fig. 3.5 it is presented the spectrum of the laser measured with an ANDO AQ-6315A optical spectrum analyzer. The central output wavelength was approximately 1064.12 nm, whereas the FWHM bandwidth was about 50 pm, close to the instrument resolution. The beam quality of the system was measured with the knife edge technique and resulted in an $M_x^2 \times M_y^2$=3,2$\times$3,3.

It is worth noticing that the actual power at our disposal for the pumping of the OPO was 15 W at 100 Hz and that the maximum power could be reached only after a 2 hour thermal stabilization of the system.

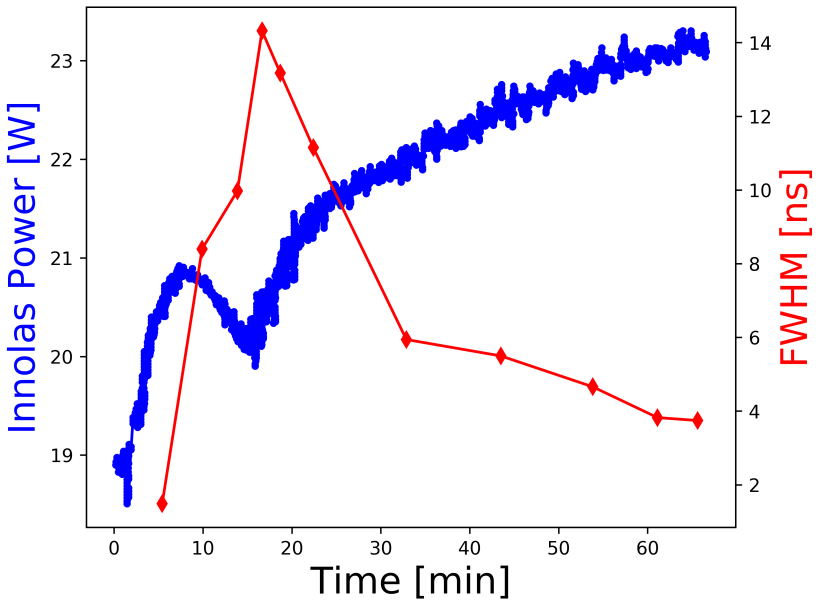

Figure 3.4: Pulse duration and average power from the Innolas pump laser from the "switching on" to the parameter stabilization

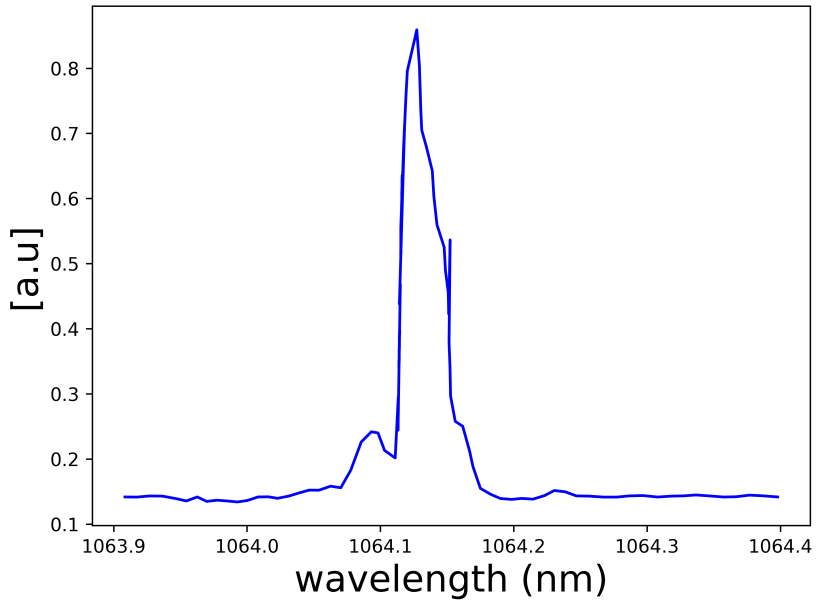

Figure 3.5: Spectrum of the pump laser [49] measured with an ANDO AQ-6315A optical spectrum analyzer

The power level was selectable with a half wavelength waveplate combined with a polar-

izer. The maximum attenuation given by this system was 90%, and, assuming a polarization extinction of 99% from the polarizer, it can be deduced that the pump beam had a polaritazion ratio of 9:1.

3.5 Design of a PPRKTP 2-μm OPO

Semiconductor materials have been successfully employed for the generation of Mid-infrared and Terahertz radiation [50][51] in particular a tunable THz wave with a peak power of 134 W was obtained by [52]. The main advantages in employing a 2 μm source instead of a more common 1 μm laser is represented by the lower losses in the semiconductor materials, meaning higher energy usable for the Terahertz conversion.

Down-conversion from the established 1 μm pump laser has been widely used for high energy generation in the far infrared [53] [54]. For these OPOs, KTP has often been used thanks to its high nonlinearity as well as its high damage threshold [55]. In this project we aimed at the development of an OPO based MOPA system whose signal and idler were tunable in the THz range.

The output coupler was a chirped VBG made by Optigrate inc., a mirror selective in frequency, a selectivity given by the periodicity of the refractive index inside the device. The wavelength reflected λ_B is given by the relation:

$$\lambda_B = 2n_e \Lambda cos(\theta) \tag{3.16}$$

Where Λ is the period of the grating, n_e is the average refractive index of the material and θ is the incidence angle, with $cos(\theta)$=1 for normal incidence.

From equation 3.16 it is clear that the reflected wavelength depends on the periodicity of the gratings. The particular VBG used in the experiment was a chirped VBG, i.e. a VBG whose periodicity of the Bragg grating changed linearly along its transverse dimension, as shown in Fig. 3.6(b).

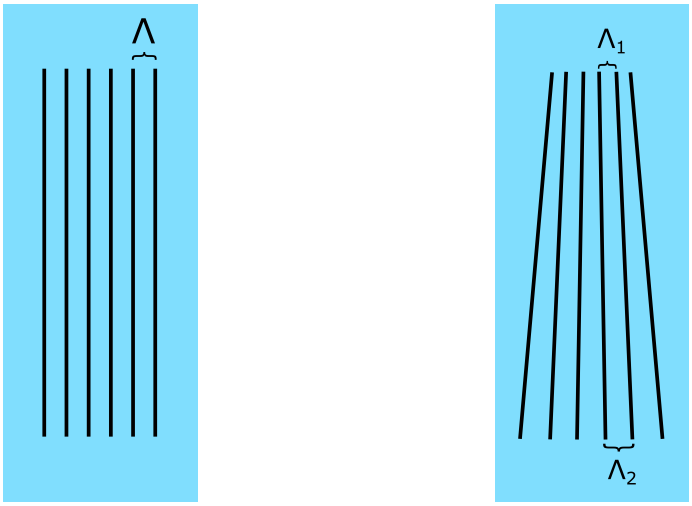

(a) (b)

Figure 3.6: VBG (a) and chirped VBG (b) schemes. In the chirped VBG the periodicity changes along the transversal length of the device changing the wavelength reflected from a minimum value of $\lambda_1 = 2n_e\Lambda_1$ to a maximum of $\lambda_2 = 2n_e\Lambda_2$ for normal incidence

The VBG used was fabricated by Optigrate and the grating had a dimension of $2.2 \times 19 \times 5$ mm^3 in the x-y-z coordinates. The wavelength reflected at the center of the VBG was $\sim$ 2130 nm and the chirp rate was 1,08 nm/mm meaning that the possible reflected wavelengths fell between 2120 and 2140 nm with a maximum reflectivity of 55%. The VBG was mounted on a translational stage in order to easily select the operating wavelength and it was thermally controlled by a Peltier cell.

The chirped VBG was the most sensitive component in terms of optical damage. It had a damage fluence of 5 J/cm^2 according to the datasheet. Since the chirp rate was 1,08 nm/mm the beam radius of the resonating radiation needed to be lower than $\approx$ 450-500 μm in order to exploit its full wavelength sensitivity. This limitations translated in a maximum pump pulse energy of 19 mJ. Since it was our priority to avoid any optical damage to the VBG we decided to operate at least 2 times below threshold.

The nonlinear material employed for the OPO architecture was a Rubidium doped Periodically Poled Potassium Titanyl Phosphate (**RPPKTP**).

KTP presents a series of advantages if compared to other nonlinear crystal such as a large nonlinear coefficient, a large angular bandwidth, small walk-off angle and broad temperature and spectral bandwidth.

Properties	**Values**
Nonlinear optical coefficient (pm/V)	d $\approx$ 3-16
Thermal conductivity	3 $Wm^{-1}K^{-1}$
Refractive index	1,71 at 1 μm 1,73 at 2 μm
Sample dimensions	$5 \times 7 \times 12$ (length) mm^3
Optical absorption	0,6% /cm at 1064 nm
Thermal expansion coefficient	10×10^{-6} $°C^{-1}$
Transmission range	0,35-4,5 μm
Hardness	5 Mohs

Table 3.1: Main physical and geometrical properties of the PPRKTP sample used in the experiments

Moreover RKTP can be relatively easily poled with electric poling techniques, thus allowing relatively high precision and a wide range of possible phase matching condition.

The PPRKTP employed was a $7 \times 5 \times 12$ mm^3 crystal periodically poled. Rubidium doping made the electric poling of the crystal easier thus allowing the fabrication of better quality samples [56]. The period of the poling was 38,85 μm with a duty cycle of 50% in order to convert the pump wavelength at 1064 nm to 2 μm. The end faces were AR coated for 1 and 2 μm and the PPRKTP was thermally controlled by a Peltier cell and it was kept at 55° to be insensitive to any room temperature fluctuation.

A preliminary estimation of the pump intensity and pump energy required to reach the threshold for the parametric generation can be done according to eq. 3.15. Assuming a $d_{eff} \approx 8$ pm/V, a signal and pump mode coupling coefficient of $\approx$ 0,5, corresponding to a perfect overlap and a resonator length of 5 cm, the threshold energy for a 12-mm-long PPRKTP resulted to be

in the order of ≈ 3 mJ for a pump beam radius w_p=0,5 mm.

Starting from a fixed pump beam radius on the VBG a series of simulations were performed by means of the free simulation software SNLO and different cavity architectures were analyzed. The simulations regarding the design and the validation of the experimental results were performed by other PhD students from KTH and Sun Yat-Sen University involved in the project.

The final design which guaranteed the highest output energy still remaining below damage threshold resulted in a concave plane cavity of ≈ 50 mm of length. The curved pump mirror of the OPO was a plane–concave mirror with a double coating on the curved surface which was HR for 2 μm and AR (92% of transmissivity) for 1 μm. The pump fluence inside the nonlinear medium was ≈ 2,5 J/cm^2 for a pump energy of ≈ 7 mJ. The waist radius of the signal+idler on the VBG was 480 μm and the fluence on it was 2,4 J/cm^2.

Another simulation was later performed by means of a numerical model briefly described in [40] to verify the experimental results and the fit of the data led to a d_{eff} of the active material employed of 7,6 pm/V which is similar to the expected value for PPKTP.

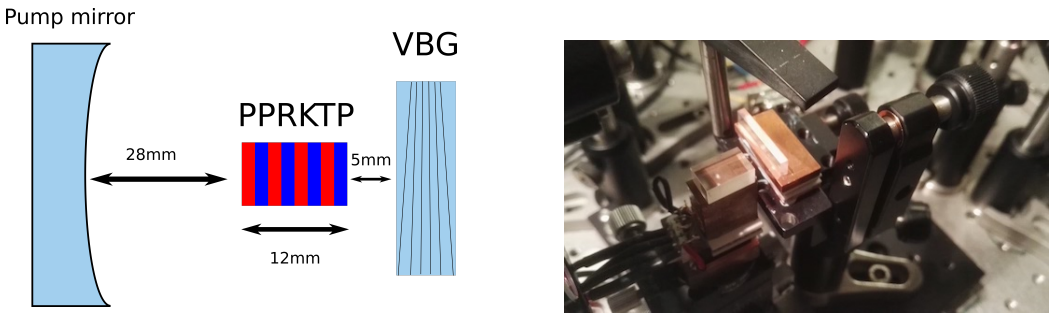

Figure 3.7: Architecture of the OPO: the pump mirror had a curvature radius of 150 mm and was HR coated for 2 μm and AR coated for 1 μm (a) and photo of the chirped VBG and the nonlinear crystal (b)

In order to maximize the spatial beam quality of the generated radiation, the pump beam ellipticity was corrected and its waist was reshaped in order to match the cavity mode.

This was possible with a combination of spherical and cylindrical telescopes. We estimated

a pump beam waist of 500 μm in the PP-RKTP crystal.

The VBG was translated orthogonally to the optical axis for a length of around 20 mm and the spectrum of the signal and the idler covered wavelengths from 2117 nm (signal) up to 2140 nm (idler) as shown in Fig. 3.8. The spectra of the various configurations were taken with a Jobin Yvon iHR330 diffraction grating monochromator and a PbSe photodetector. The groove density of the grating was 300/mm and it could provide an accuracy of 0,5 nm.

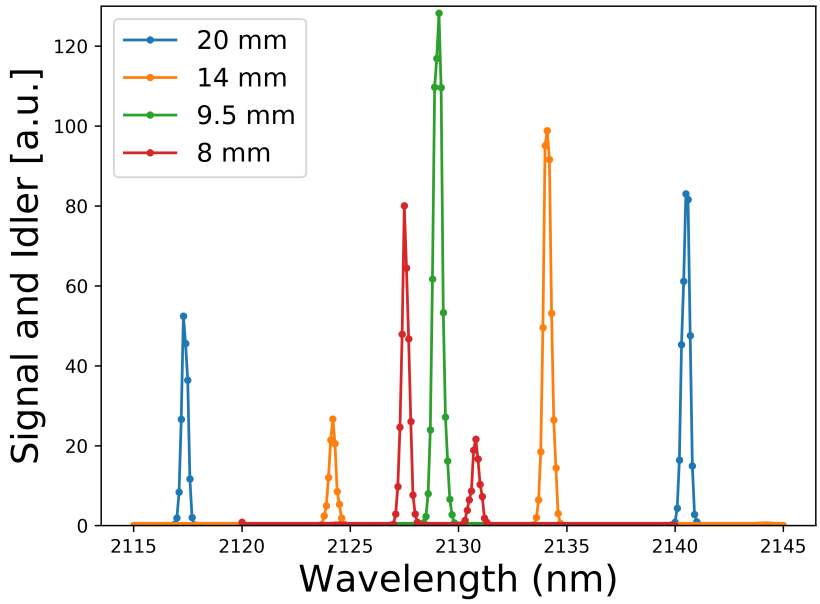

Figure 3.8: Output of the OPO with the VBG at different position

The input beam needed to be further filtered from the 1 μm pump in order to avoid any influence of the pump in the measurement. The fluctuation of the amplitude of the signal and the idler, especially for the wavelengths far from degeneracy, can be explained by a non-optimal alignment of the cavity for this particular configurations. The alignment could anyway be corrected and the output presented the same characteristic of spectral and spatial quality for any operating wavelength.

The maximum output power obtained from the OPO was 1,5 mJ for a pump energy of 7 mJ and a threshold of 4 mJ 3.10 (a). The rms was 1,4% with a conversion efficiency of $\sim$ 20%.

The duration of the pump pulse and OPO pulse were measured respectively by an InGaAs photodetector and a PEM (VIGO) detector and is shown in Fig. 3.9 .

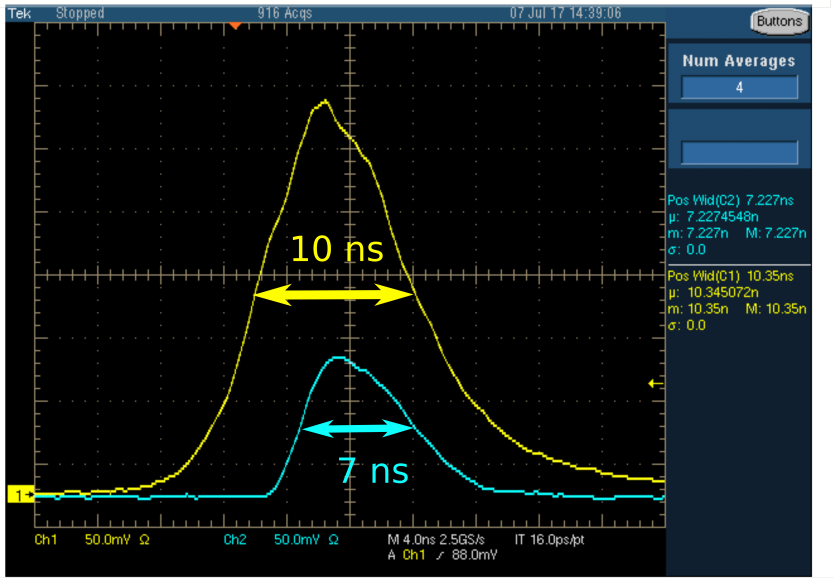

Figure 3.9: Oscilloscope trace of the pump laser with the OPO generated radiation

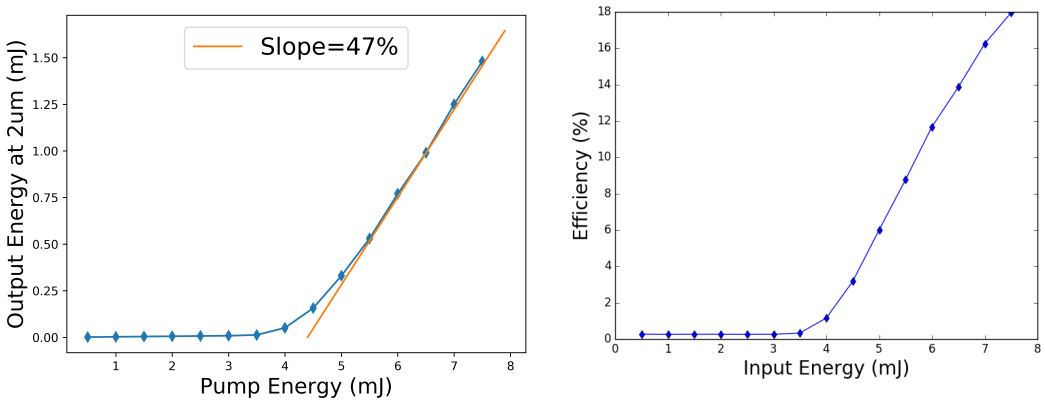

(a) (b)

Figure 3.10: Output energy of the signal and the idler combined versus the pump energy (a) and optical efficiency of the OPO (b)

In Fig. 3.10 it is shown the characterization of the output energy (signal + idler) as a function of the incident pump energy. The output energy of the seeder was dependent on the alignment of the cavity. In Fig. 3.11 (a) it is shown the pump beam profile whose non-perfectly

gaussian shape determined a similiar profile for the OPO (Fig. 3.11 (b)). It is however worth noticing that the seeder beam profile could be improved at the expenses of the output energy. It was indeed possible to obtain a better spatial quality for the seeder beam (Fig. 3.11 (c)) for a 20% drop in output energy.

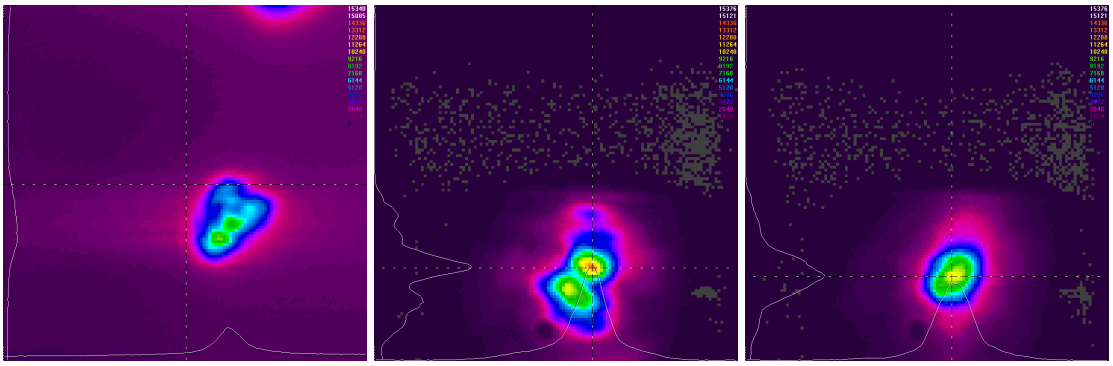

(a) (b) (c)

Figure 3.11: Beam profile of the Pump (a), the seeder optimized for maximum energy (b) and maximum beam quality (c)

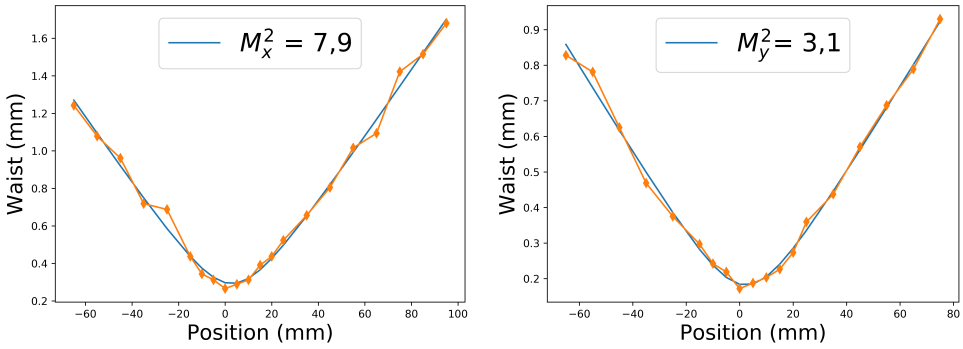

(a) (b)

Figure 3.12: Spatial beam quality for the x and y directions measured with the knife edge technique

In Fig. 3.12 it is shown the results of a beam quality measurement of the OPO output carried out when the OPO was aligned for maximum energy conversion. The measurement was carried out with the Pyrocam and resulted in a $M_x^2 \times M_y^2 = 7,9 \times 3,1$. Since our goal was

the optimization of the energy performance of the nonlinear MOPA, we decided to optimize OPO alignment for maximum conversion efficiency in subsequent experiments.

3.6 Optical Parametric Amplification stage: setup and results

The experimental setup of the OPO+OPA MOPA is shown in Fig. 3.13.

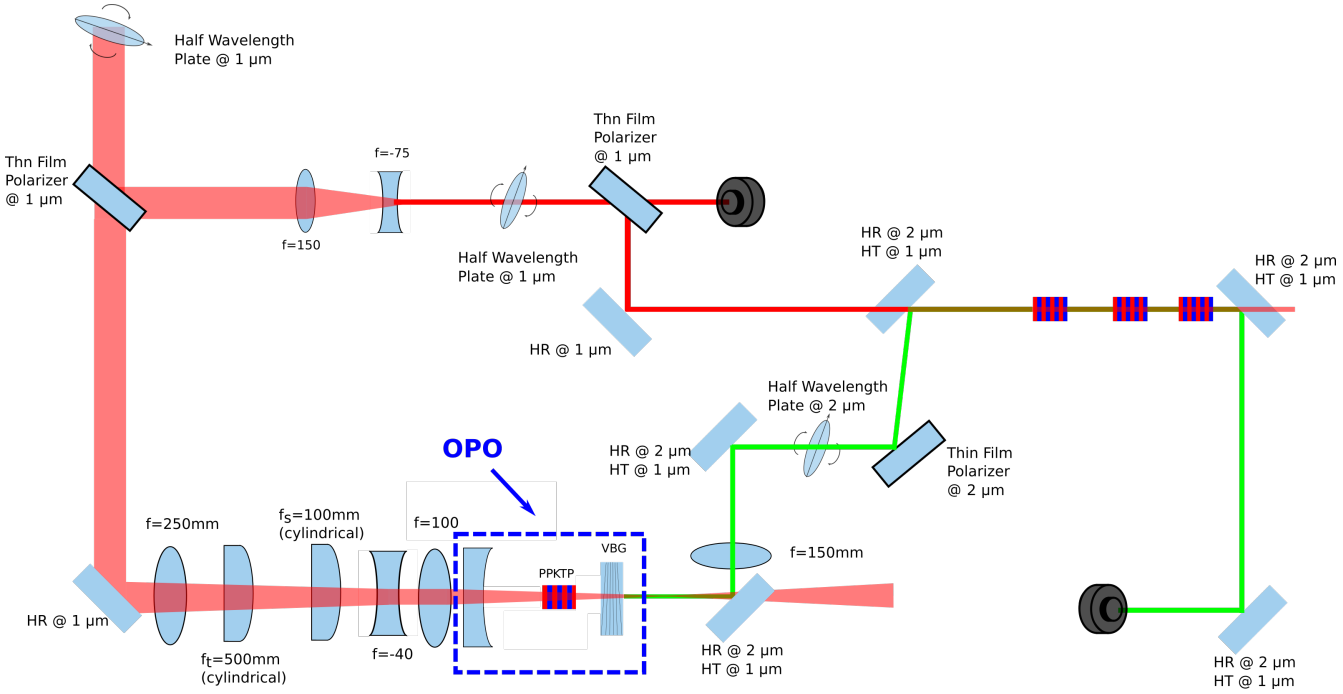

Figure 3.13: Setup of the Optical Parametric Amplifier

Signal and idler generated by the OPO were collimated by means of a 150 mm spherical lens and separated from the pump by three dichroic mirrors highly reflective for 2,1 μm and highly transmittant at 1 μm.

The OPO output and the residual pump were then superimposed and injected in the OPA crystals. The amount of pump and signal + idler were controlled by a combination of thin film polarizer and half wavelength waveplates at 1064 nm and 2,1 μm respectively.

In order to improve the mode matching between the pump and the 2 μm radiation the waist of the former was adjusted by a telescope.

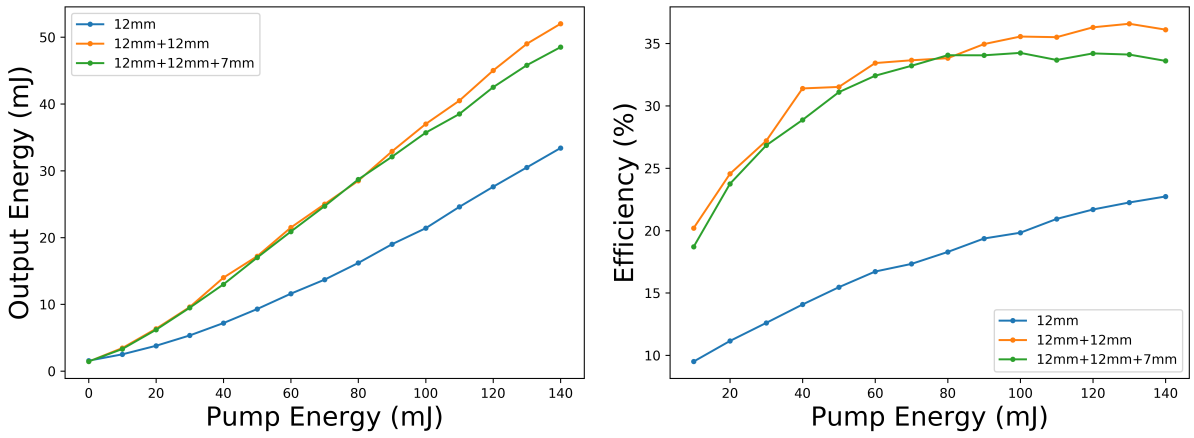

(a) (b)

Figure 3.14: Output energy after the amplifier with the three different configurations (a) and their respective efficiencies (b)

The measured output energy and conversion efficiency of the different OPA stages are given in Fig. 3.14. At the maximum pump energy of 140 mJ used in the amplifier and with a seed energy of $\sim$ 1,5 mJ, this corresponded to an incident fluence of 2,25 J/cm^2. It is well below the damage threshold of the crystals, which have been measured to be 10 J/cm^2 at 1 μm with nanosecond pulses [47], indicating further power scaling would still be possible. The number of crystals in the amplifier stage was varied, from one to three in total, and the energy output of each configuration was measured. The seed energy from the OPO was 1,5 mJ in each case.

For a single-amplifier crystal with a length of 12 mm, and pumping with 140 mJ, we were able to reach a maximum total energy output of 38,3 mJ. This corresponds to an OPA conversion efficiency of 26%. In this case, the OPA did not reach saturation yet. To drive the OPA into saturation and increase the extraction efficiency, a longer OPA crystal would be required. Therefore, we added a second 12 mm PPRKTP crystal to the OPA stage and re-measured the output. For two crystals (12 + 12 mm), we measured an improvement in the energy yield of OPA, with a maximum output energy of 52 mJ at 140 mJ pump energy, see Fig. 3.14.

This corresponded to the OPA power-extraction efficiency of 36%. In this case, the amplifier began to saturate at around 60 mJ of the input pump. Extending the OPA length further by adding one more 7-mm-long crystal did not improve the OPA efficiency. This configuration (12

+ 12 + 7 mm), actually showed lower performance than the two crystal amplifier. A maximum output energy of 48,5 mJ was reached in this case, with a corresponding conversion efficiency of 33,5%, limited by back-conversion. For this reason, we used the two-crystal amplifier for further measurements. The OPA gain as a function of the seed energy was measured at the pump energy of 60 mJ where the OPA just reached saturation (see Fig. 3.15).

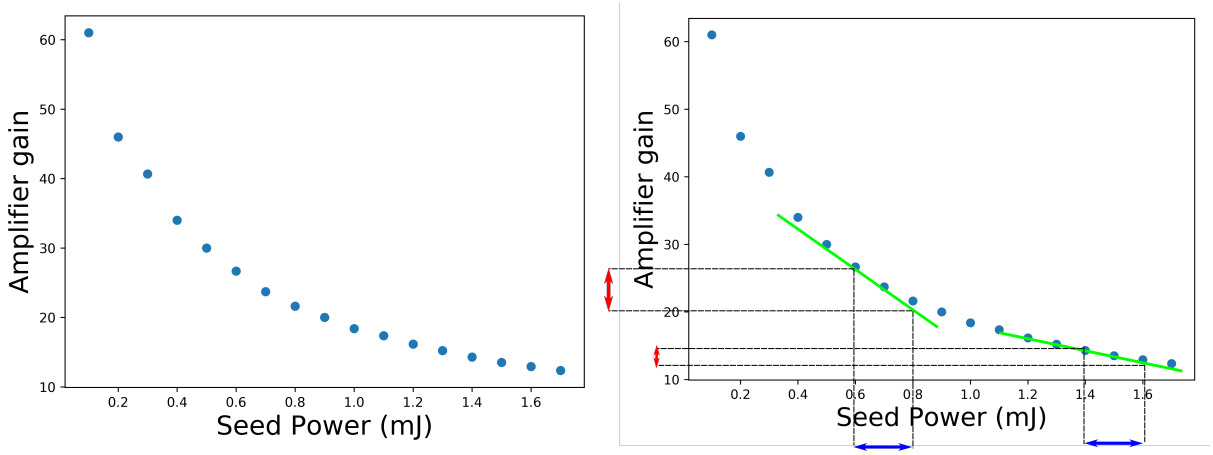

(a) (b)

Figure 3.15: Amplifier efficiency measured by varying the amount of energy of the OPO injected inside the amplifier while maintaining a fixed pump energy of 60 mJ.

The amplifier showed significant saturation for seed energies above 1 mJ. The linear slope of the output energy vs input seed energy for the seed below 0,5 mJ was 12,8%, meaning that OPO fluctuations of 1,4% rms would have been amplified to 18% rms after the amplifier. At the seed energies above 1 mJ, the slope decreased to 2,6%, reducing the output fluctuations to 3,6%. By increasing the pump energy to 140 mJ, the rms fluctuations of the OPA output approached that of the seed OPO. For this reason, we decided to use a seed energy of $\sim$ 1,5 mJ in the amplifier experiments. The output spectra of the amplifier was also measured (Fig. 3.16). The spectrum of the OPA stage was measured for increasing pump energies (40, 80 and 120 mJ). As it can be seen in the figure, the amplified signal and idler spectra showed no broadening or wavelength shift even for maximum pump energy and thus, the bandwidth was comparable to that of the OPO output. The OPO was singly resonant on the idler field, and therefore, the majority of the power was initially contained in the idler. This is also the reason why one sees

such a fast growth in the signal during amplification, since there was little signal power to begin with, therefore, a greater improvement was easily seen. After significant pumping (post 80 mJ), the amplifier began to become saturated leading to larger increase shown in Fig. 3.16. The saturation was evident from the measured conversion efficiencies in Fig. 3.14. At this point, the OPA behavior approached something more similar to difference frequency mixing (DFM), as opposed to DFG amplification, so more energy flew into the signal field [40].

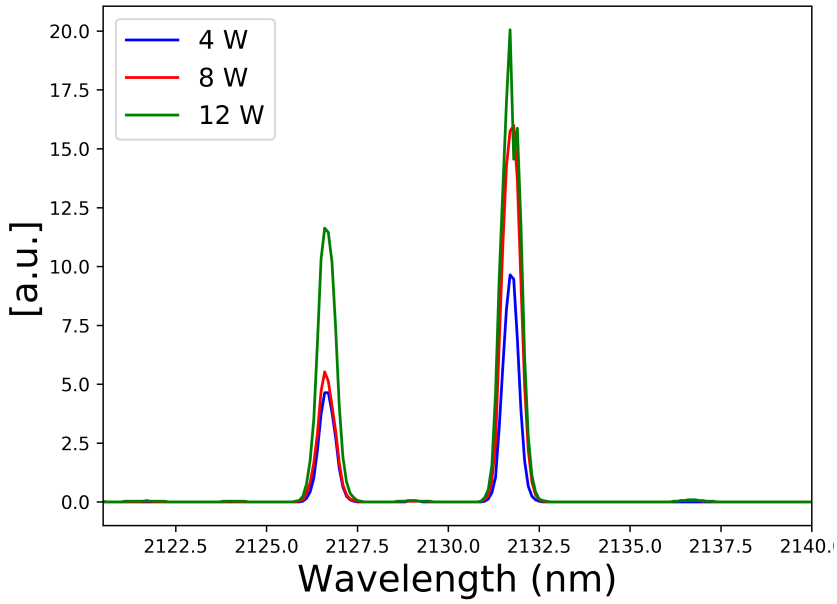

Figure 3.16: Spectrum of signal and idler at different pump energy values with the VBG at a fixed position

4. Porro-prism, Nd:YAG multi-mJ Q-switched laser

4.1 Introduction

High-energy nanosecond Q-switched laser sources are routinely used in many applications in different sectors like medical systems, laser marking, industrial laser machining, remote sensing. In many situations, the laser is required to work in harsh conditions, such as high temperature variations, mechanical vibrations or great accelerations (e.g. in airborne or aerospace applications) that can strongly affect the alignment of the cavity. Therefore, the study of optical solutions suitable to minimize the resonator sensitivity to misalignment is of great interest. One of the most extensively applied techniques to enhance the resonator stability makes use of Porro prisms instead of regular flat mirrors [57], [58]. Porro prisms, otherwise referred to as "right angle" prisms, have the property that an optical ray incident on the prism is back-reflected parallel to the initial propagation direction, no matter was the angle of incidence. Due to this property, a Fabry-Perot resonator configuration employing crossed roof Porro prisms instead of flat end-mirrors highly improves the misalignment tolerances [59]. Indeed, by "crossing" the Porro prisms, so that the apexes are at 90° to each other, any misalignment in one direction is compensated for by one prism and any misalignment in the orthogonal direction is compensated for by the other prism, thus making the resonator highly insensitive to misalignment.

One of the main drawback of this cavity configuration is given by the phase change in the polarization produced by these prisms, because of the out of plane total internal reflections that

takes place inside the prisms. This effect must be taken into account in the design of the laser resonator, in particular when dealing with intracavity polarization-sensitive components, as usually happens, e.g., in actively Q-Switched laser sources. For this reason, a proper resonator modeling based on Jones' matrixes formalism (see Appendix A for some details about Jones matrixes) is often required when dealing with Porro prisms resonators. The other principal drawback is represented by the "petal-like" structure of the transverse modes sustained by Porro prisms resonators, due to the presence of the apexes of the prisms, which limit the beam quality.

In this chapter I will describe the design and experimental results obtained with a multi-mJ, side-pumped Nd:YAG Q-Switched nanosecond laser I developed during my last year of PhD. This laser source was originally intended as a possible seeder for a more complex MOPA laser at 1064 nm for a spaceborne atmospheric LIDAR. For this reason, a special attention was devoted to the identification of a simple pump configuration and resonator geometry still offering a reasonably good beam quality and effective mitigation of misalignment sensitivity. To this purpose, I investigated both a Passively Q-switched (PQS) and an Electro-Optical Modulator (EOM) Actively Q-Switched (AQS) resonator configuration.

In Section 4.2 it is described the pump module, the free-running resonator design and the results of Jones matrixes model of the resonator. In Section 4.3 I report a detailed characterization of the misalignment sensitivity of the resonator. In Section 4.4 I present the results I obtained in PQS and AQS regimes in terms of pulse energy/duration, spatial and spectral quality of the pulses and beam pointing stability.

4.2 Porro-prism laser resonator

The experimental setup is shown in Fig. 4.1. The geometrical resonator length was 52 cm. The active medium was a 1%-doped Nd:YAG crystal slab. The slab was shaped in a triangular form, with lateral facets cut at the Brewster angle. The 3 mm (height) $\times$ 18 mm (width) facet was AR coated at 808 nm and side-pumped by means of an 8-emitters laser diode stack (Intense Inc.) providing a maximum peak power of 1600 W. The pump diode and laser crystal were mounted on the same metallic plate that was maintained at room temperature by means of a

Peltier module. The radiation emitted by the diode stack was coupled in the active medium trough a properly designed cylindrical thick lens with a lateral width (along z-direction in Fig. 4.1) of 5 mm and a radius of curvature of 5.6 mm in the xy-plane.

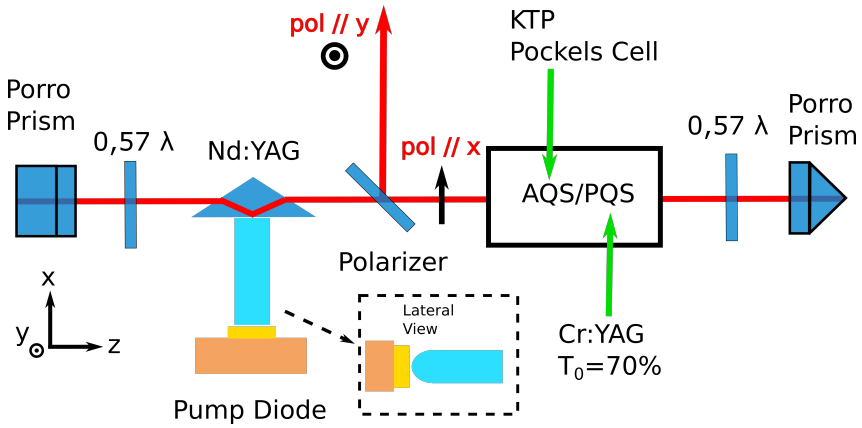

Figure 4.1: Scheme of the cavity architecture. It is possible to identify a *Gain Arm*, the one including the wave-plate and the Porro prism on the left side of the polarizer, and a *Feedback Arm*, the one containing the polarizer, the Porro prism, the wave-plate and the Q-switch (EOM or saturable absorber) on the right side of the resonator

This optical element acted as a pump beam homogenizer in the xz-plane and a focusing element in the xy-plane, hence producing a pump spot on the lateral facet of the Nd:YAG triangular slab of $1/e^2$ diameter $2w_z \times 2w_y \approx 5 \times 1$ mm^2. A pair of fused silica Porro prisms (1-inch diameter) were used as end mirrors of the linear resonator. The prisms where inserted in a kinematic mounting that permitted tip-tilt in the xy plane (Thorlabs model KM100) in combination with precise rotation (1° tolerance) along z-axis (Newport model RM25A). The prisms were oriented so to have their apexes laying in the the xy-plane and forming a 45° angle with respect to the x-axis. Because of the specular reflection of the cavity mode at the pumped facet of the active medium, this arrangement corresponded to the crossed-Porro configuration yielding the highest misalignment insensitivity for the resonator. A 0,57λ retarding quartz wave-plate (WP) was employed in front of each Porro prism to compensate for the polarization rotation induced by the out-of-plane total internal reflections taking place in the Porro prisms. A 45° Thin Film Polarizer (TFP) acted as output coupling element of the resonator. According

to the notation introduced in [60], the 0,57λ WP positioned in the "gain arm" (left side of the resonator with respect to TFP in Fig. 4.1) was adjusted for minimum roundtrip losses, whereas through the rotation of the optical axis of the 0,57λ WP of the "feedback arm" (right side of the resonator with respect to TFP in Fig. 4.1) we realized the output coupling of the resonator. Modeling the evolution of laser beam polarization inside the resonator with Jones matrixes formalism, one can predict the equivalent output coupling through the TFP. In Fig. 4.2 we report the comparison between our simulations and experimental measurement of the effective transmission realized in the feedback arm.

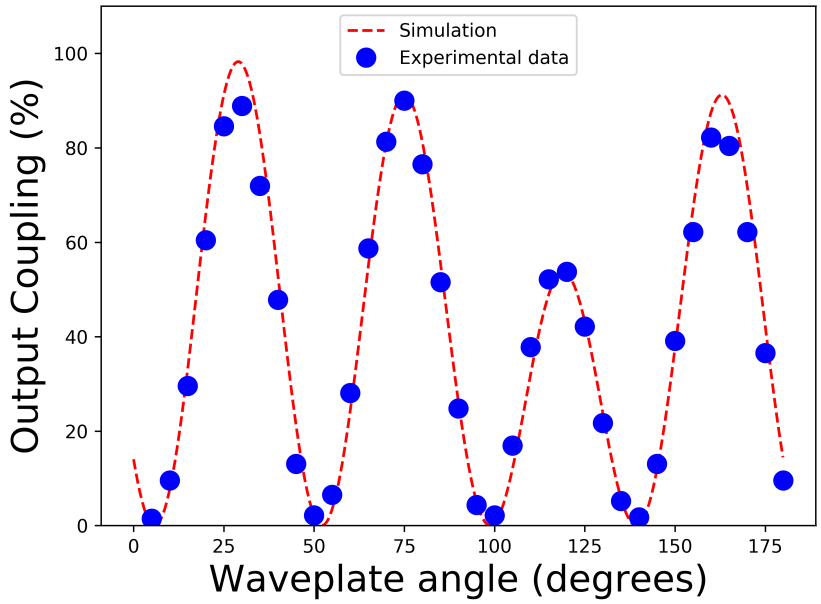

Figure 4.2: : Feedback arm equivalent output coupling transmission as a function of the 0,57λ WP optical axis angle of rotation (0° correspond to WP optical axis perpendicular to the x-z-plane). The result of simulations based on Jones matrixes formalism is shown in dashed red line, experimental measurements in blue dots

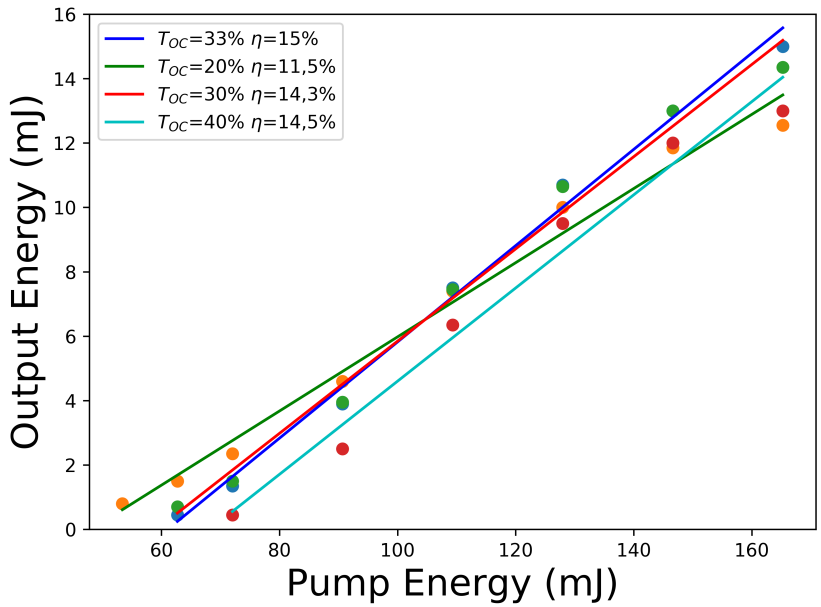

Figure 4.3: Free-running regime characterization

At first, we operated the laser in free-running regime at a pump repetition rate of 20 Hz. Pump pulse duration was set to 150 μs during all the experiments in order to guarantee a reasonable trade-off between pump energy deposition and Nd:YAG upper energy level storage efficiency. This corresponded to a nominal available maximum pump energy $\mathrm{E}_{p,max} = T_p \cdot P_{peak} = 240$ mJ. In order to determine the effective pump energy incident on the Nd:YAG slab, we characterized the transmission of the pump-coupling cylindrical lens. Despite a nominal AR coating at 808 nm, the transmission of the lens was as low as 67%, resulting in a maximum available pump energy at the pumped facet of the Nd:YAG slab $\mathrm{E}_{p,max} \simeq 160$ mJ. A possible explanation of the poor performance of the coating can be the highly out-of-normal incidence of the divergent pump stack-diode radiation on the curved surface of the cylindrical lens that was put in proximity of the diode emitters (see inset of Fig. 4.1).

The output energy as a function of the incident pump energy for different values of the output coupling is shown in Fig. 4.3. Optimum coupling resulted T_{OC} = 33%, yielding a maximum output energy E_{max} = 15 mJ. The maximum slope efficiency η = 15% with respect to the incident pump energy was obtained with T_{OC} = 33%.

4.3 Misalignment sensitivity characterization

Since Porro prisms are employed mainly for their tolerance to misalignment, the analysis of the latter was a crucial point for the characterization of our architecture. In free-running regime we characterized the misalignment sensitivity of the resonator by measuring the output energy as a function of the angular deviations of the end prisms with respect to optimum position. Starting from the best alignment condition (output power = 100%) the Thorlabs kinematic mounts were misaligned and the output power was recorded. The angular resolution offered by the mirror mounts was about 0,8 mrad.

The result of the measurement is presented in Fig. 4.4 for both the gain and feedback arm Porro prisms. As expected, each Porro presents an "insensitive" axis and a critical one and the two are orthogonal to each other thanks to the crossed Porro configuration adopted. Output power remains almost constant at about 90% of its maximum value for a misalignment angle of about 50 mrad in the insensitive direction for each prism.

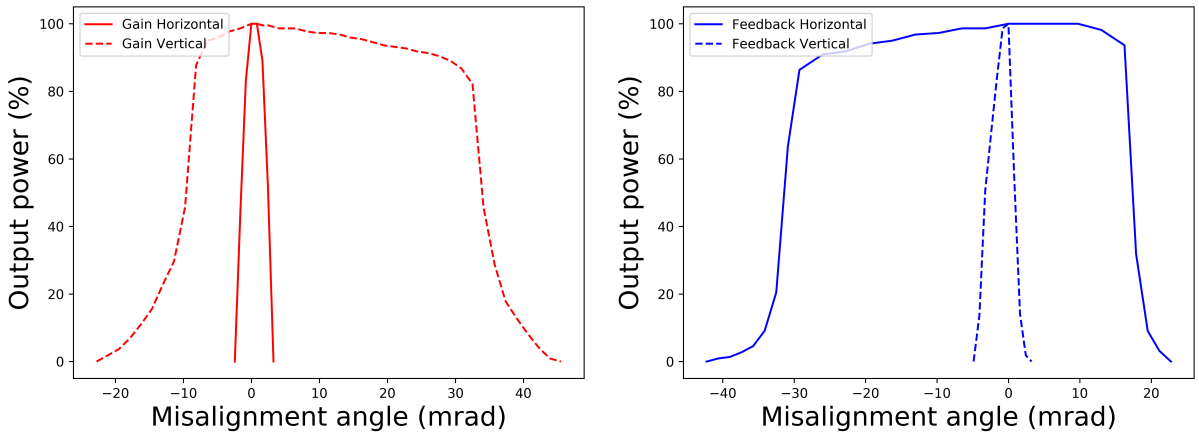

(a) (b)

Figure 4.4: Misalignment measurements for the Porro prism oscillator

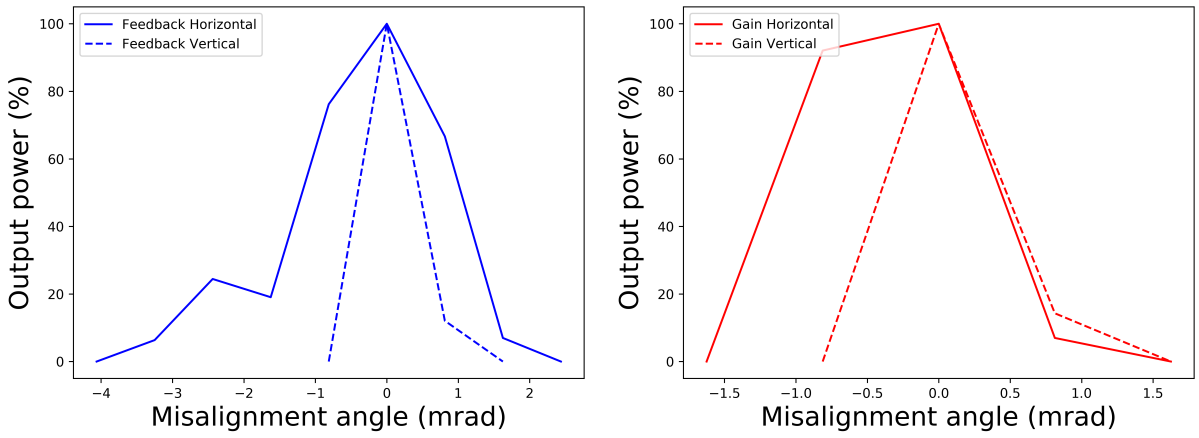

(a) (b)

Figure 4.5: Misalignment measurements for the plane-plane oscillator

In order to have a quantitative estimation of the improvement due to the employment of these prisms, two other resonator architectures were tested. The first architecture was a plane-plane cavity where the two prisms were replaced by a couple of HR mirrors coated at 1064 nm. The results of the misalignment measurements are shown in Fig. 4.5. The sensitivity of the mirror mount was not accurate enough to provide a detailed characterization of the tolerance. It is however clear that a misalignment of less than 2 mrad could decrease the output energy to level lower than 10% of its maximum. The different behavior of the horizontal plane (more insensitive), with respect to the vertical (more sensitive), can be explained if one considers the peculiar shape of the gain volume in the active medium which is asymmetric with a vertical extension smaller then the horizontal.

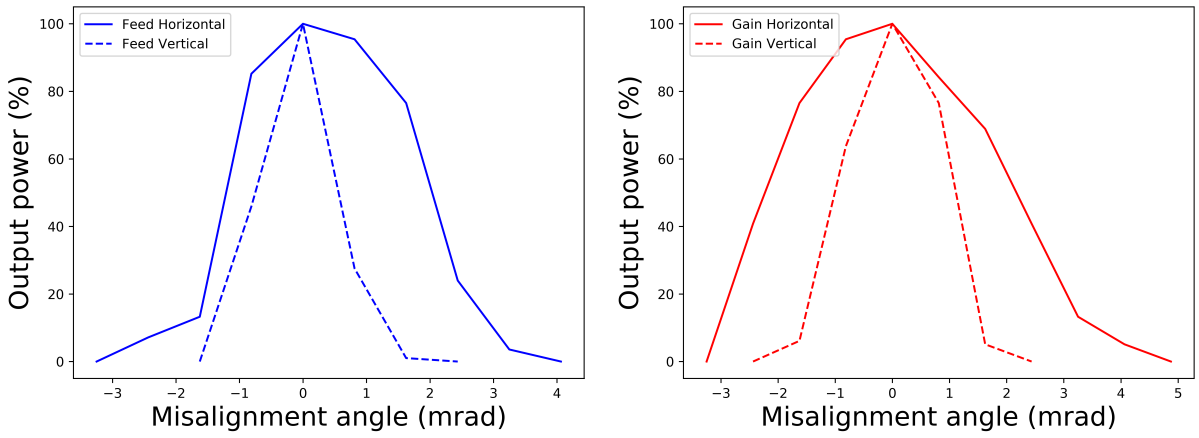

(a) (b)

Figure 4.6: Misalignment measurements for the plane concave oscillator

The other design tested was a plano-concave cavity where the Porro prism in the Gain arm was replaced by a concave mirror with a radius r=1000 mm and the Feedback arm Porro prism was replaced by a plane mirror HR coated at 1064 nm. This cavity was designed to provide a similar spatial beam quality of the Porro prism resonator ($M_x^2 \times M_y^2 \approx 10 \times 10$). The results of the misalignment measurements are shown in Fig. 4.6. The misalignment is slightly improved since the output power maintains a value higher than 50% of its maximum for a range of ≈ 3-6 mrad of misalignment angle.

We can conclude that the use of Porro prism as end mirrors can increase the tolerance to misalignment of the resonator of more than one order of magnitude.

4.4 Passive and Active Q-switching experimental results

For the PQS experiments, we employed Cr:YAG saturable absorbers with different initial transmission T_0 = 90% and 70%. Best results in terms of output pulse energy were obtained with the T_0 = 70% saturable absorber, yielding 7−mJ. Employng the saturable absorber with T_0 = 90% the output energy dropped to 3,5 mJ. The oscilloscope trace of the 46-ns-long, 7-mJ pulses is shown in Fig. 4.7. Laser resonator output coupling was adjusted to optimize the output pulse energy and was 36%. The measured pulses optical spectrum of 37 pm FWHM bandwidth centered at

1063,97 nm (see Fig. 4.8), was close to the resolution of the instrument (20 pm, ANDO optical spectrum analyzer, model AQ6317B). The oscilloscope trace of the PQS pulses presented in Fig. 4.7 was recorded with a 2 GHz photodiode (model EOT3000) and 1 GHz bandwidth oscilloscope (Tektornix TDS5104B) and clearly shows the presence of multi-longitudinal modes beats. A FFT of the signal (see inset of Fig. 4.7) reveals the presence of at least 5 oscillating modes.

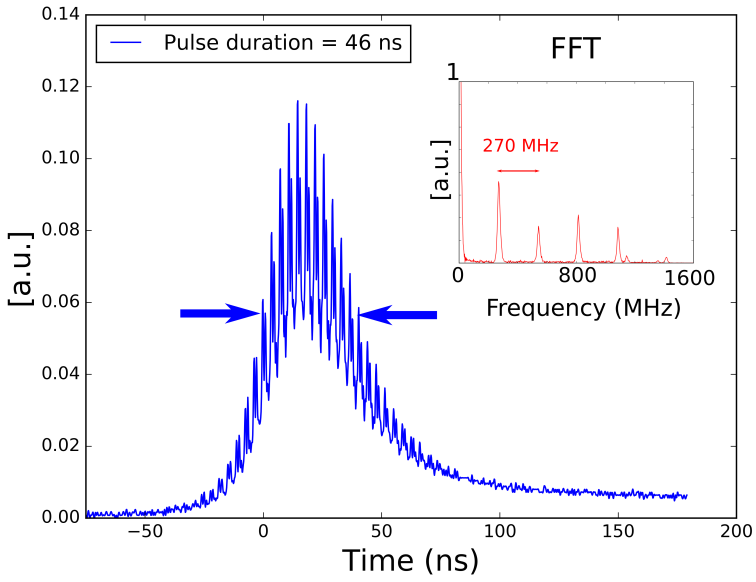

Figure 4.7: Oscilloscope trace of the pulses in PQS regime. In the inset it is shown the computed FFT of the signal revealing the longitudinal modes revealing longitudinal modes equally spaced of a resonator FSR

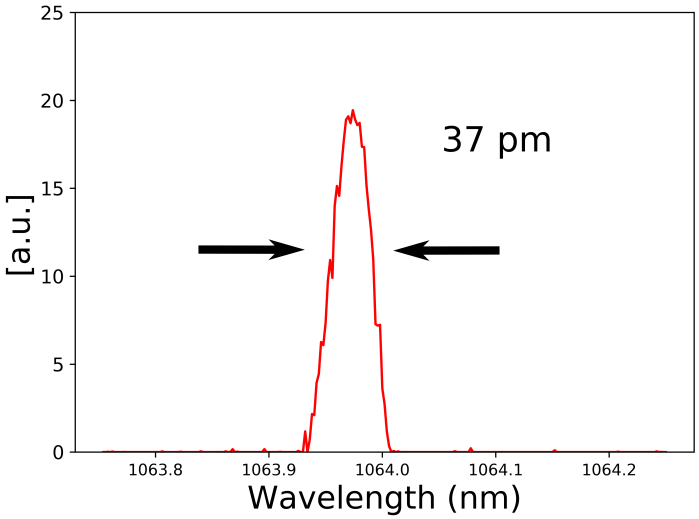

Figure 4.8: Optical spectrum of the pulses in PQS regime

One of the main drawback of PQS laser is represented by the intrinsic pulse jitter. We characterized it by measuring the time delay between the pump pulse rising edge and the Q-Switching pulse rising edge with a mean value of 133 μs and a standard deviation of $\approx$ 700 ns.

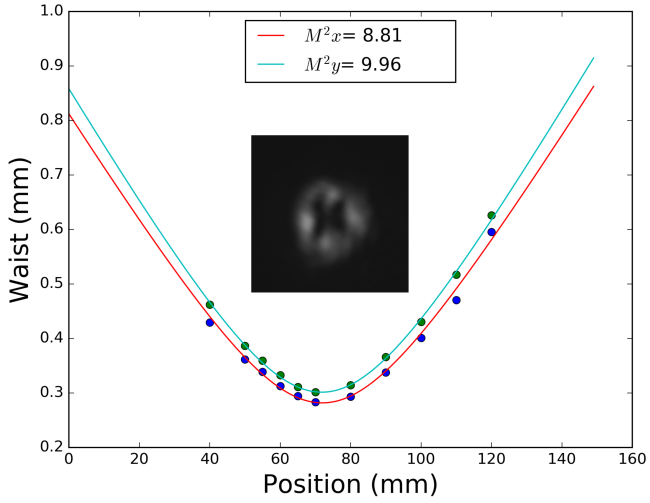

Figure 4.9: Spatial beam quality measurement for the PQS configuration

Spatial beam quality of the PQS laser was measured by scanning a CCD camera along the focal plane of a f = 175 mm spherical lens put at the output of the laser resonator. A $M_x^2 \times = M_y^2$

8,8 × 9,9 was obtained as it can be seen in Fig. 4.9. This relatively high M^2 value is quite typical for side-pumped configuration and Porro prisms resonators [61].

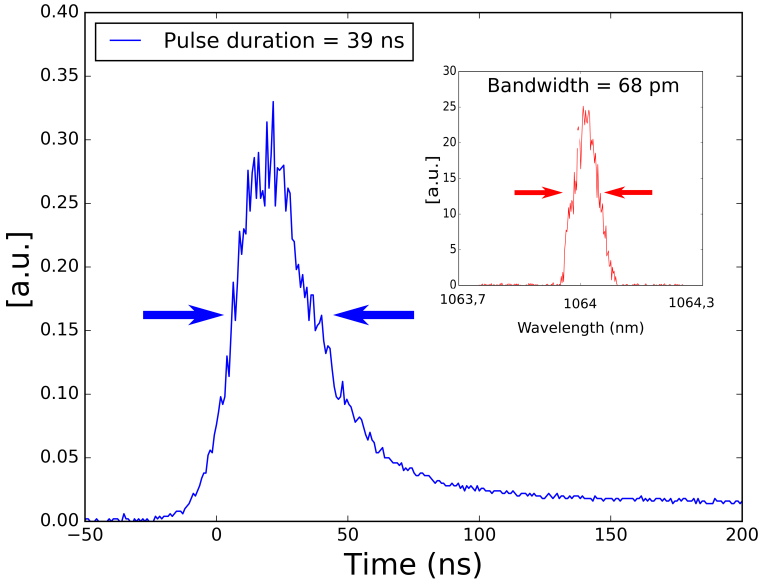

Figure 4.10: Pulse duration and spectrum of the AQS laser

For active Q-Switching we employed a double 7 × 7 mm^2 × 5 mm (length of the single element), matched RTP Pockels cell with a half-wavelength voltage of 2,4 kV. The output coupling of the laser was controlled through the voltage applied to the Pockels cell, being the 0,57λ WP of the feedback arm (see Fig. 4.1) oriented for ideal 100% output coupling when the switch was "off". In order to operate in a safe condition for possible intracavity element optical damage, we maintained the output coupling transmission to 40% during the AQS experiments. In these operating conditions, the maximum pulse energy was 10.5 mJ, with a corresponding pulse duration of 39 ns. Pulse oscilloscope trace and the pulse optical spectrum (68 pm FWHM bandwidth centered at 1064,01 nm) are shown in Fig. 4.10. The output pulse energy and pulse duration as a function of the incident pump energy in AQS regime are shown in Fig. 4.11. At the maximum incident pump energy, the pulse peak power exceeded 250 kW.

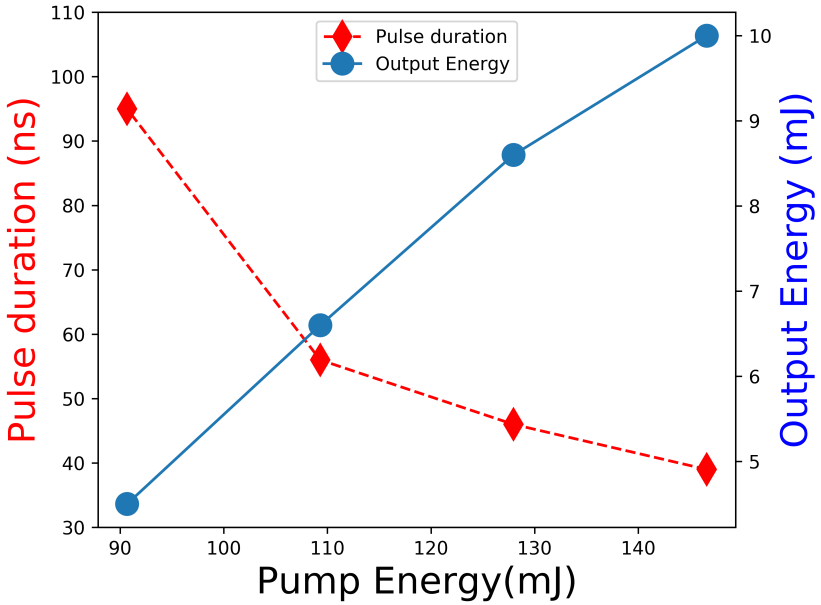

Figure 4.11: Pulse duration and pulse energy as function of the pump energy

The spatial beam quality of the AQS configuration was measured by means of a CCD camera and the results were comparable to the PQS architecture being $M_x^2 \times M_y^2 = 9 \times 9{,}9$ (see Fig. 4.12)

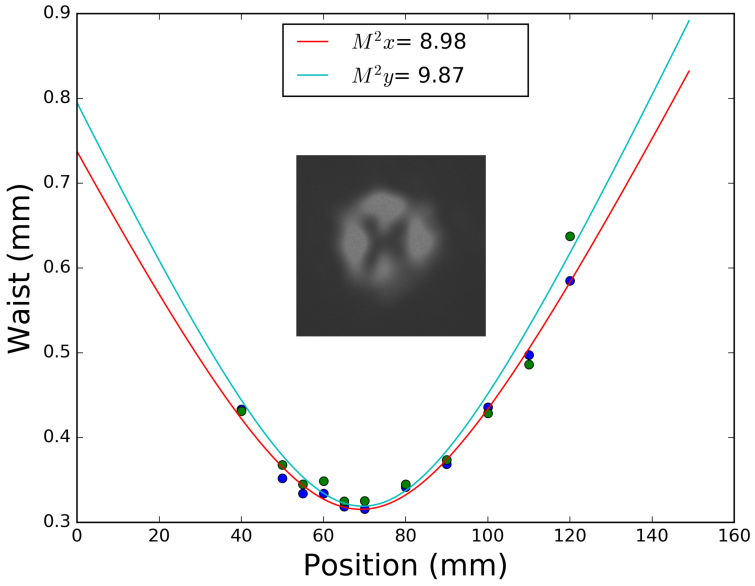

Figure 4.12: Spatial beam quality measurement for the AQS configuration

4.4.1 Beam pointing stability measurements

The beam pointing stability is the measurement of the fluctuation in the pointing direction of the laser beam due to thermal or mechanical effects.

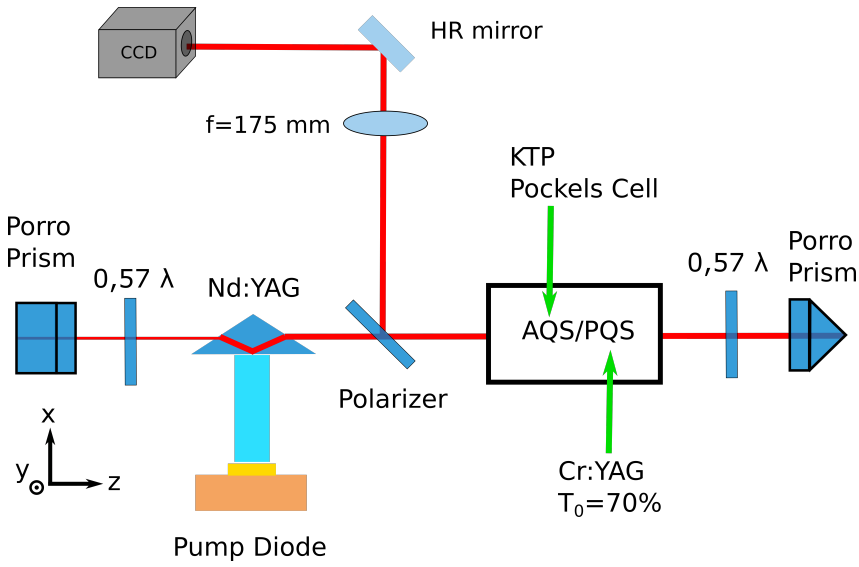

Figure 4.13: Setup for the analysis of the beam pointing stability of the laser oscillator

In Fig. 4.13 it is represented the setup employed for the measurement of the beam pointing stability of the laser. The analysis was carried out by means of a ABCD matrix calculation. In a ABCD matrix model the paraxial laser beam is represented by a ray vector

$$\begin{bmatrix} x \\ \theta \end{bmatrix} \tag{4.1}$$

where x is the displacement of the ray from the optical axis and θ is its angle with respect from the optical axis. Different optical components are represented by different matrices, for example

$$Free\ space\ propagation\ = \begin{bmatrix} 1 & L \\ 0 & 1 \end{bmatrix} \quad Thin\ lens\ = \begin{bmatrix} 1 & 0 \\ \frac{-1}{f} & 1 \end{bmatrix} \tag{4.2}$$

where L and f are respectively the length of the propagation in free space and the focal length of a thin lens. The ray vector and its angular divergence after it has passed trough a series of optical components described by a proper ABCD matrix, can be found with the following

calculation

$$\begin{bmatrix} x_{out} \\ \theta_{out} \end{bmatrix} = \begin{bmatrix} A & B \\ C & D \end{bmatrix} \begin{bmatrix} x_{in} \\ \theta_{in} \end{bmatrix} \tag{4.3}$$

where $\begin{bmatrix} A & B \\ C & D \end{bmatrix}$ is the matrix describing the optical setup, i.e., product of all the matrix representing the optical elements.

The measurement setup for our analysis consisted of a focusing lens of focal length 175 mm, a HR mirror and a CCD camera. The beam was focused by the lens into the CCD camera placed at a distance L=175 mm from the lens, in order to measure the beam profile in the focus.

$$\begin{bmatrix} x_f \\ \theta_f \end{bmatrix} = \begin{bmatrix} 1 & 0 \\ \frac{-1}{f} & 1 \end{bmatrix} \begin{bmatrix} 1 & L \\ 0 & 1 \end{bmatrix} \begin{bmatrix} x_{in} \\ \theta_{in} \end{bmatrix} \tag{4.4}$$

In our case the free propagation distance $L = f$. If we carry out the calculations

$$\begin{bmatrix} x_f \\ \theta_f \end{bmatrix} = \begin{bmatrix} \theta_{in} f \\ \theta_{in} - \frac{x_{in}}{f} \end{bmatrix} \tag{4.5}$$

From equation 4.5 it is possible to notice that x_f=$\theta_{in} f$ and thus

$$\partial x_f = \partial \theta_{in} f. \tag{4.6}$$

From equation 4.6 follows that any instability in the pointing direction of the input beam in the measurement setup can be calculated from an instability in the position of the focus by $\partial\theta_{in}$= $\partial x_f / f$. The CCD camera captured 100 images of the beam in a span of 5 minutes. The images were analyzed by a MATLAB code that calculated the centroid of the beam in each image. To obtain the beam pointing stability the standard deviation of the 100 samples was divided by the focal length of the lens. The beam pointing stability, i.e. the standard deviation of the angular divergence of the laser, was found to be 7 μrad for the PQS configuration 4 μrad for the AQS configuration. The results are shown in Table 4.1.

4.5 Summary of PQS and AQS performance

In Table 4.1 there is a comparison between the results obtained in both PQS and AQS regime: it is clear that generally AQS can provide better results especially in terms of output energy

and jitter of the output pulse with respect to the pump pulse. These advantages however come with the price of the increased complexity (mostly for the electronics required) and therefore with the increased cost, making the PQS architecture the best choice whenever the pulse jitter is not of concern for the application, as it is usually the case for example in range finding applications. In some applications however, where the specifications on the jitter are particularly strict (LIDAR), the choice is forced on the AQS configuration.

	PQS	**AQS**
$\mathbf{M_x^2 \times M_y^2}$	8,8×9,9	9×9,9
Pulse duration	46 ns	39 ns
Bandwidth	37 pm	68 pm
Beam Pointing Stability	7 μrad	4 μrad
Jitter	700 ns	90 ns
Pulse Energy	7 mJ	10 mJ
Pulse Peak Power	150 kW	250 kW

Table 4.1: Comparison for the results for the two architectures of AQS and PQS

5. Conclusions

During my PhD I studied different types of high energy, narrow bandwidth, master oscillator power amplifier laser architectures for various applications, ranging from nonlinear optics to remote sensing. In all the projects I took part the bandwidth of the laser was a critical parameter for either fulfilling certain conditions for the LIDAR system or for an efficient frequency down-conversion in the nonlinear optics applications.

In addiction, I had the opportunity to design and characterized a multi-mJ, side-pumped Nd:YAG Q-switched nanosecond laser originally intended as a possible seeder for a more complex MOPA laser at 1064 nm for a space-borne atmospheric LIDAR.

At the beginning of my PhD, I developed a MOPA laser system capable of generating SLM high energy pulses (3,2 mJ) with a narrow bandwidth (63 MHz) and excellent beam quality. The system is composed by a gain switched microchip seeder, an high-gain, double-pass CW-pumped amplification stage and a QCW-diode-pumped, two-stages booster amplifier. Owing to the high peak power (250 kW) and extremely good spectral and spatial beam quality of the generated nanosecond laser pulses, this complex MOPA laser system at 1064 nm proved to be an excellent source for nonlinear optics experiments, namely for SRS frequency down-conversion in the visible.

We exploited the good properties of $SrWO_4$ crystal, by pumping it with the second harmonic of the MOPA pulses, thus obtaining wavelength shifted pulses at 559 nm with a duration of 3,3 ns and a maximum energy of about 0,18 mJ, corresponding to a high peak power of about 50 kW. To this purpose we took advantage of a significant SRS threshold reduction permitted by the low-finesse Fabry-Perot resonator effect taking place in the Raman crystal. Despite an extremely simple SRS experiment setup, we could demonstrate a very good beam quality (M^2 = 1,3) at 559 nm. We also carefully characterized the longitudinal mode content of the Raman

shifted pulses. About 15% of the generated pulses resulted SLM, the remaining 85% contained only two or seldom three longitudinal modes, confirming the very high spectral purity of the Raman generated pulses.

The second project realized was a, high-energy and high spectral purity MOPA laser system tunable around 2130 nm, based on an OPO followed by an OPA pumped by a commercial nanosecond, narrow-bandwidth, high-energy laser at 1064 nm. The tuning of the plane-concave Fabry-Perot cavity OPO was realized with a chirped Volume Bragg Grating (VBG) with a peak reflectivity at 2130 nm and about 20 nm tuning range. The nonlinear crystals employed in these experiments were periodically-Poled, Rb-doped, large-area KTP crystals specifically designed and realized at the Laser Physics department of the KTH in Stockholm.

The maximum output energy of the OPO was 1,5 mJ with a pump of 7 mJ, corresponding to about 5% of the available pump energy. The maximum pump energy level was dictated by the damage threshold of the VBG which was the most delicate component of our OPO. The measurements confirmed the theoretical expectations as the source generated narrowband pulses (7 ns for 0,4 nm of bandwidth) that could be tuned in a range of 1,5 THz. The remaining 95% of the pump energy was used to pump the OPA in which the same nonlinear material used for the OPO (PP-RKTP) was employed. At the end of the amplification chain we obtained 52 mJ total energy (signal+idler) at 2 μm with well-preserved spectral properties and a fairly good beam quality. This rather complex MOPA laser system is intended to be a flexible platform for THz generation in semiconductor materials through difference frequency generation.

In addition to the intense experimental activity I carried out developing complex MOPA laser systems operating in different regimes and wavelength regions, I also had the opportunity to study simple laser architectures, employing few, well tested and technologically mature components for direct generation of mJ-level nanosecond pulses in diode-pumped oscillators operating at 1 μm. In particular, I concentrated my attention on Porro prism laser oscillators, which are routinely used in remote sensing, space-borne and military applications, where the laser is supposed to be working in harsh conditions.

To this purpose I studied and built a multi-mJ, polarization coupled, Porro prism laser oscillator operating in nanosecond AQS and PQS regime. The characterization of the laser I realized is comprehensive of a spatial and spectral beam quality analysis, a detailed characterization of

the misalignment tolerance guaranteed by the Porro prism resonator, as well as measurements of the output pulse energy, jitter and beam pointing stability. Best results in terms of output pulse in PQS regime energy were obtained with the T_0 = 70% saturable absorber, yielding 7-mJ, 46-ns pulses (150 kW peak power). In AQS regime, we demonstrated a maximum pulse energy of 10,5 mJ, with a corresponding pulse duration of 39 ns (250 kW peak power). The use of Porro prism as end mirrors of the linear resonator in substitution of the usual plane or concave mirrors allowed a more than one order of magnitude reduction of the misalignment sensitivity of the resonator.

A. Jones calculus

It is often necessary to determine the nature of the polarization of a light beam which has passed through various anisotropic optical elements. Such elements alter the nature of the polarization of light and can be placed both outside and inside the laser resonators. If such elements are placed inside the resonator, they not only alter the polarization of the output radiation but also change significantly the losses in the resonator.

Calculations of the polarization state of a light beam propagating through anisotropic optical media or inside resonators containing such optical elements can be performed successfully by applying the Jones matrix method [62].

In addition, Jones method can yield the values of the parameters which determine the steady-state polarization and the losses in optical systems comprising any number of optically anisotropic elements and can be quite easily implemented on computer.

In Jones calculus, the electrical field associated to the polarized light beam is represented by a complex, two-components vector. For example, if we consider a linearly polarized beam

$$E(z,t) = \hat{\mathbf{x}} E_x e^{-i(\omega t - kz + \sigma_x)} + \hat{\mathbf{y}} E_y e^{-i(\omega t - kz + \sigma_y)} \tag{A.1}$$

It is possible to define $E_0 = \sqrt{E_x^2 + E_y^2}$ and thus the Jones vector of the light beam becomes

$$\begin{bmatrix} E_0 e^{-i\sigma_x} \\ E_0 e^{-i\sigma_y} \end{bmatrix} \tag{A.2}$$

where σ_x and σ_y are the phase shifts in the x and y directions respectively.

If we consider for example a linearly polarized wave along the x axis with an amplitude of E_0 its Jones vector will be

$$E_0 \begin{bmatrix} 1 \\ 0 \end{bmatrix} \tag{A.3}$$

Similiarly if we consider a circular polarization with the same amplitude the Jones vector will be

$$\frac{E_0}{\sqrt{2}} \begin{bmatrix} 1 \\ i \end{bmatrix} \tag{A.4}$$

since a in a circular polarization the component in each direction have the same amplitude and a phase shift $\sigma = \pi/2$ ($\exp(i\pi/2) = i$).

In Jones calculus, the effect of the optical elements on the polarization state of the light beam is described by a 2×2 transfer matrix. Here I report the Jones matrixes for the most common components that can be fine in an optical setup.

$$\begin{cases} Horizontal\ Polarizer = \begin{bmatrix} 1 & 0 \\ 0 & 0 \end{bmatrix} \\ Rotation = \begin{bmatrix} cos(\theta) & sin(\theta) \\ -sin(\theta) & cos(\theta) \end{bmatrix} \\ Phase\ delayer = \begin{bmatrix} 1 & 0 \\ 0 & e^{i\sigma} \end{bmatrix} \end{cases} \tag{A.5}$$

The first matrix in equation A.5 describes a linear polarizer oriented along the x axis. Indeed, every vector that is multiplied by that matrix keeps only its horizontal component. The second matrix is called the rotation matrix and describes a change of coordinate system. For example, if a wave is linearly polarized at 45° from the horizontal plane and passes through a horizontal linear polarizer, the output can be calculated as follows

$$\begin{bmatrix} \frac{1}{\sqrt{2}} \\ 0 \end{bmatrix} = \begin{bmatrix} cos(-\pi/4) & sin(-\pi/4) \\ -sin(-\pi/4) & cos(-\pi/4) \end{bmatrix} \begin{bmatrix} 1 & 0 \\ 0 & 0 \end{bmatrix} \begin{bmatrix} cos(\pi/4) & sin(\pi/4) \\ -sin(\pi/4) & cos(\pi/4) \end{bmatrix} \begin{bmatrix} 1 \\ 0 \end{bmatrix} \tag{A.6}$$

From another point of view it can be said that the combination of two rotation matrix and the horizontal linear polarizer matrix are equal to the 45° polarizer matrix.

The last matrix in (A.5) models the phase shift introduced by an anisotropic medium between two orthogonal polarizations. For example it is possible to describe a half-wavelength retarding waveplate whose optical axis is oriented at an angle β from the horizontal plane with the following Jones matrixes

$$\begin{bmatrix} cos(2\beta) & sin(2\beta) \\ sin(2\beta) & -cos(2\beta) \end{bmatrix} = \begin{bmatrix} cos(-\beta) & sin(-\beta) \\ -sin(-\beta) & cos(-\beta) \end{bmatrix} \begin{bmatrix} 1 & 0 \\ 0 & -1 \end{bmatrix} \begin{bmatrix} cos(\beta) & sin(\beta) \\ -sin(\beta) & cos(\beta) \end{bmatrix} \tag{A.7}$$

More in general, any component that introduces a phase shift ϕ and is rotated by an angle θ with respect to the x-axis, can be described by

$$M(\phi, \theta) = \begin{bmatrix} cos(-\theta) & sin(-\theta) \\ -sin(-\theta) & cos(-\theta) \end{bmatrix} \begin{bmatrix} 1 & 0 \\ 0 & e^{i\phi} \end{bmatrix} \begin{bmatrix} cos(\theta) & sin(\theta) \\ -sin(\theta) & cos(\theta) \end{bmatrix} \tag{A.8}$$

When a wave passes through an anisotropic element or a system of such elements, the state of its polarization normally changes. However, there are some states of polarization of an incident wave which are not affected by a given element. These states are known as the eigenpolarizations.

The problem of finding eigenpolarization states reduces to the determination of the eigenvalues and the eigenvectors of the Jones matrix M representing the single optical component or the cascading of an arbitrary number of optical components.

.

B. Terahertz sources and applications

The Terahertz gap is a fraction of the electromagnetic spectrum that separates the optical frequencies from microwaves, in particular, usually, with THz gap it intended the spectral region extending from 0,3 THz to 10 THz.

In 1995 the first imaging system based on terahertz time-domain spectroscopy was developed [63]. In the early 2000s the interest in this part of the spectrum due to its possible application in high speed optical communications, medical diagnostic, public security and spectroscopy to name a few, has drawn a lot of scientific effort worldwide in order to provide the scientific and industrial opto-electronic community with efficient Terahertz sources and detectors.

The challenges in the adoption of the Terahertz radiation in the above mentioned fields are mainly due to the lack of efficient sources and receivers. A lot of technologies are being developed in order to fill this gap, such as up-conversion from microwave frequencies, vacuum electronics, quantum cascade lasers (QCL, which are the most promising solution) etc... [64]. In this appendix a brief review of Terahertz sources and applications will be presented.

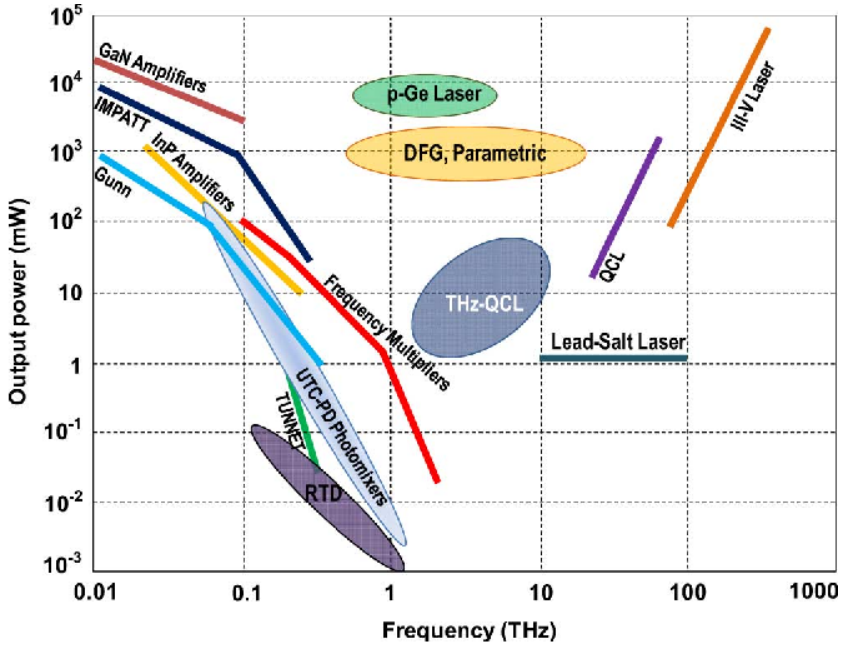

Figure B.1: Illustration of the general Terahertz sources [65]

CO_2 narrow bandwidth laser have been employed as sources for **Optically Pumped** CH_3OH THz lasers. These systems exploit the molecular rotational transitions of the gas and are able to emit narrow bandwidth radiation (in the MHz range). The disadvantages of these sources is their intrinsic dependence on the molecular structure of the gas which limits their tunability.

Recently Quantum Cascade Lasers (or QCL) have proven to be a very promising alternative for the generation of THz waves. QCL are semiconductor lasers composed by a series of Quantum Wells coupled made by nanometers-thick layers of GaAs and AlGaAs. The thickness of the quantum wells is the parameter defining the transition level of the electrons and, thus, defining the energy of the photons emitted. QCL THz lasers have recorded output power in the ranges of hundred of mW, moreover their semiconductor nature makes them excellent candidates for low cost applications. The main drawback with QCL is their working temperature. These systems, indeed, need to be cooled down to $\approx$ 160 K in order to provide enough power for the applications that make THz such an attractive region of the electromagnetic spectrum. A lot of research, anyway, is being carried on to increase the working temperature of QCL THz lasers.

One of the most popular techniques for THz generation, especially for scientific purposes,

is the employment of ultrashort laser pulses for the optical pumping. The optical pumping can be divided in two main branches: the use of **Photoconductive Antennas** or the exploitation of the **Optical Rectification**.

When a Photoconductive Antennas is illuminated by a laser pulse with a duration ≈ 100 fs a transient photocurrent is generated. The transient photocurrent then drives the antenna and is re-emitted in the form of a broadband THz wave.

The Optical Rectification exploits the nonlinearity of certain semiconductor meterials (ZnTe, $LiNbO_3$, GaAs, and GaSe) and generates a THz radiation whose frequency depends on the envelope of the laser pulse illuminating the material. Generally fs-pulses are employed since they have a bandwidth of the order of $\sim$ THz.

Frequency down-conversion has long been popular for the generation of mid-infrared radiation and it has also been exploited for the generation of THz radiation. One of the most efficient choice as source of energetic Terahertz pulses is parametric generation [66]. Parametric generation of Terahertz radiation is based on DFG process, i.e. two very energetic waves whose frequency difference is in the THz range interact in a nonlinear medium creating a third wave whose central frequency is in the THz range.

B.1 Terahertz applications

As mentioned in the previous Section THz radiation has attracted a lot of interest from researcher in different fields. In this short Section it will be given a short review of different applications.

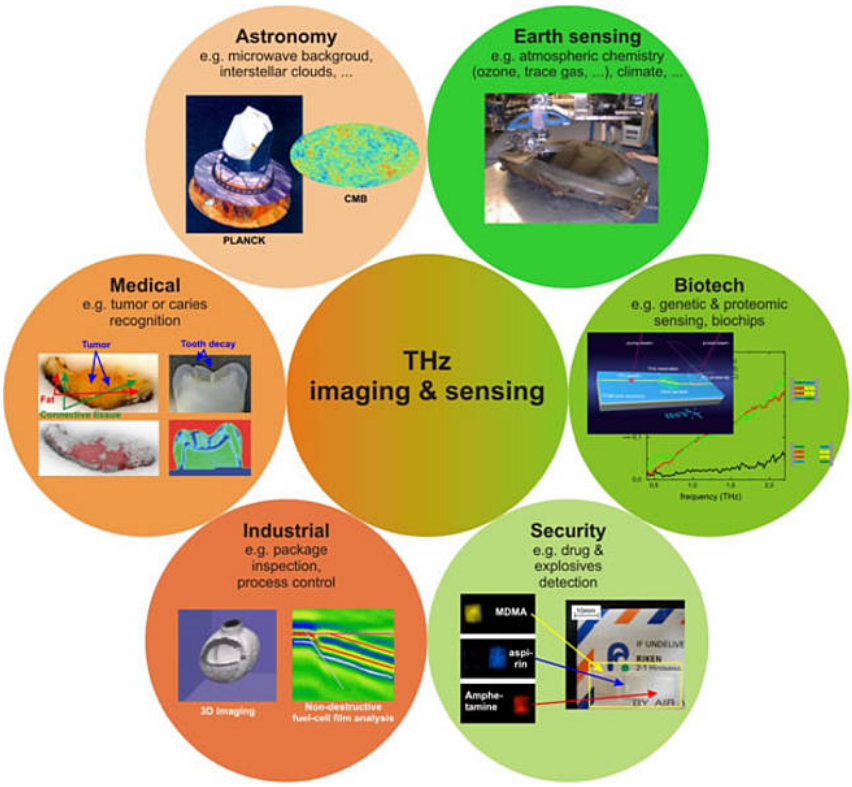

Figure B.2: Illustration of the general Terahertz applications [65]

Increasing food production and its relative quality standards are pushing for a development of faster and more reliable monitoring methods. Infrared radiation have been widely employed for the control of food produced in industrial plants. However near-infrared and middle-infrared can provide limited information about the molecular composition of certain chemicals. THz sources and detectors can exploit the response that residual pesticide exhibits in this frequency range.

In mechanical and civil engineering a lot of different non destructive testing techniques have been developed to monitor the quality of building material. In particular the response of plastic and foam polymer materials to THz radiation makes this type of source very efficient to a failure analysis when these materials are employed [67].

Wood used for building engineering present generally the same properties unrelated to the type of wood. THz radiation however can penetrate better than infrared radiation and presents different absorption coefficient for different kind of wood.

Composite materials have recently proven to be a better choice with respect to common

material thanks to their properties of increased strength, light weight and safety. Different absorption coefficient for different orientation of the fiber composing these materials are particularly enhanced in the THz range. These sources can thus be employed for the analysis of the quality of the fabrication of composite materials.

Due to their resistance to chemical attacks and high temperature ceramic materials have been widely employed in civil engineering. The quality in the fabrication in ceramic strongly depends on the porosity of the final product. It has been proven that low-porosity ceramics present a constant refractive index in the THz range whereas high-porosity sample show a sensible change in the refractive index in this spectrum.

The increasing number of terrorist attacks in public places have pushed the research of novel and more efficient systems for non invasive weapon detection. Some of the most critical parameters are the ability to detect explosives, ceramic weapons and chemical threats. THz radiation can offer a solution which could be easily implemented in the areas more vulnerable to these attacks. It is therefore being pushed a research for the development of security surveillance system. In this framework THz sources and detectors can be an intriguing option for many reasons [68].

- While most common materials are transparent to THz waves, plastic and ceramic present a higher absorption coefficient and can thus be easily spotted.
- Pulsed THz sources can provide the user with radar-like images.
- Different chemicals exhibit different signatures and can be detected even when sealed in a container.
- THz is a non-ionizing radiation and, in contrast to X-rays, can be used with lower health risks.

The non-ionizing nature of THz waves makes them excellent alternatives to X-rays also for biomedical imaging and spectroscopy. Since they can penetrate hundreds of microns in the skin they can be used in the skin disease diagnosis, or, more generally, in tissue characterization. Moreover it is possible to distinguish between molecules with the same molecular

formula, but with different structural forms (isomers) since the vibrational modes corresponding to protein tertiary structural motion lie in the THz range [69].

In the pharmaceutical industry time domain spectroscopy has found an important applications in the detection of polymorphs. Crystal polymorphs are defined as substances that are chemically identical but exist in more than one crystal form. Different polymorphs exhibit different response to THz radiation and can thus be easily identified with this technique. THz time domain imaging can also be used for analysis and characterization of coating thickness and uniformity [70].

Bibliography

[1] H.J.Booth, "Recent applications of pulsed lasers in advanced materials processing," *Thin Solid Films,Volumes*, vol. 453–454, pp. 450–457, 2004.

[2] F. Pirzio, "Special issue on solid state lasers materials, technologies and applications," *Applied Science*, vol. 8, no. 3, p. 460, 2018.

[3] A. Gil-Villalba, R. Meyer, R. Giust, L. Rapp, C. Billet, and F. Courvoisier, "Single shot femtosecond laser nano-ablation of cvd monolayer graphene," *Scientific Reports*, vol. 8, no. 1, p. 14601, 2018.

[4] Y. Nakata, M. Yoshida, and N. Miyanaga, "Parallel fabrication of spiral surface structures by interference pattern of circularly polarized beams," *Scientific Reports*, vol. 8, no. 1, p. 13448, 2018.

[5] J. Blackburn, "Laser welding of metals for aerospace and other applications," *Welding and Joining of Aerospace Materials*, no. 3, pp. 75–108, 2012.

[6] E. R. Kayvan Shokrollahi and M. Murison, "Principles and surgical applications," *The Journal of Surgery*, vol. 2, no. 1, pp. 28–34, 2004.

[7] G. Sauder, E. Ruf, S. Moedl, and R. Thyzel, "Nanosecond laser cataract surgery in locs iii grade 4 and 5: A case series," *The Journal of Surgery*, vol. 2, no. 1, pp. 28–34, 2004.

[8] L. Mastropasqua, P. A. Mattei, L. Toto, A. Mastropasqua, L. Vecchiarino, G. Falconio, and E. Doronzo, "All laser cataract surgery compared to femtosecond laser phacoemulsification surgery: corneal trauma," *INTERNATIONAL OPHTHALMOLOGY*, vol. 37, pp. 475–482, JUN 2017.

[9] K. Fedin, M. Inochkin, L. Khloponin, and V. Khramov, "Subnanosecond 1 j laser for medicine and technology," *Optical and Quantum Electronics*, vol. 49, p. 178, Apr 2017.

[10] T. Drozd, Z. Mierczyk, M. Zygmunt, and J. Wojtanowski, "Free space optical communication based on pulsed lasers," in *Proc. SPIE*, 2016.

[11] B. Huang, Q. Yi, L. Yang, L. Du, L. Miao, C. Zhao, and S. Wen, "Dual-Wavelength Nanosecond Nd:YVO4 Laser With Switchable Inhomogeneous Polarization Output," *IEEE JOURNAL OF SELECTED TOPICS IN QUANTUM ELECTRONICS*, vol. 24, SEP-OCT 2018.

[12] H. Chen, S.-P. Chen, Z.-F. Jiang, and J. Hou, "Diversified pulse generation from frequency shifted feedback Tm-doped fibre lasers," *SCIENTIFIC REPORTS*, vol. 6, MAY 19 2016.

[13] S. Golik, Sergey, Bukin, Oleg, Ilyin, Alexey, I. Tsarev, Vladimir, A. Saluk, Pavel, Shmirko, and Konstantin, "Application of high-power Nd:YAG lasers for environmental monitoring," in *Proceedings of SPIE - The International Society for Optical Engineering*, p. 5627, 2005.

[14] S. Malladi, D. Ramakrishna Rao, S. Mohankumar, B. Presennakumar, S. Muraleedharan Nair, V. Buthiran, R. Sreeja, and S. Ayyalusamy, "Space borne laser radar for atmospheric studies," vol. 561, p. 171, 05 2004.

[15] I. S. McDermid, "Ground-based lidar and atmospheric studies," *Surveys in Geophysics*, vol. 9, pp. 107–122, Jun 1987.

[16] M. R. Topp, "Pulsed laser spectroscopy," *Thin Solid Films,Volumes*, vol. 14, no. 1, p. 1978, 2006.

[17] S. Svanberg, G. Zhao, H. Zhang, J. Huang, M. Lian, T. Li, S. Zhu, Y. Li, D. Zheng, H. Lin, and K. Svanberg, "Laser spectroscopy applied to environmental, ecological, food safety, and biomedical research," *Optics express*, vol. 23, pp. 65–147, 03 2016.

[18] G. S. Katarzyna Komar, "Application of the laser spectroscopy techniques for analysis of pigments on paper," *Proc.SPIE*, vol. 5958, pp. 5958 – 5958 – 8, 2005.

[19] P. Campbell, I. Moore, and M. Pearson, "Laser spectroscopy for nuclear structure physics," *Progress in Particle and Nuclear Physics*, vol. 86, pp. 127 – 180, 2016.

[20] P. Hannaford, "Femtosecond laser spectroscopy," 01 2005.

[21] M. S. Astapovich, A. V. Gladyshev, M. M. Khudyakov, A. F. Kosolapov, M. E. Likhachev, and I. A. Bufetov, "Watt-Level Nanosecond 4.42-mu m Raman Laser Based on Silica Fiber," *IEEE PHOTONICS TECHNOLOGY LETTERS*, vol. 31, pp. 78–81, JAN 1 2019.

[22] M. Rajabi and F. Abrinaei, "High nonlinear optical response of Lanthanum-doped TiO2 nanorod arrays under pulsed laser irradiation at 532 nm," *OPTICS AND LASER TECHNOLOGY*, vol. 109, pp. 131–138, JAN 2019.

[23] B. Nandy, C. Kumar, J. C. Casals, H. Ye, and M. Ebrahim-Zadeh, "Tunable high-average-power optical parametric oscillators near 2 mu m," *JOURNAL OF THE OPTICAL SOCIETY OF AMERICA B-OPTICAL PHYSICS*, vol. 35, pp. C57–C67, DEC 1 2018.

[24] C. S. Rao, S. Kundu, and A. K. Ray, "High repetition rate nanosecond optical parametric oscillator pumped by the third harmonic of a DPSSL," *APPLIED PHYSICS B-LASERS AND OPTICS*, vol. 124, AUG 2018.

[25] F. Cao, F. Donnarumma, and K. K. Murray, "Wavelength dependent atomic force microscope tip-enhanced laser ablation," *APPLIED SURFACE SCIENCE*, vol. 447, pp. 437–441, JUL 31 2018.

[26] M. Vainio and L. Halonen, "Mid-infrared optical parametric oscillators and frequency combs for molecular spectroscopy," *Phys. Chem. Phys.*, vol. 18, no. 2, p. 4266, 2016.

[27] A. Agnesi, L. Carrà, P. Dallocchio, F. Pirzio, G. Reali, S. Lodo, , and G. Piccinno, "50-mj macro-pulses at 1064 nm from a diode-pumped picosecond laser system," *Opt. Express*, no. 19, p. 20316, 2011.

[28] A. Agnesi, L. Carra, R. Piccoli, F. Pirzio, , and G. Reali, "Nd:YVO_4 amplifier for ultrafast low-power lasers," *Opt. Lett.*, 2012.

[29] C. Weitkamp, *Lidar: Range-Resolved Optical Remote Sensing of the Atmosphere*. Springer, 2005.

[30] O. Svelto, *Principles of Lasers*. Springer, 2010.

[31] J. J. Zayhowski and A. Mooradian, "Single-frequency microchip Nd lasers," *Optics Letters*, no. 1, pp. 24–26, 1989.

[32] E.Molva, "Microchip lasers and their applications in optical microsystems," *Optical Materials*, no. 2, 1999.

[33] J. J. Zayhowski, "Q-switched operations of microchip lasers," *Optics Letters*, vol. 16, no. 8, p. 575, 1991.

[34] F. B. Xavier Delen and P. Georges, "Temperature dependence of the emission cross section of Nd:YVO_4 around 1064 nm and consequences on laser operation," *J. Opt. Soc. Am. B*, vol. 28, May 2011.

[35] A. Agnesi and F. Pirzio, "High gain solid-state amplifiers for picosecond pulses," *Advances in Solid-State Lasers: Development and Applications*, no. 11, 2010.

[36] I. C. Vittorio Degiorgio, *Note di fotonica*. Springer, 2012.

[37] P. Farinello, F. Pirzio, X. Zhang, V. Petrov, and A. Agnesi, "Efficient picosecond traveling-wave Raman conversion in a $SrWO_4$ crystal pumped by multi-watt MOPA lasers at 1064 nm," *Appl. Phys. B*, 2015.

[38] O. Lux, S. Sarang, O. Kitzler, and R. P. Mildren, "Intrinsically stable high-power single longitudinal mode laser using spatial hole burning free gain," *Optica*, 2016.

[39] Y. Zhang, F. Pirzio, A. Agnesi, X. Zhang, , and V. Petrov, "200 ps pulse generation at 1180 nm with a $SrWO_4$ raman crystal pumped by sub-nanosecond MOPA laser system," *Laser Phys. Lett.*, 2014.

[40] R. S. Coetzee, X. Zheng, L. Fregnani, F. Laurell, and V. Pasiskevicius, "Narrowband, tunable, 2 μm optical parametric master-oscillator power amplifier with large-aperture periodically poled Rb:KTP," *Applied Physics B.*, 2018.

[41] P. E. Powers, *Fundamentals of Nonlinear optics.* CRC press., 2017.

[42] K. Scholle, S. Lamrini, P. Koopmann, and P. Fuhrberg, "2 μm laser sources and their possible applications," *IntechOpen.*

[43] N. M. Fried and P. B. Irby, "Advances in laser technology and fibre-optic delivery systems in lithotripsy," *Nature Reviews Urology*, no. 9, pp. 563–573, 2018.

[44] J. A. Giordmaine and R. C. Miller, "Tunable coherent parametric oscillation in LiNbO3 at optical frequencies," *Phys. Rev. Lett.*, 1965.

[45] R. Kingston, "Parametric amplification and oscillation at optical frequencies,"

[46] W. Koechner, *Solid-State Laser Engineering.* 2006.

[47] R. Coetzee, N. Thilmann, A. Zukauskas, C. Canalias, and V. Pasiskevicius, "Nanosecond laser induced damage thresholds in $KTiOPO_4$ and $Rb : KTiOPO_4$ at 1 μm and 2 μm," *Optical Materials Express*, no. 9, pp. 2090–2095, 2015.

[48] Brosnan and Byer, "Optical parametric oscillator threshold and linewidth studies," *IEEEE Journal of Quantum Electronics*, no. 6, 1979.

[49] T. Resetar, "Wavelength-locked parametric master oscillator power amplifier for high-energy generation at 2 μm," Master's thesis, KTH, Stockholm, 2012.

[50] L. Wang, T. Xing, S. Hu, X. Wu, H. Wu, J. Wang, and H. Jiang, "Mid-infrared ZGP-OPO with a high optical-to-optical conversion efficiency of 75,7%," *Optics Express*, no. 4, pp. 3373–3380, 2017.

[51] E. B. Petersen, W. Shi, A. Chavez-Pirson, N. Peyghambarian, and A. T. Cooney, "Efficient parametric terahertz generation in quasi-phase-matched GaP through cavity enhanced difference-frequency generation," *Appl. Phys. Lett.*, 2011.

[52] P. G. S. Wei Shi, Yujie J Ding, "High average power, high repetition rate tunable terahertz difference frequency generation with GaSe crystal pumped by 2 μm dual wavelength intracavity KTP optical parametric oscillator," *Optics Communications*, no. 1, 2004.

[53] V. P. Markus Henriksson, Mikael Tiihonen and F. Laurell, "$ZnGeP_2$ parametric oscillator pumped by a linewidth narrowed parametric 2 μm source parametric oscillator pumped by a linewidth narrowed parametric," *Optics Letters*, no. 12, pp. 1878–1880, 2006.

[54] G. Stoeppler, N. Thilmann, V. Pasiskevicius, A. Zukauskas, C. Canalias, and M. Eichhorn, "Tunable mid-infrared $ZnGeP_2$ RISTRA OPO pumped by periodically-poled Rb:KTP optical parametric master-oscillator power amplifier," *Optics Express*, no. 4, pp. 4509–4517, 2012.

[55] J. D. Bierlein and H. Vanherzeele, "Potassium titanyl phosphate: properties and new applications," *Journal of the Optical Society of America B*, no. 4, pp. 622–633, 1989.

[56] A. Zukauskas, N. Thilmann, V. Pasiskevicius, F. Laurell, and C. Canalias, "5 mm thick periodically poled Rb-doped KTP for high energy optical parametric frequency conversion," *Optical Materials Express*, no. 2, pp. 201–206, 2011.

[57] J. Lee, "Beam pointing direction changes in a misaligned porro prism resonator," *Applied Optics*, no. 13, pp. 2701–2707, 1988.

[58] Z. Alperovich, O.Buchinsky, and S. e A. Ishaaya, "Misalignment sensitivity in an intracavity coherently combined crossed-porro resonator configuration," *Laser Physics Letters*, no. 8, p. 085802, 2017.

[59] G.Gould, "Crossed roof prism interferometer," *Applied Optics*, no. 4, pp. 533–534, 1962.

[60] L. Agrawal, "Jones matrix formulation of a Porro prism laser resonator with waveplates: theoretical and experimental analysis," *Applied Physics B*, 2007.

[61] L.Burger, "Kaleidoscope modes in large aperture Porro prism resonators," *Optics Express*, vol. 16, no. 17, pp. 12707–12714, 2008.

[62] R. C. Jones, "A new calculus for the treatment of optical systems. iv.," *J. Opt. Soc. Amer.*, p. 085802, 1942.

[63] B. B. Hu and M. C. Nuss, "Imaging with terahertz waves," *Optics Letters*, vol. 20, no. 16, 1995.

[64] R. R. A. Pavel Shumyatsky, "Terahertz sources," *Journal of Biomedical Optics*, vol. 16, pp. 16 – 16 – 10, 2011.

[65] G. Chattopadhyay, "Technology, capabilities, and performance of low power terahertz sources," *IEEE Transactions on Terahertz Science and Technology*, vol. 1, pp. 33–53, 2011.

[66] K. K, S. M, T. T, and I. H, "Coherent tunable THz-wave generation from $LiNbO_3$ with monolithic grating coupler," *Appl. Phys. Lett.*, 1996.

[67] A. Abina, U. Puc, A. Jeglič, and A. Zidanšek, "Applications of terahertz spectroscopy in the field of construction and building materials," *Applied Spectroscopy Reviews*, vol. 50, no. 4, pp. 279–303, 2015.

[68] M. C. Kemp, P. F. Taday, B. E. Cole, A. J. F. J. A. Cluff, and W. R. Tribe, "Security applications of terahertz technology," vol. 5070, pp. 5070 – 5070 – 9, 2003.

[69] A. promising diagnostic method: Terahertz pulsed imaging and spectroscopy, "Security applications of terahertz technology," *World journal of radiology*, vol. 28, no. 3, pp. 55–65, 2011.

[70] Y.-C. Shen, B. Jin, and D. Saeedkia, *Terahertz applications in the pharmaceutical industry, Handbook of Terahertz Technology for Imaging, Sensing and Communications.* Woodhead Publishing, 2013.